TECHNISCHE UNIVERSITÄT WIEN
Vienna | Austria

DIPLOMARBEIT

The Effect of Atomic Spin-Orbit Coupling on DFT+DMFT Calculations of $LiOsO_3$

zur Erlangung des akademischen Grades

Diplom-Ingenieur

im Rahmen des Studiums

Technische Physik

eingereicht von

Severino Adler, BSc.
Matrikelnummer 00946527

ausgeführt am Institut für Festkörperphysik
der Fakultät für Physik der Technischen Universität Wien
(in Zusammenarbeit mit der Universität Würzburg)

Betreuung
Betreuer: Associate Prof. Dr. Alessandro Toschi
Mitwirkung: Projektass. Dr. Daniel Springer
Prof. Dr. Giorgio Sangiovanni (Universität Würzburg)

Wien, April 2, 2019

(Unterschrift Verfasser) (Unterschrift Betreuer)

Deutsche Zusammenfassung

Aktuelle Experimente an den 5d-Osmium Oxid Perowskiten $NaOsO_3$ und $LiOsO_3$ haben auffällige Unterschiede in den Eigenschaften dieser beiden Materialien ergeben. Mittels Infrarot-Spektroskopie wird für $NaOsO_3$ ein metallisches Verhalten bei Temperaturen oberhalb von $420\,K$, ein Metall-Isolator-Übergang bei niedrigeren Temperaturen, sowie eine langreichweite antiferromagnetische Ordnung gemessen, die durch einen Slater-Lifshitz Übergang verursacht werden. $LiOsO_3$ zeigt kein magnetisches Verhalten auf der vollständigen Temperaturskala und wird hauptsächlich durch die rasche Abnahme des Drude-Peaks in der optischen Leitfähigkeit charakterisiert. Die beobachteten Unterschiede der beiden Materialien können nicht durch eine dichtefunktionaltheoretische (DFT) Behandlung erklärt werden, welche zwei ähnliche, kohärente, metallische Phasen ergeben würde. Die Erweiterung der Rechnung um lokale Wechselwirkungen (DFT+DMFT) mittels dynamischer Molekularfeldtheorie (DMFT) bringt eine deutliche Verbesserung der Beschreibung, allerdings keine Übereinstimmung mit dem Experiment. Es lässt sich zeigen, dass $LiOsO_3$ bei steigender Temperatur wesentlich schneller seine kohärente, metallische Phase verliert als $NaOsO_3$, was bedeutet, dass sich dieses Material näher an einer Mott-Hund isolierenden Phase befindet. Bei Verwendung von ab-initio durch DFT berechneten Parametern ist dieser Effekt verglichen zum Experiment schwächer und findet bei höheren Termperaturen statt. Die Ursache liegt in der Schwächung der Hundschen Wechselwirkung aufgrund der Aufhebung der t_{2g} Entartung um etwa $250\,meV$ durch das vorherrschende Kristallfeld. Die Berücksichtigung von lokaler (atomarer) Spin-Orbit Kopplung, deren atomarer Anteil auf etwa $250\,meV$ abgeschätzt werden kann, in DFT+DMFT Rechnungen, könnte im Prinzip die Entartung der t_{2g} Orbitale wieder herstellen und daher auch der beobachteten Delokalisierung entgegenwirken. Unsere Rechnungen zeigen allerdings, dass das nicht der Fall ist und dass die lokale Spin-Orbit Kopplung die Aufspaltung der t_{2g} Orbital weiter verstärkt. Dadurch kommt es zu einer zusätzlichen Metallisierung von $LiOsO_3$, besonders bei sehr hohen Temperaturen ($1160\,K$). Die Unterschiede zwischen unserer theoretischen Beschreibung und den experimentellen Resultaten können daher nicht erklärt werden. Allerdings zeigen unsere Rechnungen, dass lokale Spin-Orbit Kopplung eine ausschlaggebende Rolle für das magnetische Verhalten von $LiOsO_3$ spielt, welches unter Vernachlässigung derselbigen eine starke Tendenz zur Ausbildung einer langreichweitigen antiferromagnetischen Ordnung zeigt. Nur durch Berücksichtigung von lokaler Spin-Orbit Kopplung kann die experimentell beobachtete, paramagnetische Phase nummerisch stabilisiert werden.

Abstract

Recent experiments on the 5d-Osmium oxide perovskites $NaOsO_3$ and $LiOsO_3$ find striking differences in the physical properties of these two compounds. Infrared-spectroscopy experiments on $NaOsO_3$ show a metallic behavior above 420 K and a metal-insulator transition at lower temperatures accompanied by the onset of an antiferromagnetic long-range order induced by a Slater-Lifshitz transition. $LiOsO_3$ does not display any magnetic phase on the whole temperature range and is characterized by a strong increase of the DC resistivity and a rapid decrease of the Drude peak in the optical conductivity with increasing temperature. The differences in the high temperature behavior of the two materials cannot be captured by density-functional theory (DFT) calculations, which would yield two very similar, coherent, metallic phases for both cases. The inclusion of local correlations by means of DFT+DMFT (dynamical mean-field theory) improves the description, but does not yield perfect agreement with the experiments. In fact, our DFT+DMFT calculation could explain a more rapid loss of the metallic coherence by increasing the temperature in $LiOsO_3$ (w.r.t. $NaOsO_3$) in terms of a slightly closer proximity of this compound to a Mott-Hund's insulating phase. However, by considering interaction values extracted by ab-initio estimates, the overall effect appears weaker and confined to higher temperatures than in the experiment, because the localizing effect of the Hund's exchange is weakened by a small lifting of the t_{2g}-degeneracy by about 250 meV, due to the crystal field. In principle, the inclusion of the local (atomic) spin-orbit coupling (whose atomic part is estimated to be about 250 meV) into DFT+DFMT calculations could have counterbalanced the t_{2g} splitting and, hence, the related weakening of localization. Our calculations show that local spin-orbit coupling, in fact, further increases the lifting of the t_{2g} degeneracy leading to a further metallization of $LiOsO_3$, especially at high temperatures (1160 K). Thus, it cannot explain the observed differences between our theoretical description and the experimental observations. Nevertheless, our new calculations have demonstrated that spin-orbit coupling does play a pivotal role for the magnetic behavior of $LiOsO_3$, which displays without local spin-orbit coupling a strong tendency towards an antiferromagnetic long-range ordering. Eventually, the inclusion of local spin-orbit coupling in our calculations appears as a crucial ingredient to stabilize the experimentally observed paramagnetic phase.

Acknowledgments

This thesis and the sucess of my studies is owed to the support of so many people, of whom I would like to thank some.

First of all, I want to thank my supervisor, Alessandro Toschi, who spent so many hours teaching me the basics and more advanced physics necessary for both, my last project work and my Diploma thesis. My decision to stay in this field is completely owed to him and his dedicatied and inspiring way of teaching and supervising. The hours spent discussing physical observations throughout this thesis, but also scientific politics, have given me great insight into scientific reality and what is needed to keep up with it. Without him I wouldn't be here.

I also want to thank my co-supervisor Daniel Springer, who guided me through the beginnings of my thesis, teaching me all the necassary basics of w2dynamics. He also helped me a great deal improving my writing skills and teached me to present scientific facts shortly, but thoroughly.

Furthermore, I want to thank Giorgio Sangiovanni who also co-supervised this thesis and kindly invited me to Würzburg to learn the more advanced calculations performed in this thesis. He also provided many great discussions, which helped deciding what to do next. As did Andi Hausoel, who actually teached me the background of w2dynamics and how to perform most of my calculations. I will not forget the time we had in Würzburg.

At this point I want to thank Cesare Franchini, Bongjae Kim and Peitao Liu who provided the necessary DFT data for this thesis.

One of the persons I am also indebted to is Marie-Therese Hübsch, with whom I spent many hours learning for exams and who introduced me to Alessandro Toschi in the first place.

I also acknowledge financial support from the Austrian Science Fund (FWF) and in particular the SFB ViCoM proj. nr. F41-15, which also made the numerical calculations performed on the VSC3-cluster possible.

Selbstverständlich ist der Erfolg dieser Diplomarbeit und meines Studiums nicht nur jenen Menschen geschuldet, welche direkt daran beteiligt waren, sondern auch meinen Freunden, meiner Familie (besonders meiner "erweiterten" Familie, Anne-Marie, Willi und Viola) welche mich durch die Höhen und Tiefen der letzten Jahre begleitet haben. Besonderer Dank gilt hier Moritz Pichler. Er hat dankbarerweise diese Arbeit auf Tipp- und Grammatikfehler korrekturgelesen.

Allergrößter Dank gebührt auch meinen Eltern, die mich immer finanziell aber besonders moralisch in all meinen Entscheidungen unterstüzt haben. Ich hatte immer den Freiraum Neues zu versuchen und trotzdem den Rückhalt wieder in ein bekanntes Umfeld zurückzukehren. Der Mensch der ich heute bin, bin ich wegen euch.

Zum Schluß möchte ich dir danken Selina. Meine Ausgeglichenheit der letzten sieben Jahre verdanke ich dir und deiner leidenschaftlichen und liebevollen Hingabe.

Für meine Eltern
Michaela & Hans-Peter
die mich in allen meinen Entscheidungen
stets unterstützt haben.

Contents

Chapter 1

Introduction

In this chapter we briefly review recent experimental findings for $NaOsO_3$ and $LiOsO_3$. The remarkable differences observed in the high temperature regime of these two compounds represent the motivation for the comparative theoretical study presented here. We discuss the electronic properties derived by a density-functional theoretical (DFT) calculation and how they are magnified by electronic intra-atomic interactions using a dynamical mean-field theoretical (DMFT) calculation on top of the DFT calculation. The DMFT results shows a slightly different behavior for both materials, nevertheless, the differences remain too weak to get perfect agreement with the experiment if the calculations are performed with ab-initio estimated values of the interaction parameters. In order to understand which interactions play a significant role we have performed DMFT calculations with different approximations for the interaction Hamiltonian. Furthermore, we have investigated the dependence of the calculation on the chosen one-particle basis, finding that approximations strongly depend on this choice. Due to the slightly lifted t_{2g} degeneracy of about $250\,meV$ in $LiOsO_3$, a basis incorporating this aspect is best suited for making approximations, i.e. approximations made in the basis where the one-particle coefficient matrix of the local Hamiltonian is diagonal yield best agreement with non approximated (full Coulomb) calculations. However, since we do not observe perfect agreement with the experiment even in the full Coulomb calculation, we try to introduce spin-orbit coupling (SOC) on the atomic level. The strength of the atomic (local) SOC can be estimated to approximately $250\,meV$ which is of the same size as the lifting of the t_{2g} degeneracy and, in principle, it could compensate for the decrease of localization generated by the non-degeneracy of the t_{2g} orbitals.
In chapter two we will briefly present the methods used throughout this thesis. Chapter three discusses the differences in the results obtained in different one-particle bases. Chapter four presents the results of our calculations, including local spin-orbit coupling. We will investigate both, the temperature trend at fixed spin-orbit coupling strength and the behaviour for varying the spin-orbit coupling strength at fixed temperature. Finally in chapter five we present the conclusion of this thesis and an outlook on possible next studies.

1.1 Comparison of Two Similar but Different Osmates

In solid state physics, 5d compounds are particularly interesting due to the strong dependence of their physics on the interplay of many interactions, such as the Coulomb repulsion between electrons (e-e interaction), the magnetic and the spin-orbit coupling. In many nominally half filled 3d compounds such as V_2O_3 (which would be nominally half filled with respect to the two lower lying $e_{g\pi}$ orbitals of the t_{2g} manifold) the e-e interaction dominates, due to the spatially small elongation of the 3d orbitals and the small overlap to the neighbouring orbitals. This suffices to explain the experimentally observed behavior. However, as 5d orbitals are spatially more extended than the 3d orbitals [1] and also have a larger overlap to neighbouring orbitals, the effect of the e-e interaction is expected to be reducing w.r.t. the 3d orbitals, becoming of the same order as those of other interactions in 5d compounds. Therefore, it is particularly intriguing to measure and theoretically describe those materials.

In this respect, recent experiments on the 5d-Osmium oxide perovskites $NaOsO_3$ [1, 2] and $LiOsO_3$ [3] have shown that small changes in the electronic configuration do indeed have a big influence on the behavior of a material.

The crystal structures of $NaOsO_3$ and $LiOsO_3$ are displayed in Figure 1.1. Both materials show a similar perovskite structure, with a $Os^{5+}O_6$ octahedral structure as the central block. Both compounds show a tilting of the octahedra, which is enhanced in $LiOsO_3$ compared to $NaOsO_3$ because of the reduced size of the lithium atoms compared to the sodium atoms. Therefore, $NaOsO_3$ has an orthorhombic Pnma (62) crystal structure and $LiOsO_3$ has, as V_2O_3, a trigonal R3c (162) crystal structure. The hybridization of the 2p orbitals of the oxygens surrounding the osmium atoms acts as a crystal-field on the 5d osmium orbitals which splits the five orbitals into two e_g and three t_{2g} orbitals. The two e_g orbitals lie about 4 eV above the three t_{2g} orbitals. Since the lithium and sodium atoms give one electron to the oxygen atoms, osmium will give three of its six 5d electrons to the oxygen atoms. This leaves the osmium with nominally three valence electrons, which exactly half-fill the t_{2g} manifold. The small distortion (tilting) of the octahedra leads to a further small splitting of the t_{2g} manifold into two energetic lower and one energetic higher lying orbital. This is the same splitting as in V_2O_3, which has also a R3c crystal structure. Since V_2O_3 has nominally only two valence electrons, only the lower orbitals are occupied. $LiOsO_3$ and $NaOsO_3$ have nominally three valence electrons. Therefore, we take into account the whole t_{2g} manifold. The e_g manifold is unoccupied and is therefore not considered throughout this thesis. If not stated otherwise by orbitals we will always refer to the three t_{2g} orbitals in the following.

A selection of the experimental results of $NaOsO_3$ and $LiOsO_3$ is shown in Figure 1.2. For both materials the reflectance is measured and the optical conductivity derived via the Kramers-Kronig relations (see [2, 3] for a detailed description of the experimental setup). $NaOsO_3$ (left panels (a) and (b) of Figure 1.2) shows a significant increase in the optical conductivity at low frequencies for increasing temperatures, which is perfectly mirrored by a corresponding enhancement of the DC

[1] The spatially larger extension of the 5d orbitals is easily argued with the fact that the radial wave function of the 5d orbitals has more knots than the radial wave function of the 3d orbitals, and therefore has to radially extend further.

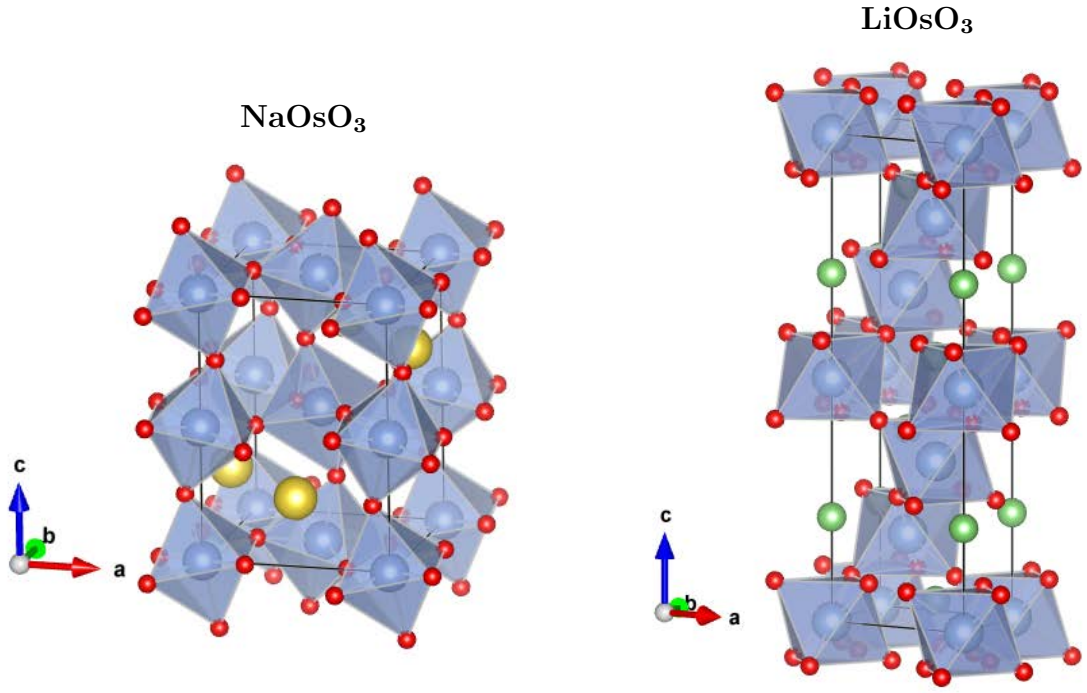

Figure 1.1: Crystal structure of $NaOsO_3$ (left side) and $LiOsO_3$ (right side). The red spheres denote the oxygen atoms, the blue spheres the osmium atoms, the yellow spheres the sodium atoms and the green spheres the lithium atoms. Both compounds show a tilted octahedral $Os^{5+}O_6$ structure which is the building block to its cubic perovskite structure. The tilting is enhanced in $LiOsO_3$ compared to $NaOsO_3$, which is due to the reduced atomic size of the lithium atoms compared to the sodium atoms. $NaOsO_3$ shows a orthorhombic Pnma (62) crystal structure, $LiOsO_3$ shows a trigonal R3c (162) crystal structure (The structure displayed it actually the R3$\bar{c}$ structure, which $LiOsO_3$ takes below 140 K. In R3c the lithium atoms are equally distanced from the upper and lower osmium atoms.). We thank Peitao Liu for providing the pictures of the crystal structures.

conductivity. The significant decrease of the coherent Drude weight in the optical conductivity when reducing the temperature from T=450 K to T=380 K coincides with the onset of a known antiferromagnetic phase with a Néel temperature of 410 K. Therefore, it was first believed that $NaOsO_3$ has a Slater metal-insulator transition (MIT). More recent studies [4] have shown that a more thorough definition can be obtained through a spin-fluctuation driven Lifshitz MIT. For $LiOsO_3$, the experimental data (right panel (c) of Figure 1.2) shows the opposite trend than for $NaOsO_3$. For increasing temperature the Drude peak at low frequencies is rapidly suppressed, yielding even a plateau for T$\geq$300 K, as the material would be on the verge of a MIT at high temperatures. In comparison to $NaOsO_3$, $LiOsO_3$, quite surprisingly, does not show any kind of magnetic ordering over the whole temperature scale.

Not mentioned so far is the ferroelectric state of $LiOsO_3$ which it exhibits below 140 K [5]. Our study stay well above this temperature.

A theoretical description by means of DFT fails to describe most of these differences. The density of states (DOS) of the three 5d Os t_{2g} orbitals for both materials derived with the local-density approximation (LDA) are displayed in Figure 1.3. The left panel (a) shows the DOS

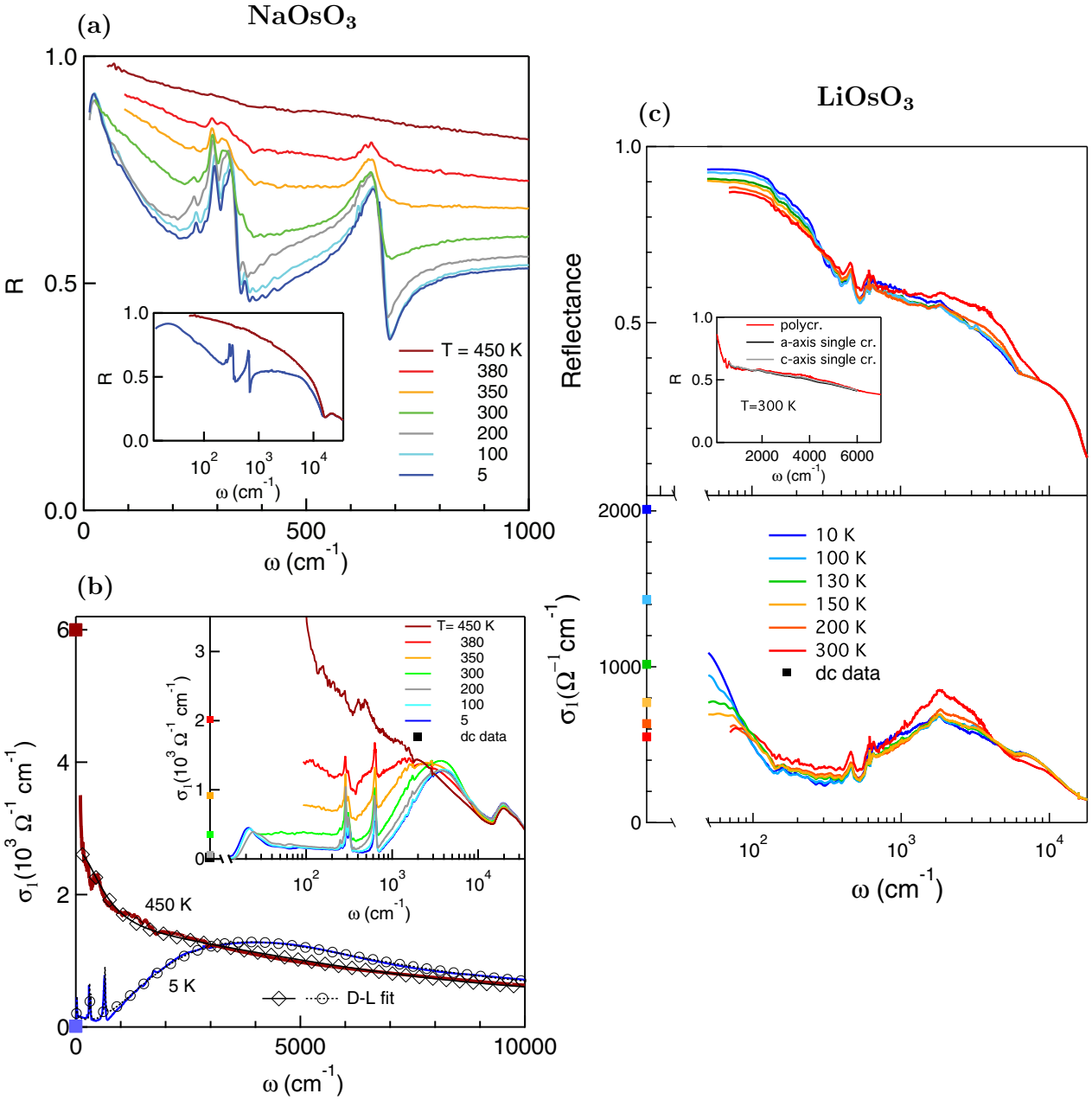

Figure 1.2: Experimental data of the reflectance (R) and the optical conductivity (σ) for (a), (b) $NaOsO_3$[2] and (c) $LiOsO_3$[3] . The optical conductivity is derived from the reflectance with the Kramers-Kronig relations. The inset of (a) shows T=450 K and 5 K on a logarithmic scale. In the main panel of (b) D-L fit is short for a Drude-Lorentz fit to the data. The inset in (c) compares the midinfrared reflectance of a high-density polycrystalline pellet with that of a single crystal oriented along the ac plane.

of $NaOsO_3$, the right panel the DOS of $LiOsO_3$. Both materials have significant weight around the Fermi level, which for both materials is around $\mu \sim 5.1\,\mathrm{eV}$ and have approximately the same bandwidth of around $\sim 3.5\,\mathrm{eV}$. As already discussed, both materials have nominally half filled t_{2g} orbitals and so the DFT calculation would "place" both materials in a metallic phase.

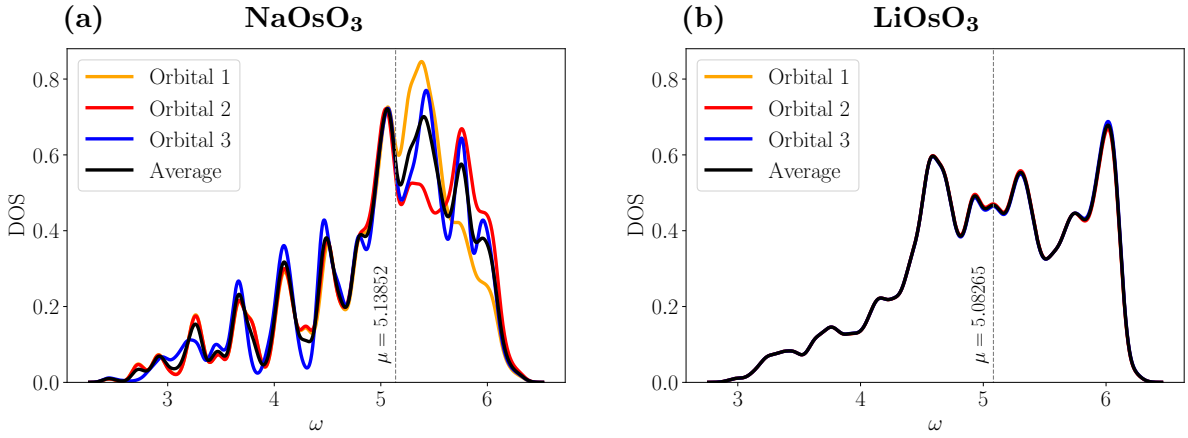

Figure 1.3: LDA density of states of the 3 t_{2g} orbitals of $NaOsO_3$ (a) and $LiOsO_3$ (b). Both density of states show a clear metallic behavior and a similar bandwidth of about 3 eV.

Furthermore, temperature dependencies cannot be directly captured by a DFT calculation. In order to improve the theoretical description of these materials, it appears necessary to take electronic correlation effects introduced by the e-e interaction in the solid into account. These typically tend to localize the electrons, i.e. induce a reduction of the metallicity.

A fast and rudimentary estimate of the importance of electronic correlations can be given by comparing the experimentally measured kinetic energy of the conduction band electrons (through the plasma frequency measured in infrared optical spectroscopy) to the kinetic energy calculated using DFT, i.e. K_{expt}/K_{DFT} [4]. For an uncorrelated material this ratio would tend to unity. A DFT calculation for $NaOsO_3$ [4] yields 0.33 without consideration of SOC and 0.76 with consideration of SOC, which corresponds to a weakly correlated regime. Furthermore, it shows the importance of SOC in the spatially more extended 5d orbitals. For $LiOsO_3$ [3], an alternative estimate for the importance of electronic correlation has been made by comparing the spectral weight of the Drude peak to the spectral weight of the Drude peak plus the mid-infrared contribution visible in Figure 1.2 (a), which yields a ratio of 0.03! This strongly suggests that electronic correlations play a pivotal role in $LiOsO_3$. In order to include the local electronic correlation effects induced by the local electrostatic repulsion of the Os-t_{2g} orbitals, an additional dynamical mean-field theoretical (DMFT) calculation is performed [6, 7]. The low-energy Hamiltonian describing the local interactions is the multi-orbital Hubbard Hamiltonian, which in second-quantization formalism reads

$$\hat{H} = \underbrace{\sum_{i\gamma\sigma,j\bar{\gamma}\bar{\sigma}} (\epsilon_{i\gamma\sigma,j\bar{\gamma}\bar{\sigma}} - \mu\delta_{i\gamma\sigma,j\bar{\gamma}\bar{\sigma}})\hat{c}^{\dagger}_{i\gamma\sigma}\hat{c}_{j\bar{\gamma}\bar{\sigma}}}_{\text{one-partice terms}} + \underbrace{\sum_{i,\gamma_1\sigma_1,\gamma_2\sigma_2,\gamma_3\sigma_3,\gamma_4\sigma_4} U_{\gamma_1\sigma_1,\gamma_2\sigma_2,\gamma_3\sigma_3,\gamma_4\sigma_4}\hat{c}^{\dagger}_{i\gamma_1\sigma_1}\hat{c}^{\dagger}_{i\gamma_2\sigma_2}\hat{c}_{i\gamma_3\sigma_3}\hat{c}_{i\gamma_4\sigma_4}}_{\text{intra atomic mulitband (local) interaction}} \quad , \tag{1.1}$$

where $\hat{c}^{\dagger}_{i\gamma\sigma}$, $\hat{c}_{i\gamma\sigma}$ denote the creation and annihilation operators at a given lattice site i and orbital γ with a given spin σ. The pre-factor $\epsilon_{i\gamma\sigma,j\bar{\gamma}\bar{\sigma}}$ accounts for the one-particle part of the Hamiltonian, which is non-local and corresponds to the kinetic energy, μ for the chemical potential and $U_{\gamma_1\sigma_1,\gamma_2\sigma_2,\gamma_3\sigma_3,\gamma_4\sigma_4}$ for the local Coulomb repulsion between the electrons at the same lattice site occupying the t_{2g} orbitals. In principle, the local interactions of the multi-orbital Hubbard Hamiltonian can induce local and non-local correlation effects. However, dynamical mean-field theory only describes the purely local correlation effects induced by (1.1), i.e. DMFT further approximates the Hubbard Hamiltonian by a purely local Hamiltonian called the Anderson impurity Hamiltonian (introduced in Chapter 2.2.1). The one-particle term $\epsilon_{i\gamma\sigma,j\bar{\gamma}\bar{\sigma}}$ is derived from the Fourier Transform of the overlap integrals of the "wannierized" [8] DFT solution. The unscreened Coulomb interaction coefficients $U_{\gamma_1\sigma_1,\gamma_2\sigma_2,\gamma_3\sigma_3,\gamma_4\sigma_4}$ are derived via calculating the Coulomb integrals with the "wannierized" DFT orbitals. Nevertheless, the unscreened Coulomb interaction coefficients are unphysical, because surrounding orbitals partially screen the Coulomb interaction of the three t_{2g} orbitals. To take the screening effects into account, the Coulomb interaction coefficients of the three t_{2g} orbitals are corrected with a constrained random-phase approximation (cRPA) calculation [9, 10]. The DFT, Wannierization and cRPA calculation have been performed at University of Vienna in the group of professor Cesare Franchini using VASP [11–14] for the DFT calculation and wannier90 [8] for the "wannierization" of the orbitals in advance to this project.

Note that throughout this thesis energy is given in units of eV and, therefore, the Bolzmann's constant reads $8.617 \times 10^{-5}\,\mathrm{eV}\cdot\,\mathrm{K}^{-1}$ [15].

1.1.1 $NaOsO_3$

The results of a previous paramagnetic DFT+DMFT calculation taking into account the full Hamiltonian (1.1) for $NaOsO_3$ are shown in Figure 1.4. All DMFT calculations in this thesis are performed with w2Dynamics [16, 17]. In order to obtain the local spectral function an additional analytical continuation step has been performed with the maximum entropy solver of the ALPS package [18], which is used for all analytical continuations in this thesis. The local spectral function displayed in the main panel shows a metallic behavior, i.e. it has significant weight at $\omega = 0$ for all calculated temperatures. Since our DMFT calculation has enforced the paramagnetic phase no agreement with the experiment can be expected below the temperature of 410 K where $NaOsO_3$ displays a long range antiferromagnetic order [2]. For temperatures far above the Néel temperature of $NaOsO_3$ the local spectral function displays a gradual loss of metallicity with increasing temperature. A complete disappearance of the quasi-particle peak at $\omega = 0$ can be observed only at the highest temperature of 1160 K (most likely well above the melting temperature of this compound). In the high temperature regime we do not have experimental results to compare our results to, but a decreasing local spectral function close to $\omega = 0$ for increasing temperature is also in other correlated materials too, e.g. the typical strongly correlated material V_2O_3 [19, 20]. However, correlation effects in V_2O_3 are much more pronounced as it is a 3d compound. Nevertheless, this trend is an indicator that correlation does

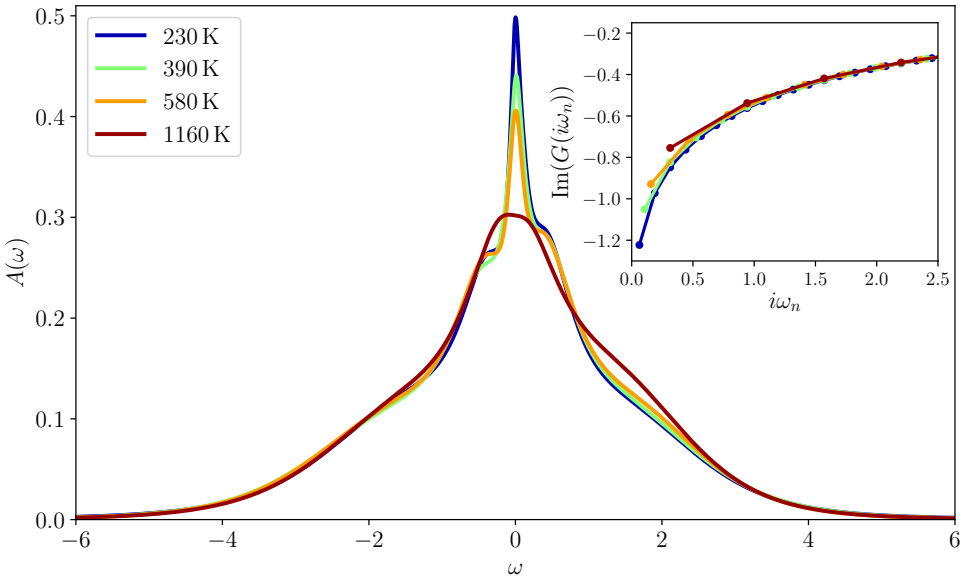

Figure 1.4: Averaged local spectral functions (w.r.t. orbitals and atoms) of $NaOsO_3$ derived from the DMFT data via analytical continuation with the maximum entropy solver of the ALPS package for various temperatures, where $\omega = 0$ corresponds to the Fermi-level. The inset shows the corresponding averaged DMFT Green's functions on the Matsubara axis. The temperature trend of the local spectral function shows an evident loss of metallic coherence for increasing temperature. Nonetheless, $NaOsO_3$ remains metallic for all displayed temperatures.

play a role in $NaOsO_3$.

Another quantity yielding information about the degree of electronic correlations are relative occupancies of the atomic orbitals given by the fraction $\langle \hat{n}_i \hat{n}_j \rangle / \langle \hat{n}_i \rangle \langle \hat{n}_j \rangle$. For an uncorrelated materials this fraction is one. In Figure 1.5 the average occupancy per orbital (c), the relative average double occupancy (a) and the relative average Hund's like occupancy (b) for $NaOsO_3$ are displayed (with Hund's like we refer to double occupancy of different orbital index but same spin index, i.e. measuring the spin alignment between different orbitals). With increasing temperature (decreasing β), the relative double occupancy decreases accompanied by an increase of the relative Hund's like occupancies. Therefore, the material becomes less metallic as spin alignment becomes more important and partially freezes out electronic mobility. The differences in the occupancies of the orbitals display the fact that the t_{2g} orbitals are not degenerate in this basis due to a local distortion. To sum it all up, both, the double occupancies and the Hund's like occupancies display a typical behavior of a correlated metal.

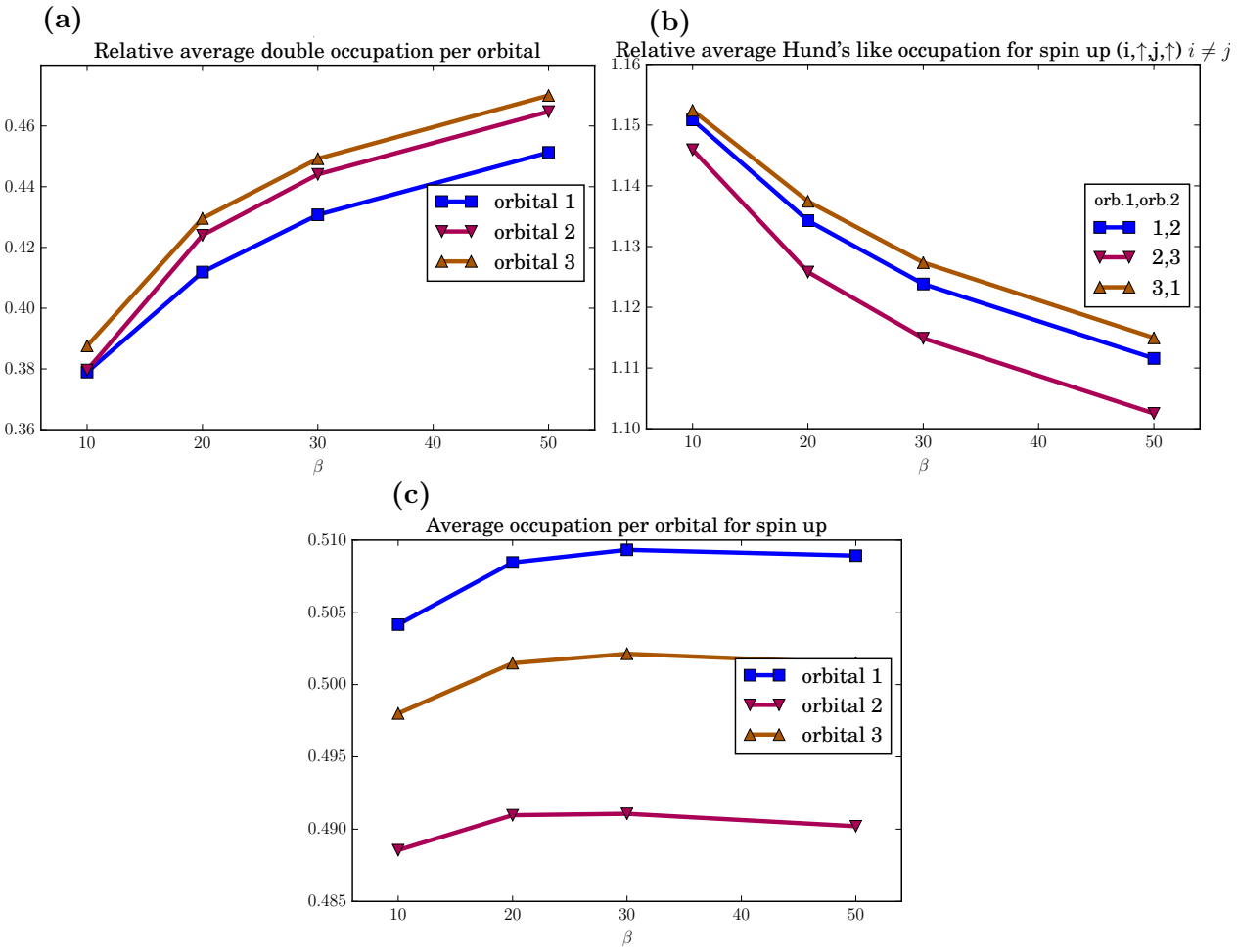

Figure 1.5: Occupancies of $NaOsO_3$ for various temperatures, with $\beta = \frac{1}{k_b T}$. The term "relative" refers to expressions of the form $\frac{\langle \hat{n}_i \hat{n}_j \rangle}{\langle \hat{n}_i \rangle \langle \hat{n}_j \rangle}$. The average occupation per orbital is shown in panel (c) and displays a slight difference between the orbitals, i.e. the t_{2g} orbitals are not perfectly degenerate. Panel (a) shows the relative average double occupation per orbital and panel (b) the relative Hund's like occupation i.e. the spin alignment between different orbitals. As this is a paramagnetic calculation panels (b) and (c) display only the results for the spin up channel. For high temperatures, i.e. small β values, the spin alignment (b) increases whereas the double occupancy (a) decreases consistent with the loss of spectral weight at $\omega = 0$

1.1.2 $LiOsO_3$

As in Section 1.1.1, we performed a paramagnetic DFT+DMFT calculation for $LiOsO_3$ taking into account the full Hamiltonian (1.1) and analytically continued the result to obtain the results displayed in Figure 1.6. The inset shows the corresponding Green's function on the imaginary axis. As for $NaOsO_3$ the local spectral function displays a metallic behavior for all calculated temperatures. However, the decrease of the quasi-particle peak at $\omega = 0$ appears to be more pronounced as it develops the onset of an actual "pseudogap" dip at $\omega = 0$ at 1160 K. The corresponding decrease of the Green's function also appears to be more prominent compared to $NaOsO_3$. At intermediate temperatures of about 580 K the local spectral function of $LiOsO_3$ displays small side peaks around $\omega = \pm 0.5$ eV. Finally, in comparison to $NaOsO_3$ $LiOsO_3$ shows a stronger broadening of the local spectral function with increasing temperature.

To understand the slight differences in the behavior of the local spectral function we investigate the occupancies of $LiOsO_3$ presented in Figure 1.7. All three orbitals are almost perfectly half-filled (panel (c)), indicating the high degree of energy degeneracy in this local basis. This is also clearly reflected in the double and Hund's like occupancy (panel (a) and (b)) where all lines are almost identical. Similar to $NaOsO_3$ the double and the Hund's like occupancies follow opposite temperature trends. However, for high temperatures (low β) $LiOsO_3$ displays a smaller double occupancy and a larger Hund's like occupation compared to $NaOsO_3$ consistent with the trends of the local spectral functions. Overall, $LiOsO_3$ appears to be slightly closer to a possible

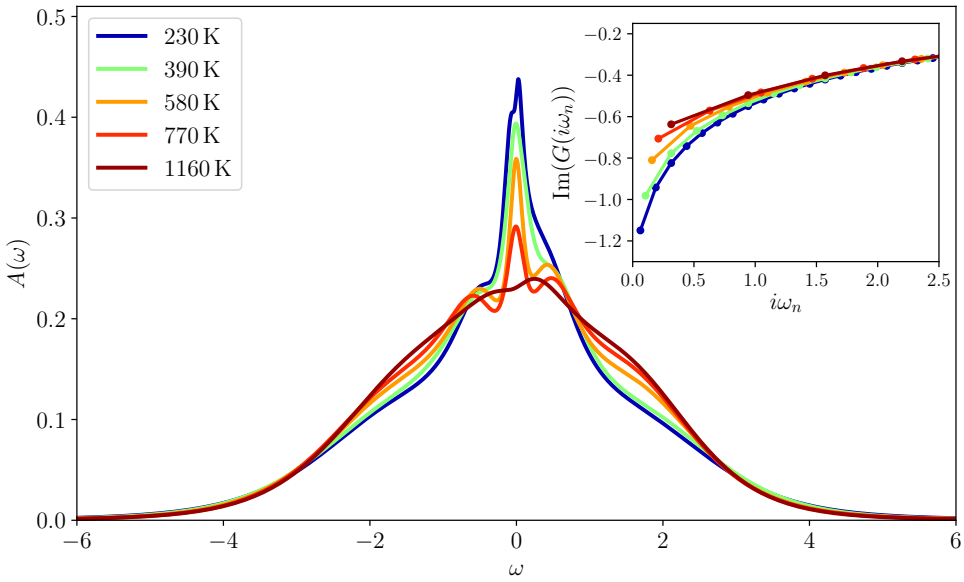

Figure 1.6: Averaged local spectral functions (w.r.t orbitals and atoms) of $LiOsO_3$ derived from the DMFT data via analytical continuation with the maximum entropy solver of the ALPS package for various temperatures, where $\omega = 0$ corresponds to the Fermi-level. The inset shows the corresponding averaged DMFT Green's functions on the Matsubara axis. The temperature trend of the local spectral function shows a clear loss of metallicity for increasing temperatures.

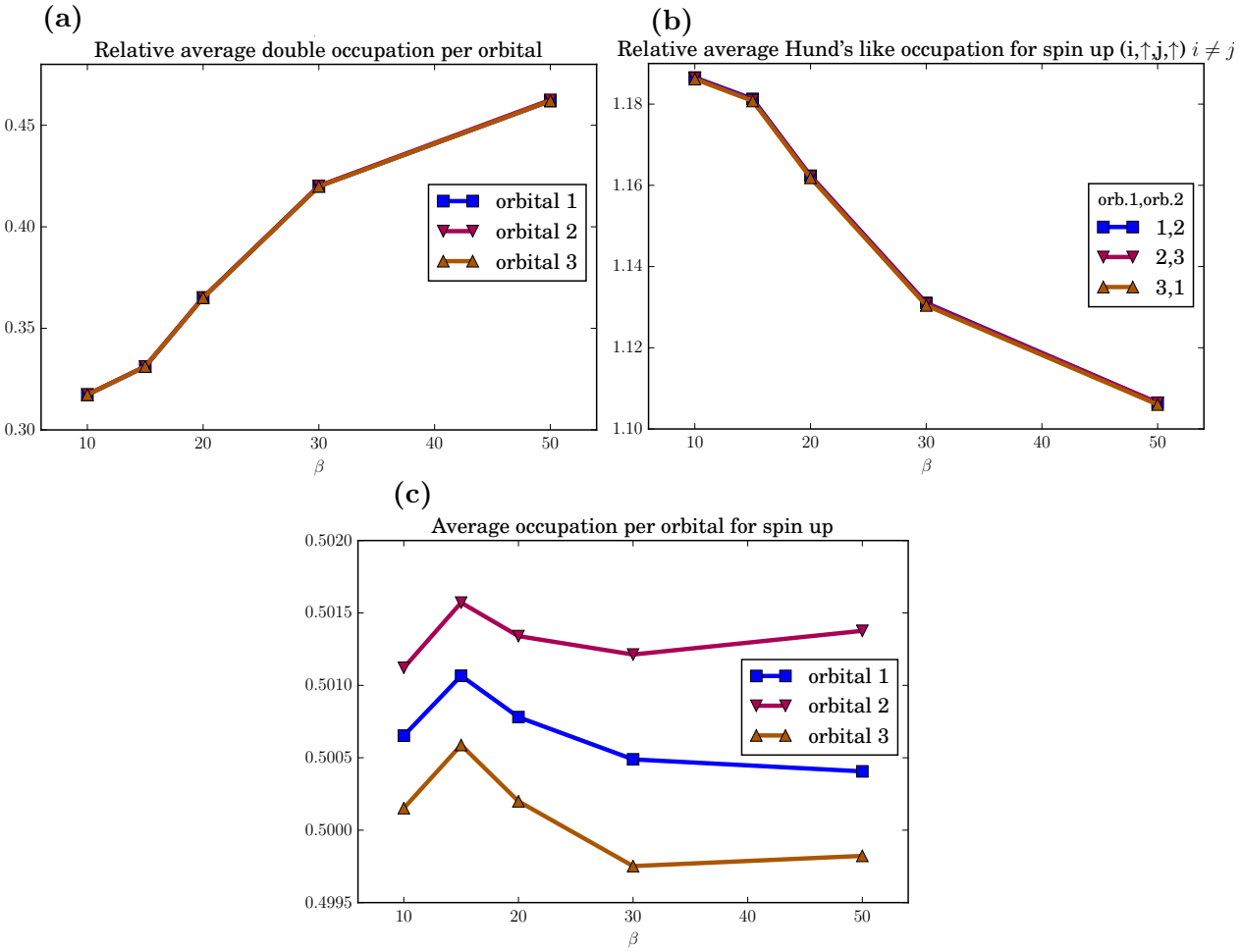

Figure 1.7: Occupancies of $LiOsO_3$ for various temperatures, with $\beta = \frac{1}{k_b T}$. The term "relative" refers to expressions of the form $\frac{\langle \hat{n}_i \hat{n}_j \rangle}{\langle \hat{n}_i \rangle \langle \hat{n}_j \rangle}$. The average occupation per orbital is shown in panel (c) and displays almost no difference between the orbitals, i.e. the t_{2g} orbitals are almost perfectly degenerate in this basis. Panel (a) shows the relative average double occupation per orbital and panel (b) the relative Hund's like occupation, i.e. the spin alignment between different orbitals. As this is a paramagnetic calculation panels (b) and (c) display only the results for the spin up channel. For high temperatures, i.e. small β values, the spin alignment (b) increases whereas the double occupancy (a) decreases consistent with the loss of spectral weight at $\omega = 0$

MIT than $NaOsO_3$, as suggested by the temperature trend the local spectral function and the occupancies. To obtain a deeper insight in the underlying microscopic mechanisms at work we perform additional calculations, taking only certain parts of the interaction term of (1.1) into account.

1.1.3 Analysing Different Interactions

The multi-band Hubbard Hamiltonian (1.1) is of very general type as it retains all on-site terms of the (screened) Coulomb interaction, projected on the Wannier basis of choice. Starting from this full representation of the screened Coulomb interaction, there are two very common approximations of this Hamiltonian: The Density-Density Approximation and the Kanamori Approxi-

mation, where the Kanamori Approximation includes the Density-Density Approximation. In a one particle basis where, i denotes the lattice site, γ the t_{2g} orbitals and σ the spin the Kanamori Hamiltonian reads

$$\begin{aligned}\hat{H}_{\text{Kana}} = & \underbrace{\sum_{i\gamma\sigma}(\epsilon_{i\gamma\sigma,i\gamma\sigma}-\mu)\hat{c}^{\dagger}_{i\gamma\sigma}\hat{c}_{i\gamma\sigma}}_{\text{one-particle terms}} \\ & + \underbrace{U\sum_{i\gamma}\hat{n}_{i\gamma\uparrow}\hat{n}_{i\gamma\downarrow}}_{\text{Intraband Coulomb}} + \underbrace{V\sum_{i,\gamma<\bar{\gamma},\sigma\neq\bar{\sigma}}\hat{n}_{i\gamma\sigma}\hat{n}_{i\bar{\gamma}\bar{\sigma}}}_{\text{Interband Coulomb}} + \underbrace{(V-J)\sum_{i,\gamma<\bar{\gamma},\sigma}\hat{n}_{i\gamma\sigma}\hat{n}_{i\bar{\gamma}\sigma}}_{\text{Hund}} \\ & \underbrace{-J\sum_{i,\gamma\neq\bar{\gamma}}\hat{c}^{\dagger}_{i\gamma\uparrow}\hat{c}^{\dagger}_{i\gamma\downarrow}\hat{c}_{i\bar{\gamma}\uparrow}\hat{c}_{i\bar{\gamma}\downarrow}}_{\text{Pair Hopping}} \underbrace{-J\sum_{i,\gamma\neq\bar{\gamma}}\hat{c}^{\dagger}_{i\gamma\uparrow}\hat{c}_{i\gamma\downarrow}\hat{c}^{\dagger}_{i\bar{\gamma}\downarrow}\hat{c}_{i\bar{\gamma}\uparrow}}_{\text{Spin Flip}} \quad . \end{aligned} \tag{1.2}$$

The first line of (1.2) denotes the diagonal entries of the one-particle term included in (1.1) and the second line of (1.2) constitutes the terms proportional to density-density interactions, which is why these terms are named the Density-Density Approximation. There are three terms contributing to the Density-Density Approximation: the intraband Coulomb repulsion (U), the interband Coulomb repulsion (V) and the Hund term (J), which incorporates the Hund's rule in a solid. In addition to the density-density terms the full Kanamori Hamiltonian also includes pair-hopping and spin-flip terms, denoted in the third line of (1.2). The pair-hopping term is to be understood literally as a pair of one spin up and one spin down electron hopping from one orbital to another orbital at the same site. In contrast, the spin-flip term incorporates a pair of electrons with different spin at different orbitals at the same site to switch places. I other words both electrons flip their spin as an effect of the interaction. These microscopical processes correspond to the so called "quantum fluctuations" of the magnetic moment.

Our previous results calculated with the full Hubbard Hamiltonian (1.1) have shown subtle differences between the two materials $NaOsO_3$ and $LiOsO_3$. To understand their origin we performed additional calculations (also previously to this thesis) using approximation schemes which, per construction, emphasize (i.e. overestimate) specific physical processes, such as the tendency towards a high spin configuration driven by J: the Density-Density and the Kanamori Approximation. The results of the analytically continued local spectral functions are displayed in Figure 1.8. None of the two materials exhibit a significant temperature dependence in the Density-Density Approximation. The grey dashed lines display a representative local spectral function for (a) $LiOsO_3$ and (b) $NaOsO_3$ calculated with the Density-Density Approximation. $LiOsO_3$ shows a clear insulating behavior developing a spectral gap around $\omega = 0$. Introducing the Density-Density Approximation in the material neglects important effects driven by the full Coulomb interaction (such as the quantum fluctuations) as well as significant one-particle contributions such as the intra-atomic inter-orbital hoppings. As a result one tends to largely overestimate the size of the Hund's magnetic moments, and, hence, the corresponding localization effects. This is enough to fully localize the valence electrons of the t_{2g} manifold in $LiOsO_3$ but not in $NaOsO_3$ which for this cRPA values stays metallic at all temperatures.

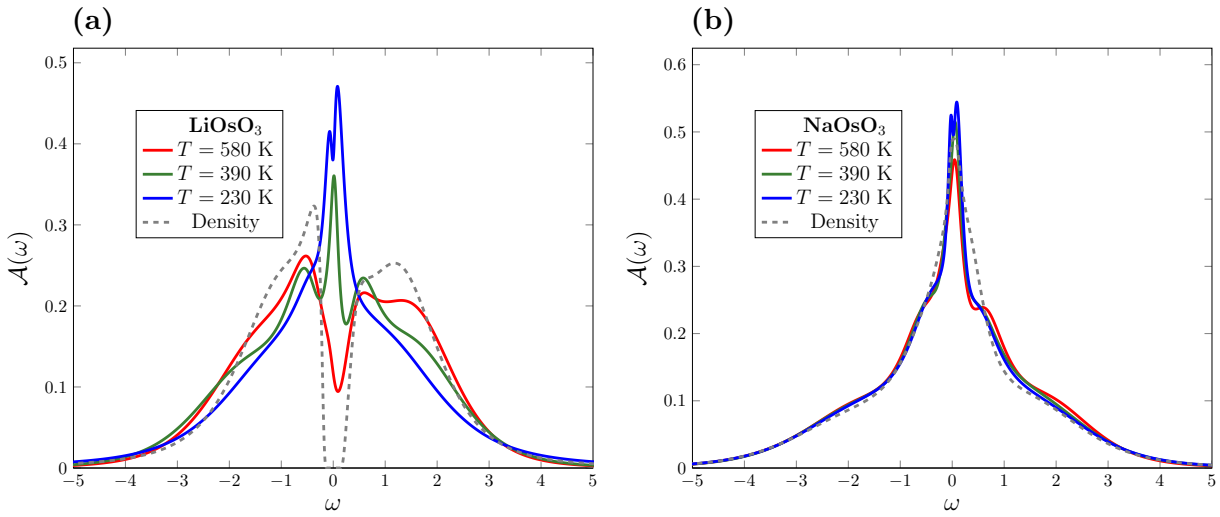

Figure 1.8: Spectral function of $LiOsO_3$ (Kanamori parameters: U=2.41, V=1.79, J=0.26) (a) and $NaOsO_3$ (Kanamori parameters: U=2.27, V=1.69, J=0.23) (b) for the Kanamori and Density-Density interaction. As the Density-Density calculation does not display a distinct temperature dependence only one spectrum is included.

Eventually for $LiOsO_3$ the results do not match with the experiment as they are too insulating. Therefore, we take a look at the results of the less approximated Kanamori calculations also displayed in Figure 1.8. For $LiOsO_3$ the results exhibit a strong temperature dependence of the spectrum. It shows the same trend as the experimentally measured results starting with a clear quasi particle-peak at lower temperatures, which rapidly decreases with increasing temperature. At 580 K the peak is already replaced by a very pronounced dip and it appears to be already at the verge of a MIT. On the other hand, $NaOsO_3$ is metallic over the whole temperature range in both approximations, however, it shows a weak temperature dependence in the Kanamori Approximation. The dependence is weaker as in the full Coulomb calculation displayed in Figure 1.4 and therefore the Kanamori approximation results better agree with the experimental results. It becomes clear that the differences observed in $LiOsO_3$ and $NaOsO_3$ originate in the different interaction and one-particle terms considered in the Density-Density and Kanamori approximation, respectively. For $LiOsO_3$ the additional hopping terms considered in the full calculation significantly change the results, whereas for $NaOsO_3$ they appear to play only a minor role.

So far there is no way to distinguish how important the different one-particle and interaction terms are in order to explain the observed differences. It is therefore of interest to perform a "Gedankenexperiment" where the DMFT calculation is repeated for both materials, but with interchanged interaction parameters. In Figure 1.9 the results of this "Gedankenexperiment" for a calculation performed for the Kanamori Approximation at 390 K are displayed. The left panel (a) shows a calculation for $LiOsO_3$ with its original parameters (i), with only U exchanged (ii), with only J exchanged (iii) and with all interaction parameters exchanged (iv). The right panel (b) displays the same for $NaOsO_3$. Exchanging any parameter immediately yields a result more similar to the respective other material. In the case of $LiOsO_3$ any exchange almost perfectly coincides with the calculation done for $NaOsO_3$, which in comparison appears to be slightly less sensitive to an exchange of the J parameter. However, exchanging U or all parameters

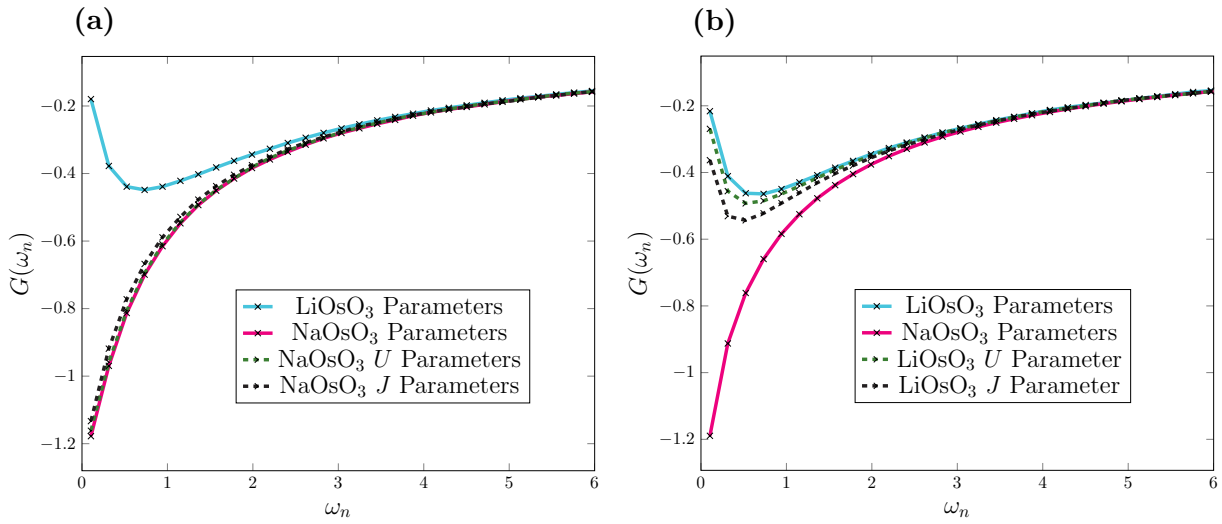

Figure 1.9: A "Gedankenexperiment", where we exchange the U and J values of $LiOsO_3$ and $NaOsO_3$. The results for $LiOsO_3$ with its own and $NaOsO_3$ parameters are shown in (a), the results for $NaOsO_3$ with its own and $LiOsO_3$ parameters are shown in (b). All calculations are performed at a temperature of 390 K

again displays a similar shape as a calculation of $LiOsO_3$. These results are a strong evidence that the main reason for the different properties of these two materials stems from the rather small differences in the values of the interaction parameters and not from the different one-particle terms, i.e. the electronic configuration. However, it seems that a Kanamori approximated calculation is capable of explaining the experimental findings. In this respect it is puzzling that our description becomes worse as we include a more realistic shape of the one-particle terms, i.e. kinetic energy and of the local interaction. Ideally, one would expect that, once the theoretical calculations describe the experimental effects, additional effects will only give a minor contribution. This is not the case for $LiOsO_3$ where a drastic change is observed when more local interaction terms and, especially, more intra-atomic one-particle terms are included, raising the question whether another basis is better suited to perform approximations or not.

1.1.4 The Kanamori Approximation of $LiOsO_3$ in a Different Basis

A DMFT calculation can be performed in different basis sets, which might be more or less suitable for performing an approximation of the interaction or the one-particle hopping terms. Therefore, it is worth investigating the behavior of a Kanamori approximated calculation in a basis incorporating the off-diagonal terms of $\epsilon_{\gamma\sigma,\bar{\gamma}\bar{\sigma}}$, which are induced from the tilting of the $Os^{5+}O_6$ octahedron of the perovskite structure. In order to achieve this $\epsilon_{\gamma\sigma,\bar{\gamma}\bar{\sigma}}$ is diagonalized and the corresponding transformation matrices are used to transform the k dependent one-particle Hamiltonian and the local interaction matrices $U_{\gamma_i\sigma_i,\gamma_j\sigma_j,\gamma_k\sigma_k,\gamma_l\sigma_l}$. Consequently, an extraction of the Kanamori parameters from $U_{\gamma_i\sigma_i,\gamma_j\sigma_j,\gamma_k\sigma_k,\gamma_l\sigma_l}$ yields new parameters for $LiOsO_3$: U=2.35, V=1.82, J=0.29 (compared to: U=2.41, V=1.79, J=0.26, in the standard LS basis). The Hund's parameter J is slightly increased compared to the standard LS basis, whereas the Coulomb repulsion parameter U is slightly decreased. In most calculations electronic systems tend to be very

sensitive to the J value, which acts as a localizing factor at half-filling, i.e. pushing the material towards an insulating phase. However, in this basis we now observe a slight lifting of the t_{2g} degeneracy of 235 meV which decreases the localizing effect of the Hund's exchange. Figure 1.10 displays the result of this calculation compared to the result of the full calculation performed in the standard LS basis (A detailed discussion of the basis dependence of various results can be found in chapter 3). The left panel (a) shows the basis invariant trace of the Green's function calculated in the diagonalized Kanamori Approximation. The right panel (b) shows the trace of the Green's function of full Coulomb calculation in the standard LS basis. Both calculations yield almost the same result for all calculated temperatures proving that in a suitably chosen basis the Kanamori Approximation still incorporates all important effects. However, it further provides evidence that the previous Kanamori calculation performed in the standard LS basis, neglecting the intra-atomic inter-orbital hopping, matches the experiment accidentally due to significant, uncontrolled error cancellation. At the same time the most general calculation (Figure 1.6) can, in principle, be regarded as the best ab-initio theoretical description so far obtained.

At this point our calculations do not explain the experimentally observed trend, especially not the differences between the two materials $NaOsO_3$ and $LiOsO_3$. The calculated local spectral function of $LiOsO_3$ decreases slightly faster (but not fast enough) than the local spectral function of $NaOsO_3$ with increasing temperature. This difference is expected to be more distinct. In fact, for $LiOsO_3$ the experimentally visible trend is seen in the theoretical calculations, but the corresponding temperatures are too high. In order to counter this slight bias towards metallicity, we will include the atomic spin-orbit coupling (SOC) into our calculations and study if it can act as a localizing factor. The strength of the atomic SOC can be estimated to be about 250-300 meV beign of the same size as the delocalizing lifting of the t_{2g} orbitals in $LiOsO_3$.

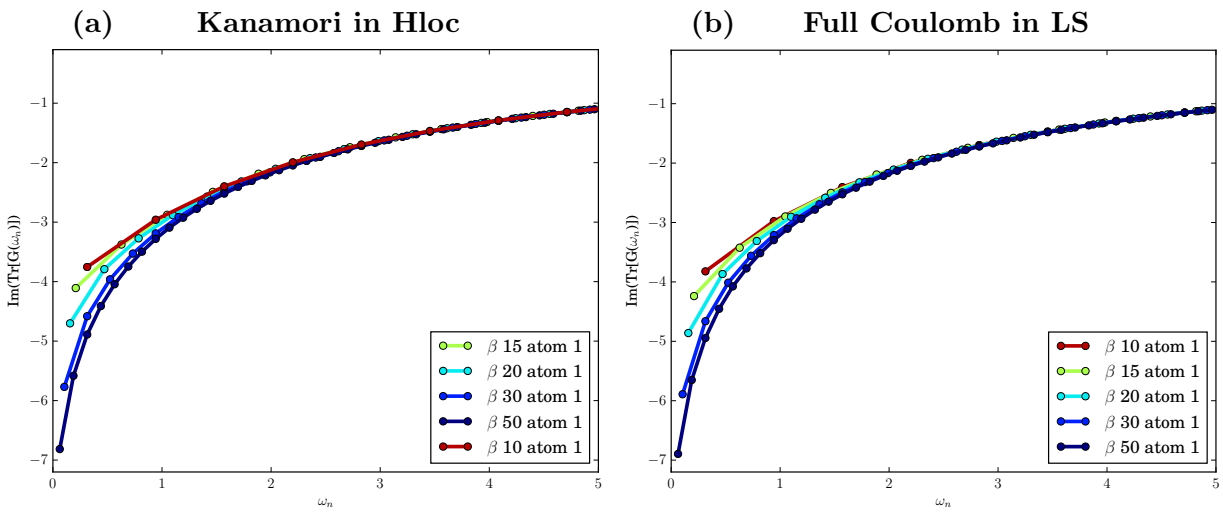

Figure 1.10: Imaginary part of the trace of the Green's function for $LiOsO_3$ of the Kanamori approximation in a basis where the local one-particle Hamiltonian is diagonal (a) and of the full calculation in the standard LS basis (b) with $\beta = \frac{1}{k_b T}$. Both calculations yield the same results. A detailed presentation of the basis dependence of various results can be found in chapter 3

1.1.5 Introducing the Local (Atomic) Spin-Orbit Coupling for $LiOsO_3$

In 5d compounds such as $LiOsO_3$ local correlations are known to be less important than in 3d compounds such as V_2O_3. At the same time the spin-orbit coupling becomes larger. Therefore, spin-orbit coupling could have an influence in this compound. Similar to other terms taken into account on a DMFT level we will only include the local (atomic) [2] part of the SOC. In general, it is possible to perform a DFT calculation including SOC, but it is not possible to obtain ab-initio the necessary interaction matrices $U_{\gamma_i\sigma_i,\gamma_j\sigma_j,\gamma_k\sigma_k,\gamma_l\sigma_l}$ from a corresponding cRPA calculation. Therefore, it is necessary to introduce local (atomic) SOC by hand, i.e. add it to the one-particle term of the Hamiltonian (1.1). For the 3 t_{2g} orbitals in the order xz, yz, xy the SOC Hamiltonian reads [21, 22]

$$\hat{H}_{\mathrm{SOC}} = \xi \hat{l} \cdot \hat{s} = \frac{\xi}{2} \begin{pmatrix} 0 & -i\sigma_3 & i\sigma_1 \\ i\sigma_3 & 0 & -i\sigma_2 \\ -i\sigma_1 & i\sigma_2 & 0 \end{pmatrix} \tag{1.3}$$

where σ_i are the Pauli spin matrices

$$\sigma_1 = \begin{pmatrix} 0 & 1 \\ 1 & 0 \end{pmatrix} \qquad \sigma_2 = \begin{pmatrix} 0 & -i \\ i & 0 \end{pmatrix} \qquad \sigma_3 = \begin{pmatrix} 1 & 0 \\ 0 & -1 \end{pmatrix} \quad . \tag{1.4}$$

As one can see, the SOC Hamiltonian introduces additional complex off-diagonal terms. In principle, those could either act localizing or delocalizing because they represent additional hopping terms, as this Hamiltonian is to be added to the one-particle terms of (1.1). It is the main purpose of this thesis to investigate how the spin-orbital coupling influences a DMFT calculation of $LiOsO_3$, in particular, if it can explain the differences between the observed experimental measurements and the theoretical description.

[2] Throughout this thesis we will call it local instead of atomic spin-orbit coupling, since the term "local" better suits the DMFT context. We are aware that this is not consistent with the title of this thesis, however, the title is chosen in a way that it is familiar to a broad audience.

Chapter 2

Methods

In this chapter we start by methodologically introducing the definition of Green's function at finite temperatures. Then we give a short introduction into the Wick's rotation, the related Matsubara formalism and how to use it to compute one-particle Green's functions at finite temperatures and also introduce the concept of the self-energy. The dynamical mean-field theory (DMFT) is illustrated as a theory describing local correlations in a lattice. At the center of DMFT is the connection of the Anderson impurity model (AIM) to the Hubbard model via a self-consistent mapping, where at convergence the interacting local lattice Green's function equals the interacting AIM Green's function. As next step the concept and the algorithm of continuous-time quantum-Monte-Carlo (CT-QMC) as a solver of the auxiliary AIM of DMFT is explained. Eventually, the obtained Green's function needs to be analytically continued to obtain local spectral functions. This is done by means of the Maximum entropy method which is briefly illustrated to round up the whole calculation procedure.

2.1 Perturbative Expansion of the Green's Function

The central object for a quantum-field theoretical calculation of a solid is the time ordered Green's function. A detailed introduction of the Green's functions can be found in many books [23–30]. In a second quantization formalism, with a time independent Hamiltonian, the one-particle Green's function reads

$$G_{ij}(x, x', t - t') \equiv -i\langle \mathcal{T} \hat{\Psi}_i(x, t) \hat{\Psi}_j^\dagger(x', t') \rangle \quad , \tag{2.1}$$

where $\hat{\Psi}_i$, $\hat{\Psi}_i^\dagger$ are fermionic annihilation and creation operators, $\mathcal{T}$ represents the time ordering symbol, i.e. later times have to be sorted to the left, and $\langle \dots \rangle$ represents the expectation value. For a temperature dependent Green's function expressing the expectation value yields

$$G_{ij}(x, x', t - t') = -i \frac{\mathrm{Tr}\left[e^{-\beta \hat{H}} \mathcal{T} \hat{\Psi}_i(x, t) \hat{\Psi}_j^\dagger(x', t')\right]}{\mathrm{Tr}\left[e^{-\beta \hat{H}}\right]} \quad , \tag{2.2}$$

where β is the inverse temperature, $\hat{H}$ the Hamiltonian describing the system and $e^{-\beta \hat{H}}$ is the density matrix of the system. In most cases it is impossible to exactly evaluate expression (2.2).

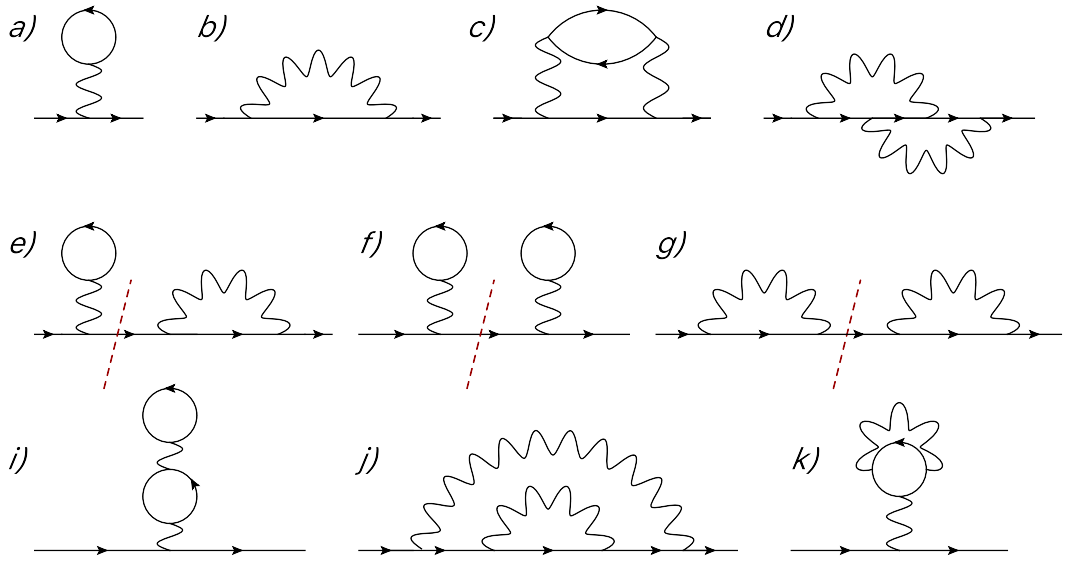

Figure 2.1: Different types of Feynmann diagrams for the Green's function. Fermionic propagators are represented by solid straight lines, bosonic interactions are represented by wiggly lines. Diagrams a), b), c), d) are one-particle irreducible and have no corrections on internal lines. Diagrams e), f), g) are one-particle reducable indicated by the red dashed lines. Diagrams i), j), k) are also one-particle irreducible but have corrections for internal lines.

However, for equilibrium calculations, i.e. where the system is in an equilibrium state, there is a widely used formalism which significantly simplifies calculations, namely the Matsubara formalism. To understand its main idea, let us revisit (2.2) and write down the time evolution of the creation and annihilation operators explicitly

$$\hat{\Psi}_i(x,t) = e^{it\hat{H}}\hat{\Psi}_i(x)e^{-it\hat{H}} \to \mathrm{Tr}\left[e^{-\beta\hat{H}}\mathcal{T}e^{it\hat{H}}\hat{\Psi}_i(x)e^{-it\hat{H}}e^{it'\hat{H}}\hat{\Psi}_j^\dagger(x')e^{-it'\hat{H}}\right] \quad . \tag{2.3}$$

The similarity between the density matrix $e^{-\beta\hat{H}}$ and the time evolution operator $e^{-it\hat{H}}$ can be used to introduce a so called Wick rotation, which rotates the time coordinate into the complex plane. In practice this essentially corresponds to replacing $it \to \tau$, where $\tau \in [-\beta, \beta]$. Using the cycling property of the trace and replacing $\tau - \tau' \to \tau$ yields

$$\mathrm{Tr}\left[e^{-\beta\hat{H}}\mathcal{T}e^{\tau\hat{H}}\hat{\Psi}_i(x)e^{-\tau\hat{H}}\hat{\Psi}_j^\dagger(x')\right] \quad . \tag{2.4}$$

Similar to (2.2) it is possible to define a Matsubara Green's function as

$$G_{ij}(x,x',\tau) = -\langle\mathcal{T}_\tau\hat{\Psi}_i(x,\tau)\hat{\Psi}_j^\dagger(x',0)\rangle = -\frac{\mathrm{Tr}[e^{-\beta\hat{H}}\mathcal{T}_\tau\hat{\Psi}_i(x,\tau)\hat{\Psi}_j^\dagger(x',0)]}{\mathrm{Tr}[e^{-\beta\hat{H}}]} \quad , \tag{2.5}$$

where $\mathcal{T}_\tau$ is the complex time ordering operator, i.e. greater τ get sorted to the left. Functions in Matsubara space are denoted with τ as argument.

For simplicity the indices of G and the x, x' dependence will be dropped until stated otherwise. The Matsubara Green's function has the important property that $G(\tau+\beta) = -G(\tau)$ for fermions

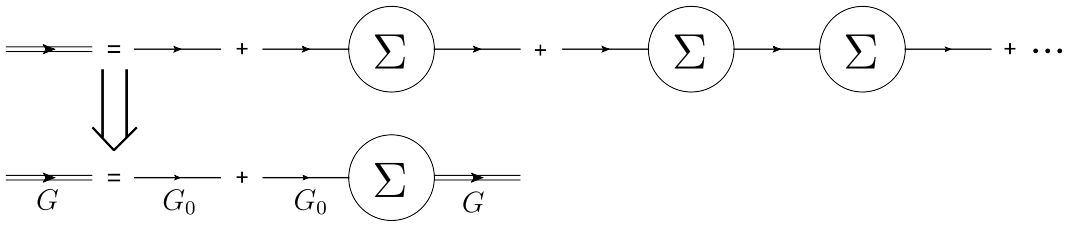

Figure 2.2: Graphical derivation of the Dyson equation where G (double lines) represents the full Green's function, G_0 (single lines) represents the non-interacting (bare) Green's function and Σ represents the self energy which consists of all one-particle irreducible lines without internal corrections [e.g. Figure 2.1 a), b), c), d)].

yielding a semi-discrete Fourier transform

$$G(\tau) = \frac{1}{\beta} \sum_{n=-\infty}^{\infty} G(\omega_n) e^{-i\omega_n \tau} \tag{2.6}$$

$$G(\omega_n) = \int_0^\beta d\tau \, G(\tau) e^{i\omega_n \tau} \quad , \tag{2.7}$$

where ω_n are the odd, discrete Matsubara frequencies

$$\omega_n = \frac{(2n+1)\pi}{\beta} \quad . \tag{2.8}$$

The advantage of the Matsubara Green's function is that it can be perturbatively evaluated order by order in the interaction picture using the Wick theorem, yielding the famous Feynman diagrammatic [24, 25, 30]. Some possible diagrams for a fermionic interacting theory are displayed in Figure 2.1. The diagrams can be classified into 3 groups. Type A are diagrams like a), b), c) and d) of Figure 2.1. These diagrams are one-particle irreducible diagrams, i.e. they do not reduce to two independent diagrams if one fermionic line is cut, which have no internal corrections to fermionic lines. Type B are one-particle reducable diagrams like e), f) and g) of Figure 2.1 and type C are one-particle irreducible diagrams which have corrections to internal fermionic lines as in i), j) and g) of Figure 2.1.

The sum of all diagrams of type A is called the self-energy and can be used to derive an important equation of quantum-field theory. Excluding all diagrams of type C, the sum over all diagrams of type A and B can schematically be drawn as in Figure 2.2, where Σ represents the self-energy, i.e. the sum of all diagrams of type A, G represents the interacting Green's function and G_0 the non-interacting Green's function. Straightforwardly reordering the diagrams yields the second line of Figure 2.2 which can be written down in k-space as

$$G(k, \omega_n) = G_0(k, \omega_n) + G_0(k, \omega_n) \Sigma(k, \omega_n) G(k, \omega_n) \quad , \tag{2.9}$$

where $G_0 = [i\omega_n + \mu - \epsilon_k]^{-1}$. This equation is known as Dyson equation and is extensively used in modern quantum-field theory. Diagrams of type C can then be included via iteratively reinserting G as G_0. Therefore, the self-energy can be used to iteratively calculate the interacting Green's

function. For a fermionic system the Dyson equation has a more general form

$$G(k, \omega_n) = \left[i\omega_n + \mu - \epsilon_k - \Sigma(k, \omega_n) \right]^{-1} \tag{2.10}$$

where μ is the chemical potential and ϵ_k is the dispersion relation of the given system. In calculations one approach would be to calculate the self-energy of a given system using the non-interacting Green's function, inserting the self-energy into (2.10) and using the obtained G as new G_0 to calculate the new self-energy. This procedure is iterated until the self-energy converges.

2.2 Dynamical Mean-Field Theory

The quantum many-body problem, posed e.g. by systems of correlated electrons, has been puzzling physicist for decades. Hence, many theoretical approaches have been invented to address this problem. One of the most basic schemes is the mean-field theory. The main concept of mean-fields is to average over a part of the degrees of freedom to obtain a significantly simpler "local" problem. As a typical example we recall the Curie-Weiss self-consistency approximation for the Ising model. This concept can be extended to a many-body quantum field theory as well and corresponds to the so-called dynamical mean-field theory (DMFT) [31–34]. The difference to common mean-field theories is that in DMFT time is kept as a degree of freedom. Hence, the mean-field may change with time and it is possible to take into account correlation effects in time, which corresponds to including local quantum fluctuations. However, all spatial (non-local) correlation effects are not included, reducing its applicability to problems where spatial correlations play only a minor role. Fortunately, in several correlated materials the non-local correlation effects (which only belong to a single lattice site or a small unit cell) do not play a major role compared to the local correlation effects.

2.2.1 From the Hubbard Model to the Anderson-Impurity Model

For many quantum field theoretical calculations in a solid the Hubbard Hamiltonian of (1.1) suffices to perform accurate calculations. However, it is not possible to calculate an exact solution for a quantum system using eq. (1.1) as Hamiltonian. To obtain non perturbative results it is possible to apply DMFT. Applying DMFT in this context means to simplify eq. (1.1) to a fully local model (without explicit site dependence), solving this model to obtain the self-energy and assuming this self-energy to be correct for the lattice (Hubbard) model as well. If the local lattice Green's function is equal to the Green's function of the fully local model, self-consistency is reached. If not, the local lattice Green's function is used to build a new input model. A full description of this cycle is presented later in this thesis. This fully local model is the so-called the Anderson Impurity Model (AIM). This model consists of a non-interacting bath of electrons

and an impurity site, which can have multiple orbitals. The AIM Hamiltonian yields

$$\begin{aligned}\hat{H}_{AIM} =& \underbrace{\sum_{k,\sigma} \tilde{\epsilon}_k \hat{a}^\dagger_{k\sigma}\hat{a}_{k\sigma}}_{H_{\text{bath}}} + \underbrace{\sum_{k,\gamma,\sigma} V_{k,\gamma}(\hat{c}^\dagger_{\gamma\sigma}\hat{a}_{k\sigma} + \hat{a}^\dagger_{k\sigma}\hat{c}_{\gamma\sigma})}_{H_{\text{hyb}}} + \underbrace{\sum_{\gamma\sigma,\bar{\gamma}\bar{\sigma}} \epsilon_{\gamma\sigma,\bar{\gamma}\bar{\sigma}}\hat{c}^\dagger_{\gamma\sigma}\hat{c}_{\bar{\gamma}\bar{\sigma}}}_{H^{\text{kin}}_{\text{loc}}} \\ &+ \underbrace{\sum_{\gamma_1\sigma_1,\gamma_2\sigma_2,\gamma_3\sigma_3,\gamma_4\sigma_4} U_{\gamma_1\sigma_1,\gamma_2\sigma_2,\gamma_3\sigma_3,\gamma_4\sigma_4}\hat{c}^\dagger_{\gamma_1\sigma 1}\hat{c}^\dagger_{\gamma_2\sigma_2}\hat{c}_{\gamma_3\sigma_3}\hat{c}_{\gamma_4\sigma_4}}_{H^{\text{int}}_{\text{loc}}} - \underbrace{\sum_{\gamma}\mu(\hat{n}_{\gamma\uparrow}+\hat{n}_{\gamma\downarrow})}_{H^{\mu}_{\text{loc}}} \quad , \quad (2.11)\end{aligned}$$

where $\hat{c}$, $\hat{c}^\dagger$, $\hat{n}$ are the annihilation, creation and number operator at the impurity site, γ denotes the orbitals of the impurity sites, σ denotes the spin, $\hat{a}$, $\hat{a}^\dagger$ are the annihilation and creation operator of the non-interacting bath states which are counted with the subscript k and $V_{k,\gamma}$ the amplitude to hop from the bath to an impurity orbital.

To keep the notation compact we will combine $\gamma\sigma \to \gamma$ from here on. Further, a bold notation is introduced to denote matrices with γ dependence, so that $\mathbf{A} \equiv A_{\gamma\bar{\gamma}}$ and $\mathbf{1}$ denotes the unit matrix. The amplitude $V_{k,\gamma}$ is connected the so-called hybridisation function via

$$\Delta_{\gamma\bar{\gamma}}(\omega_n) = \sum_k \frac{V_{\gamma,k}V_{\bar{\gamma},k}}{i\omega_n - \tilde{\epsilon}_k} \quad . \tag{2.12}$$

Using the hybridisation function, the non-interacting *impurity* Green's function of the AIM, denoted by $\mathcal{G}$, can be written as

$$\mathcal{G}^0_{\gamma\bar{\gamma}}(\omega_n) = [i\omega_n\mathbf{1} + \mu\mathbf{1} - \boldsymbol{\epsilon} - \boldsymbol{\Delta}(\omega_n)]^{-1}_{\gamma\bar{\gamma}} \quad . \tag{2.13}$$

In order to connect the AIM to the Hubbard model (1.1), the standard way is to calculate a k dependent one-particle Hamiltonian, i.e. $\epsilon_{i\sigma_i,j\sigma_j} \to \epsilon_{\gamma\bar{\gamma}}(k)$, and the chemical potential by means of DFT, where the one-particle Hamiltonian connects to it's local part via

$$\epsilon_{\gamma\bar{\gamma}} = \sum\!\!\!\!\!\!\int_k \epsilon_{\gamma\bar{\gamma}}(k) \quad , \tag{2.14}$$

where $\sum\!\!\!\!\!\!\int_k$ denotes the constant weight average over all k-points of the first Brillouin zone (which corresponds to evaluating the discrete Fourier transform from k to x at $x = 0$). Furthermore, the hybridisation function Δ is calculated via

$$\begin{aligned}\Delta_{\gamma\bar{\gamma}}(\omega_n) &= i\omega_n\delta_{\gamma\bar{\gamma}} + \mu\delta_{\gamma\bar{\gamma}} - \epsilon_{\gamma\bar{\gamma}} - \big[\sum\!\!\!\!\!\!\int_k \mathbf{G}_0(\omega_n,k)\big]^{-1}_{\gamma\bar{\gamma}} \\ &= i\omega_n\delta_{\gamma\bar{\gamma}} + \mu\delta_{\gamma\bar{\gamma}} - \epsilon_{\gamma\bar{\gamma}} - \big[\sum\!\!\!\!\!\!\int_k [i\omega_n\mathbf{1} + \mu\mathbf{1} - \boldsymbol{\epsilon}(k)]^{-1}\big]^{-1}_{\gamma\bar{\gamma}} \quad . \end{aligned} \tag{2.15}$$

One important quantity left is the local interaction matrix $U_{\gamma_1\gamma_2\gamma_3\gamma_4}$, which is derived from a cRPA calculation. Using $\epsilon_{\gamma\bar{\gamma}}(k)$, μ, $U_{\gamma_1\gamma_2\gamma_3\gamma_4}$ and $\Delta_{\gamma\bar{\gamma}}(\omega_n)$ it is possible to perform a DMFT calculation.

2.2.2 The Self-Consistency Cycle of Dynamical Mean-Field Theory

The DMFT self-consistency cycle [17, 32] on the level of the Green's function is displayed for the single orbital case in Figure 2.3. The yellow box to the left represents the starting point, i.e. the non-interacting lattice Green's function, which can be calculated analytically. Averaging over all k points yields the non-interacting Green's function of the impurity. The next step is to solve the impurity-model, which is also the computational bottleneck and can be done with different algorithms, e.g. density-matrix renormalization group (DMRG) [35, 36], exact diagonalization (ED) [32] and continuous-time quantum Monte Carlo (CT-QMC) [17, 37]. The input used to perform this calculation with w2dynamics are the local one-particle coefficients $\epsilon_{\gamma\hat{\gamma}}$, the chemical potential μ, the hybridisation function $\Delta_{\gamma\hat{\gamma}}(\omega_n)$ and the interaction coefficients $U_{\gamma_1\gamma_2\gamma_3\gamma_4}$. The generated output is the interacting impurity Green's function $\mathcal{G}_{\gamma\bar{\gamma}}(\omega_n)$ which is inserted into a reformulated version of (2.10) to obtain the impurity self-energy $\Sigma_{\gamma\bar{\gamma}}(\omega_n)$. Evidently, after the first iteration this is not the self-energy with respect to the initial model but with respect to the auxiliary input model only. Now the crucial step is to use a reformulated version of (2.10) again to calculate the interacting lattice Green's function $G_{\gamma\bar{\gamma}}(\omega_n, k)$ using the non-interacting lattice Green's function $G_{0,\gamma\bar{\gamma}}(\omega_n, k)$ and the self-energy $\Sigma_{\gamma\bar{\gamma}}(\omega_n, k)$, which is approximated by the local self-energy $\Sigma_{\gamma\bar{\gamma}}(\omega_n)$. This step incorporates the approximation, that only local interactions play a crucial role as the impurity self-energy $\Sigma_{\gamma\bar{\gamma}}(\omega_n)$ is inserted into the Dyson Equation. Now

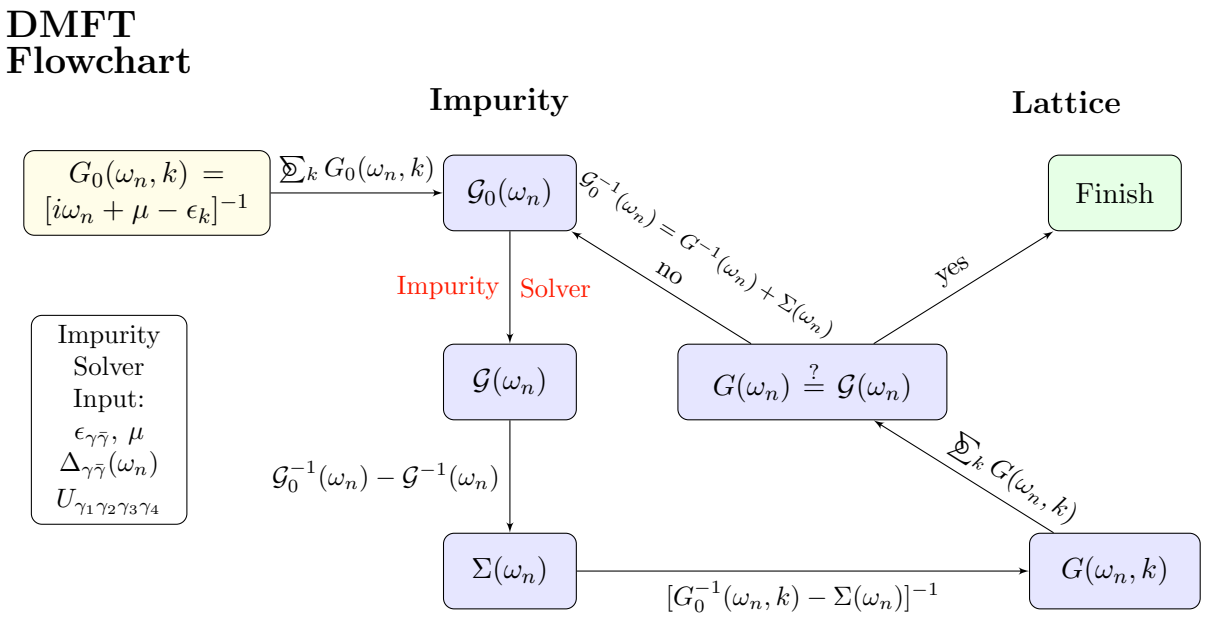

Figure 2.3: Schematic DMFT flowchart for a single orbital calculation. The light yellow box to the left denotes the starting point, whereas all boxes with a light blue background are part of the DMFT self-consistency cycle, and the light green box to the right denotes the end of the DMFT calculation. The computational bottleneck of the whole calculation is the impurity solver, which is written in red in the flowchart. The terms written above and besides the arrows denote the mathematical operation performed to obtain the quantity of the next box (with respect to the arrow direction).

one checks whether the local interacting lattice Green's function $G_{\gamma\bar{\gamma}}(\omega_n) = \sum\!\!\!\!\!\!\int_k G_{\gamma\bar{\gamma}}(\omega_n, k)$ is equal to the interacting impurity Green's function $\mathcal{G}_{\gamma\bar{\gamma}}(\omega_n)$. If so, convergence of the DMFT cycle is reached. If not, the local interacting lattice Green's function is used to build a new, non-interacting impurity Green's function (Weiss field) of the auxiliary impurity model. This cycle is repeated until convergence is reached.

In practice the convergence check is not necessarily implemented into the code as the interacting lattice and impurity Green's functions tend to fluctuate around the real solution. A convergence check is in these cases done by visual inspection, mostly of the impurity self-energy. The lattice site of Figure 2.3 can then be cut short via directly calculating the new hybridisation function from the initial input and the impurity self-energy via

$$\begin{aligned}\Delta_{\gamma\bar{\gamma}}(\omega_n) &= i\omega_n\delta_{\gamma\bar{\gamma}} + \mu\delta_{\gamma\bar{\gamma}} - \epsilon_{\gamma\bar{\gamma}} - \Sigma_{\gamma\bar{\gamma}}(\omega_n) - \Big[\sum\!\!\!\!\!\!\int_k \mathbf{G}(\omega_n, k)\Big]^{-1}_{\gamma\bar{\gamma}} \\ &= i\omega_n\delta_{\gamma\bar{\gamma}} + \mu\delta_{\gamma\bar{\gamma}} - \epsilon_{\gamma\bar{\gamma}} - \Sigma_{\gamma\bar{\gamma}}(\omega_n) - \Big[\sum\!\!\!\!\!\!\int_k [i\omega_n\mathbf{1} + \mu\mathbf{1} - \boldsymbol{\epsilon}(k) - \boldsymbol{\Sigma}(\omega_n)]^{-1}\Big]^{-1}_{\gamma\bar{\gamma}} \quad . \end{aligned} \tag{2.16}$$

Furthermore, the DFT calculation already takes into account some local interaction contributions which have to be subtracted in the DMFT cycle in order to avoid double-counting these. This is done with the so called double-counting contribution Σ^{DC} which is added to (2.16) yielding

$$\begin{aligned}\Delta_{\gamma\bar{\gamma}}(\omega_n) =& i\omega_n\delta_{\gamma\bar{\gamma}} + \mu\delta_{\gamma\bar{\gamma}} - \epsilon_{\gamma\bar{\gamma}} - \Sigma_{\gamma\bar{\gamma}}(\omega_n) \\ &- \Big[\sum\!\!\!\!\!\!\int_k [i\omega_n\mathbf{1} + \mu\mathbf{1} - \boldsymbol{\epsilon}(k) - (\boldsymbol{\Sigma}(\omega_n) - \boldsymbol{\Sigma}^{\mathrm{DC}})]^{-1}\Big]^{-1}_{\gamma\bar{\gamma}} \quad . \end{aligned} \tag{2.17}$$

Deriving the double-counting contribution is a hard task, since there is no analytically "correct" way of doing this. All double-counting contributions should be considered as "ad hoc" plausible estimates. This thesis does not focus on the effect of different double-counting contributions and assumes the double-counting of the fully localized limit [38] for all calculations.

The description above is correct if the Hubbard Hamiltonian can be simplified to an AIM of only a single site. However, in practice it is often necessary to consider more than one atom in the unit cell to obtain the correct description, e.g. if there are significant distortions and in the case of antiferromagnetism. To include a larger unit cell it is necessary to expand the formal schemes presented above. First, note that there is an additional index $a, \bar{a}$, denoting the atom in the unit cell and therefore: $\Sigma^{\mathrm{DC}}_{\gamma\bar{\gamma}} \to \Sigma^{\mathrm{DC}}_{a,\gamma\bar{\gamma}}$, $\epsilon_{\gamma\bar{\gamma}} \to \epsilon_{a\gamma,\bar{a}\bar{\gamma}}$ and $\Sigma_{\gamma\bar{\gamma}}(\omega_n) \to \Sigma_{a\gamma,\bar{a}\bar{\gamma}}$. Then the non-interacting lattice Green's function yields

$$G^0_{a\gamma,\bar{a}\bar{\gamma}}(\omega_n, k) = \big[i\omega_n\mathbf{1} + \mu\mathbf{1} - \boldsymbol{\epsilon}(k) + \boldsymbol{\Sigma}^{\mathrm{DC}}\big]^{-1}_{a\gamma,\bar{a}\bar{\gamma}} \tag{2.18}$$

and the interacting lattice Green's function yields

$$G_{a\gamma,\bar{a}\bar{\gamma}}(\omega_n, k) = \big[i\omega_n\mathbf{1} + \mu\mathbf{1} - \boldsymbol{\epsilon}(k) - (\boldsymbol{\Sigma}(\omega_n) - \boldsymbol{\Sigma}^{\mathrm{DC}})\big]^{-1}_{a\gamma,\bar{a}\bar{\gamma}} \quad . \tag{2.19}$$

The complete DMFT cycle is displayed in Figure 2.4. The light yellow box denotes the start of the calculation. $G^0_{a\gamma,\bar{a}\bar{\gamma}}(\omega_n, k)$ is calculated using (2.18). The k dependency is then eliminated by averaging over all k-points in the Green's function and the one-particle term $\epsilon_{a\gamma,\bar{a}\bar{\gamma}}(k)$. This generates the local lattice Green's function and local one-particle Hamiltonian on the whole unit cell. The next step is to generate, i.e. downfold this problem to, N single-impurity problems, where N is the number of atoms in the unit cell. This can be done by projecting down all quantities to the subspaces of the respective atoms and calculating the non-interacting impurity Green's function (Weiss field), i.e.

$$(\boldsymbol{\mathcal{G}}^{0,i})^{-1}_{\gamma\bar{\gamma}}(\omega_n) = (\mathbf{P}_{ia}\mathbf{G}^{\text{old}}_{a,\bar{a}}(\omega_n)\mathbf{P}_{\bar{a}i})^{-1}_{\gamma\bar{\gamma}} + \Sigma^i_{\gamma\bar{\gamma}}(\omega_n) \quad , \tag{2.20}$$

$$\epsilon^i_{\gamma\bar{\gamma}} = P_{ia}\epsilon_{a\gamma,\bar{a}\bar{\gamma}}P_{\bar{a}i} \quad , \tag{2.21}$$

$$\mu^{\text{DC}}_i = P_{ia}\mu^{\text{DC}}_a \quad , \tag{2.22}$$

where P_{ia} is a projector to the subspace of the i-th atom of the first Brioullin zone. For every atom the corresponding impurity hybridisation function is calculated using

$$\Delta^i_{\gamma\bar{\gamma}}(\omega_n) = i\omega_n\delta_{\gamma\bar{\gamma}} + \mu\delta_{\gamma\bar{\gamma}} - \epsilon^i_{\gamma\bar{\gamma}} - \left[\boldsymbol{\mathcal{G}}^{0,i}(\omega_n)\right]^{-1}_{\gamma\bar{\gamma}} \quad . \tag{2.23}$$

Then every impurity is solved with the chosen impurity solver yielding a new interacting impurity

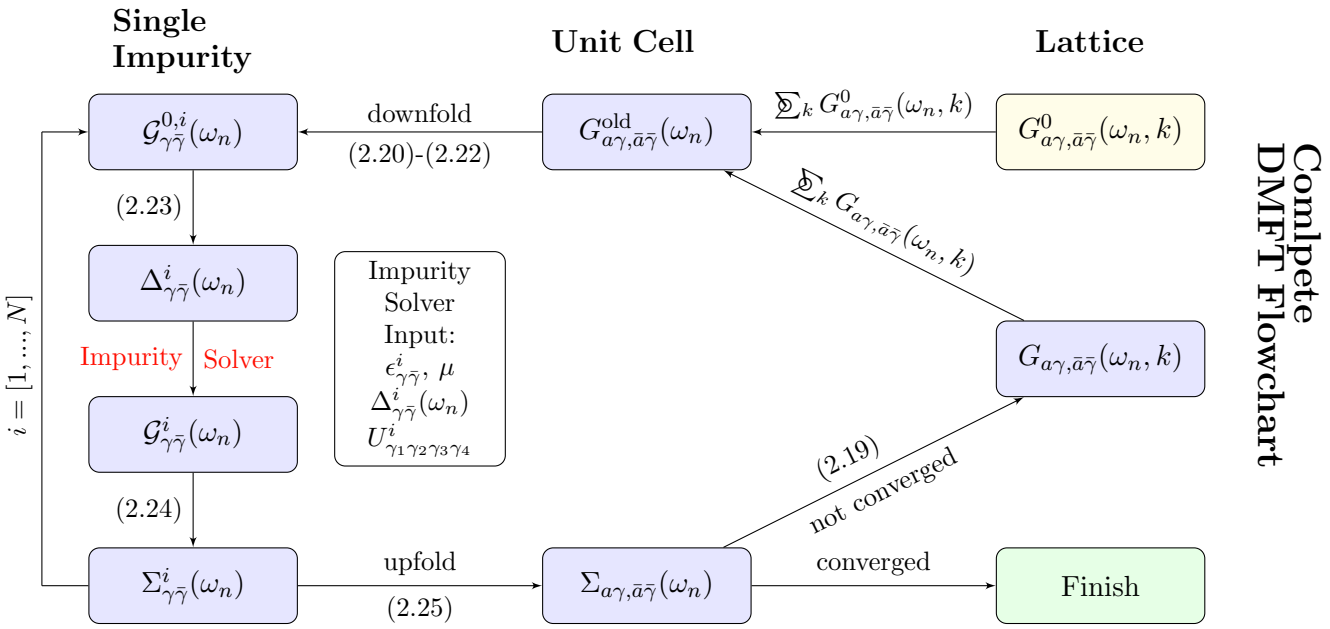

Figure 2.4: Complete DMFT flowchart. The light yellow box to the right denotes the starting point, whereas all boxes with a light blue background are part of the DMFT self-consistency cycle, and the light green box to the right denotes the end of the DMFT calculation. N denotes the number of atoms in the unit cell. The computational bottleneck of the whole calculation is the impurity solver, which is written in red in the flowchart.

Green's function $\mathcal{G}^i_{\gamma\bar{\gamma}}(\omega_n)$ and furthermore by means of the Dyson Equation (2.10)

$$\Sigma^i_{\gamma\bar{\gamma}}(\omega_n) = [\boldsymbol{\mathcal{G}}^{0,i}(\omega_n)]^{-1}_{\gamma\bar{\gamma}} - [\boldsymbol{\mathcal{G}}^{i}(\omega_n)]^{-1}_{\gamma\bar{\gamma}} \quad . \tag{2.24}$$

The full self-energy is consequently obtained via upfolding the N single impurity self-energies to the unit cell, i.e.

$$\Sigma_{a\gamma,\bar{a}\bar{\gamma}}(\omega_n) = \begin{pmatrix} \Sigma^1_{\gamma\bar{\gamma}}(\omega_n) & 0 & 0 \\ 0 & \ddots & 0 \\ 0 & 0 & \Sigma^N_{\gamma\bar{\gamma}}(\omega_n) \end{pmatrix}_{a\bar{a}} \quad . \tag{2.25}$$

If the full self-energy is converged, the calculation is finished. Otherwise the new self-energy is inserted into (2.19). Now the self-consistency cycle is iterated again using the local interacting lattice Green's function $G_{a\gamma,\bar{a}\bar{\gamma}}(\omega_n)$ to build new impurity problems via (2.20)-(2.22).

2.3 Continous-Time Quantum-Monte-Carlo Solver

All calculations in this thesis exploit the continuous-time Quantum-Monte-Carlo (CT-QMC) method implemented in the hybridisation expansion [37] in the w2dynamics [17] package to solve the auxiliary impurity problem. As it is well known, this represents the bottleneck of the DMFT cycle (see Figure 2.4).

The CT-QMC method aims to calculate the partition function of a system with a Hamiltonian $H = H_a + H_b$ via Monte-Carlo sampling the occurring integrals and sums [37], e.g.

$$\begin{aligned} Z &= \mathrm{Tr}\big[\mathcal{T}_\tau e^{-\beta H_a} e^{-\int_0^\beta d\tau H_b(\tau)}\big] \\ &= \sum_k (-1)^k \int_0^\beta d\tau_1 ... \int_{\tau_{k-1}}^\beta d\tau_k \mathrm{Tr}\big[e^{-\beta H_a} H_b(\tau_k) H_b(\tau_{k-1}) ... H_b(\tau_1)\big] \quad , \end{aligned} \tag{2.26}$$

where H_a is treated exactly and H_b is treated perturbatively. For the AIM, $H = H_{\mathrm{bath}} + H_{\mathrm{hyb}} + H_{\mathrm{loc}}$ as in (2.11), there are different choices of H_a and H_b which correspond to different CT-QMC variants. For instance, the choice $H_a = H_{\mathrm{bath}} + H_{\mathrm{hyb}} + H^{\mathrm{kin}}_{\mathrm{loc}} + H^{\mu}_{\mathrm{loc}}$ and $H_b = H^{\mathrm{int}}_{\mathrm{loc}}$ is called the "interaction expansion algorithm" (CT-INT) and $H_a = H_{\mathrm{bath}} + H_{\mathrm{hyb}} + H^{\mathrm{kin}}_{\mathrm{loc}} + H^{\mathrm{int}}_{\mathrm{int}} + H^{\mu}_{\mathrm{loc}}$ and $H_b = H_{\mathrm{hyb}}$ the "hybridisation expansion algorithm" (CT-HYB) [37]. For multi-orbital calculations close to a Mott transition a CT-HYB algorithm performs better and can reach lower temperatures than the CT-INT algorithm. Therefore, w2dynamics uses the CT-HYB algorithm in its DMFT self-consistency cycle. In the CT-HYB expansion (2.26) can be obtained as [37]

$$\begin{aligned} Z = & Z_{\mathrm{bath}} \sum_k \int_0^\beta d\tau_1 ... \int_{\tau_{k-1}}^\beta d\tau_k \int_0^\beta d\tau'_1 ... \int_{\tau'_{k-1}}^\beta d\tau'_k \sum_{\gamma_1 ... \gamma_k} \sum_{\gamma'_1 ... \gamma'_k} \\ & \mathrm{Tr}\big[\mathcal{T}_\tau e^{-\beta H_{\mathrm{loc}}} \hat{c}_{\gamma_k}(\tau_k) \hat{c}^\dagger_{\gamma'_k}(\tau'_k) ... \hat{c}_{\gamma_1}(\tau_1) \hat{c}^\dagger_{\gamma'_1}(\tau'_1)\big] \det \Delta \quad , \end{aligned} \tag{2.27}$$

where

$$Z_{\text{bath}} = \text{Tr}\left[e^{-\beta H_{\text{bath}}}\right] \quad , \tag{2.28}$$

$$\det \Delta = \frac{1}{Z_{\text{bath}}} \text{Tr}\Bigg[\mathcal{T}_\tau e^{-\beta H_{\text{bath}}} \sum_{k_1 \ldots k_k} \sum_{k'_1 \ldots k'_k} V_{\gamma_1,k_1} V^*_{\gamma'_1,k'_1} \ldots V_{\gamma_k,k_k} V^*_{\gamma'_k,k'_k} \times \hat{c}^\dagger_{k_k}(\tau_k)\hat{c}_{k'_k}(\tau'_k) \ldots \hat{c}^\dagger_{k_1}(\tau_1)\hat{c}_{k'_1}(\tau'_1)\Bigg] \quad . \tag{2.29}$$

The numerically time consuming part of this calculation is the evaluation of the trace in (2.27). However, recent improvements approach this by including the trace into the sampling routine (superstate sampling, where the trace is partially sampled via dividing it into blocks of different importance, and state sampling, where the trace is completely sampled) [16], which increases the speed of the code. One of the problems of CT-QMC is the "negative sign problem" typical for Monte-Carlo simulations of fermions [37, 39].

Every sampling routine needs a weighting factor for each sample. In the case of fermionic calculations this weighting factor is in general not positive definite. The solution is to take the absolute value to restore positive definiteness. However, this comes with the price of a less efficient sampling routine, since samples with different sign, which actually cancel, can both have a high weighting factor making it more probable to include this samples into the calculation, although in the end they do not contribute. This is unproblematic for real valued CT-HYB calculations. However, when considering SOC, which introduces imaginary contributions to the local Hamiltonian, calculations lack from a servere sign problem. So far the sign problem of calculations including SOC has not been solved. It can only be mitigated with more efficient sampling routines like the "supterstate sampling" [16] which allows to increase the sampling rate to reach a higher accuracy of the results at a given "sign level".

2.4 Maximum Entropy Method

So far all calculations are performed in Matsubara space, where time and frequencies are imaginary. In order to obtain a spectra on the real frequency axis, which allows direct comparison with experiments, it is necessary to analytically continue the result of the DMFT calculation. In practice, the Green's function on the imaginary time (τ) axis is only known for N components of the dense τ axis with finite precision, i.e.

$$\mathcal{G}(\tau_n) = \mathcal{G}_n = \frac{1}{M} \sum_{j=1}^{M} \mathcal{G}_n^{(j)} \quad , \tag{2.30}$$

where M is the number of samples for the specified τ_n. The finite precision is then incorporated by the covariance matrix C_{nm}

$$C_{nm} = \frac{1}{M(M-1)} \sum_{j=1}^{M} (\mathcal{G}_n - \mathcal{G}_n^{(j)})(\mathcal{G}_m - \mathcal{G}_m^{(j)}) \quad . \tag{2.31}$$

The Green's function on the imaginary axis is related to the local spectral function ($A(\omega) = -\frac{1}{\pi}\mathrm{Im}[G(\omega)]$) on the real axis via [18, 40]

$$\mathcal{G}(\tau_n) = \int_{-\infty}^{\infty} d\omega\, A(\omega) \frac{-e^{-\tau_n \omega}}{1 + e^{-\beta\omega}} \quad . \tag{2.32}$$

The Maximum Entropy method does a smooth fit of $A(\omega)$ such that the functional

$$Q = \frac{1}{2}\chi^2 - \alpha S[A] \tag{2.33}$$

becomes minimized, where α is a Lagrange multiplier,

$$\chi^2 = \sum_{n,m}^{M} (\bar{\mathcal{G}}_n - \mathcal{G}_n) C^{-1}_{nm} (\bar{\mathcal{G}}_m - \mathcal{G}_m) \tag{2.34}$$

and

$$S[A] = -\int d\omega\, A(\omega) \ln\left[\frac{A(\omega)}{d(\omega)}\right] \quad . \tag{2.35}$$

Here $\bar{\mathcal{G}}$ is the Green's function associated to $A(\omega)$ and $d(\omega)$ is a default model for $A(\omega)$. Ideally, the result will not depend on $d(\omega)$. In practice it does, making it worth investigating a few default models when performing an analytical continuation with the Maximum Entropy method. All Maximum Entropy calculations in this thesis have been performed with the Maxent solver of the ALPS package [18].

Chapter 3

Results without Spin-Orbit Coupling

The basis used to perform DMFT calculations is not unique as any linear combination (obtained by rotation) of Wannier orbitals can be used as a new basis. In the following chapter we discuss how this rotation of the basis looks like in the second quantization formalism yielding new $\epsilon_{\gamma\bar{\gamma}}$ and $U_{\gamma_1\gamma_2\gamma_3\gamma_4}$. Then we introduce a basis where $\epsilon_{\gamma\bar{\gamma}}$ is diagonal (we call this the locally diagonal or Hloc basis), which is better suited for a consistent Kanamori approximation, because (i) it automatically incorporates the non-negligible off-diagonal one-particle hopping terms of the standard (LS) basis and (ii) it allows for a more direct physical interpretation. The differences between a calculation performed in the standard basis and a calculation performed in the locally diagonal basis might become significant. For example, if in the chosen approximation scheme (e.g. Kanamori) the orbital off-diagonal terms of $\epsilon_{\gamma\bar{\gamma}}$ are consistently neglected in the standard basis, one would get that $LiOsO_3$ behaves like a material on the verge of a MIT. At the same time, it will shows a metallic behavior in the locally diagonal basis. The latter coincides with the results of a full Coulomb calculation, which, does not depend on the chosen basis as we explicitly verified. The fact that a Kanamori approximation in the locally diagonal basis agrees with the full Coulomb calculation shows that the off-diagonal one-particle terms of the standard basis play indeed a significant role in the physics of this material. In fact, an analytical continuation of the Matsubara results shows that the quasi-particle peak around $\omega = 0$ indeed decreases with increasing temperature in the locally diagonal basis. The predicted temperature dependence is, however, too weak to explain the experimental results, calling for an extension of the theoretical calculations made.

3.1 Introducing a New Basis

As already mentioned in chapter 1.1.4 even when one as properly chosen a fixed representation for the Wannier projection the basis in which we perform the DMFT calculation is not fixed a priori. This can be motivated by the definition of $\epsilon_{\gamma\bar{\gamma}}$ from a DFT calculation

$$\epsilon_{\gamma\bar{\gamma}} \propto \int d^3x \, \mathcal{W}^*_{\gamma}(\vec{x}) \hat{H}^{\mathrm{DFT}} \mathcal{W}_{\bar{\gamma}}(\vec{x}) \quad , \tag{3.1}$$

where $\mathcal{W}_{\gamma}$ are Wannier functions [15]. Choosing a linear combination of Wannier functions as a

new basis gives new $\tilde{\epsilon}_{\gamma\bar{\gamma}}$, but still spans the full Hilbert space of the selected manifold. The same holds for the interaction matrix $U_{\gamma_1\gamma_2\gamma_3\gamma_4}$ which is calculated by

$$U_{\gamma_1\gamma_2\gamma_3\gamma_4} \propto \int d^3x d^3x' \, \mathcal{W}^*_{\gamma_1}(\vec{x})\mathcal{W}^*_{\gamma_2}(\vec{x}\,')f(\vec{x}-\vec{x}\,')\mathcal{W}_{\gamma_3}(\vec{x})\mathcal{W}_{\gamma_4}(\vec{x}\,') \quad , \tag{3.2}$$

where $f(\vec{x}-\vec{x}\,')$ is defined by cRPA. In a second quantization formalism this corresponds to transforming the local one particle annihilation $\hat{c}_\gamma$ and creation $\hat{c}^\dagger_\gamma$ operators with a unitary transformation yielding [39]

$$\hat{d}_\gamma = \sum_{\bar{\gamma}} V^*_{\bar{\gamma}\gamma}\hat{c}_{\bar{\gamma}} \tag{3.3}$$

$$\hat{d}^\dagger_\gamma = \sum_{\bar{\gamma}} V_{\bar{\gamma}\gamma}\hat{c}^\dagger_{\bar{\gamma}} \quad , \tag{3.4}$$

where we will refer to $V_{\bar{\gamma}\gamma}$ as "rotation" matrix. There is, a priori, no possibility to decide which basis is best suited for DMFT calculations, since the CT-QMC algorithm used as impurity solver is able to take into account all elements of $\epsilon_{\gamma\bar{\gamma}}$ and $U_{\gamma_1\gamma_2\gamma_3\gamma_4}$ the results of the calculations will be basis independent. However, for performance reasons it is very common to approximate the full local one-particle and interaction Hamiltonian by neglecting some off-diagonal terms. In order to do so, it is important that the neglected terms are small compared to the other terms. In case of a Kanamori approximation, where the off-diagonal (correlated hopping) terms are neglected, a consistent calculation also neglects all off-diagonal elements of the local one-particle Hamiltonian (off-diagonal with respect to $\epsilon_{\gamma\bar{\gamma}}$). For $LiOsO_3$, however, this is equivalent to neglecting the non-degeneracy of the 3 t_{2g} orbitals. We therefore argue that the most realistic Kanamori Approximation should be performed in a basis where the local one-particle Hamiltonian of every atom is diagonal. Choosing the rotation such that $\tilde{\epsilon}^i_{\gamma\bar{\gamma}}$ is diagonal the new one-particle term of the local Hamiltonian reads

$$\sum_{\gamma\bar{\gamma}} \epsilon^i_{\gamma\bar{\gamma}}(\hat{c}^i_\gamma)^\dagger\hat{c}^i_{\bar{\gamma}} = \sum_{\delta\bar{\delta}}\sum_{\gamma\bar{\gamma}} \epsilon^i_{\gamma\bar{\gamma}}(V^i_{\gamma\delta})^* V^i_{\bar{\gamma}\bar{\delta}} \, (\hat{d}^i_\delta)^\dagger\hat{d}^i_{\bar{\delta}} = \sum_{\delta\bar{\delta}} \tilde{\epsilon}^i_{\delta\bar{\delta}}(\hat{d}^i_\delta)^\dagger\hat{d}^i_{\bar{\delta}} \quad , \tag{3.5}$$

where the index i refers to the atoms of the unit cell and

$$\tilde{\epsilon}^i_{\delta\bar{\delta}} = E^i_\delta\delta_{\delta\bar{\delta}} \quad . \tag{3.6}$$

In terms of a DFT+DMFT calculation, where the input is a k-dependent $\epsilon_{\gamma\bar{\gamma}}(k)$ "Wannier Hamiltonian", the input Hamiltonian is rotated with the $V^i_{\gamma\bar{\gamma}}$ at every k-point. This also yields a new interaction coefficient matrix which can be calculated with [39]

$$\tilde{U}^i_{\delta_1\delta_2\delta_3\delta_4} = \sum_{\gamma_1\gamma_2\gamma_3\gamma_4} U^i_{\gamma_1\gamma_2\gamma_3\gamma_4}(V^i_{\gamma_1\delta_1})^*(V^i_{\gamma_2\delta_2})^* V^i_{\gamma_3\delta_3}V^i_{\gamma_4\delta_4} \quad . \tag{3.7}$$

If the local one-particle Hamiltonian has no spin dependency, e.g. DFT without SOC, the local interaction coefficient matrix transforms like (note that we expand $\gamma \to \gamma\sigma$ now)

$$\tilde{U}^i_{\delta_1\sigma_1,\delta_2\sigma_2,\delta_3\sigma_3,\delta_4\sigma_4} = \sum_{\gamma_1\gamma_2\gamma_3\gamma_4} U^i_{\gamma_1\sigma_1,\gamma_2\sigma_2,\gamma_3\sigma_3,\gamma_4\sigma_4} (V^i_{\gamma_1\delta_1})^* (V^i_{\gamma_2\delta_2})^* V^i_{\gamma_3\delta_3} V^i_{\gamma_4\delta_4} \quad , \tag{3.8}$$

where only the orbital indices γ_i are transformed.

A full Coulomb calculation including all interaction terms for $LiOsO_3$ should yield numerically almost equivalent results for two different bases. There may be small differences due to the fact that the unit cell contains six atoms which have inter atom one-particle terms. Though transformed, these are not taken into account on the level of the CT-QMC impurity solver. The CT-QMC solver calculates the result for each atom separately and upfolds the results to the unit cell (2.25). Inter-atomic terms are taken into account on the DMFT level. Therefore, a rotated calculation in one basis might not be fully consistent with a calculation in another basis. This is yet not fully probed and understood.

3.1.1 Comparing the Numeric Setup in both Bases

Before turning to the results obtained in the locally diagonal basis and comparing them to the results of a calculation in the standard basis, it is worth to investigate the differences in the initial setup, i.e. the local one-particle Hamiltonian and the local interaction Hamiltonian. This calculation does not include SOC and is therefore not spin dependent. All orbitals displayed are without spin dependency.

A comparison of the local one-particle coefficients of the Hamiltonian of atom 1 is displayed in Figure 3.1. For the other 5 atoms the result is almost the same. In the standard LS basis the 3 t_{2g} orbitals are energetic degenerate where the exact value is not important because it is corrected by the chemical potential and only differences between the orbitals influence the physical dynamics in the material. The off-diagonal terms of the size 80 meV can be compared to the interaction coefficients displayed for the Kanamori approximation in Table 3.1. Compared to the smallest interaction parameter (J=260 meV) this is 30 %, compared to the largest (U=2.410 eV) this is

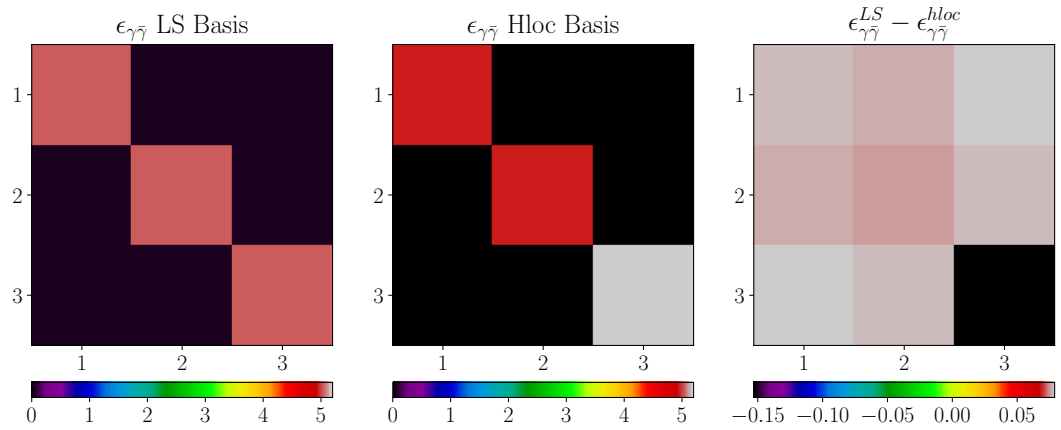

Figure 3.1: Graphical comparison of the matrix entries of $\epsilon_{\gamma\bar{\gamma}}$ of the first atom for the standard (LS) and the locally diagonal (Hloc) basis. Eigenvalues in the LS basis are: 5.045 eV, 5.042 eV, 5.047 eV. Eigenvalues in the Hloc basis are: 4.967 eV, 4.967 eV, 5.200 eV.

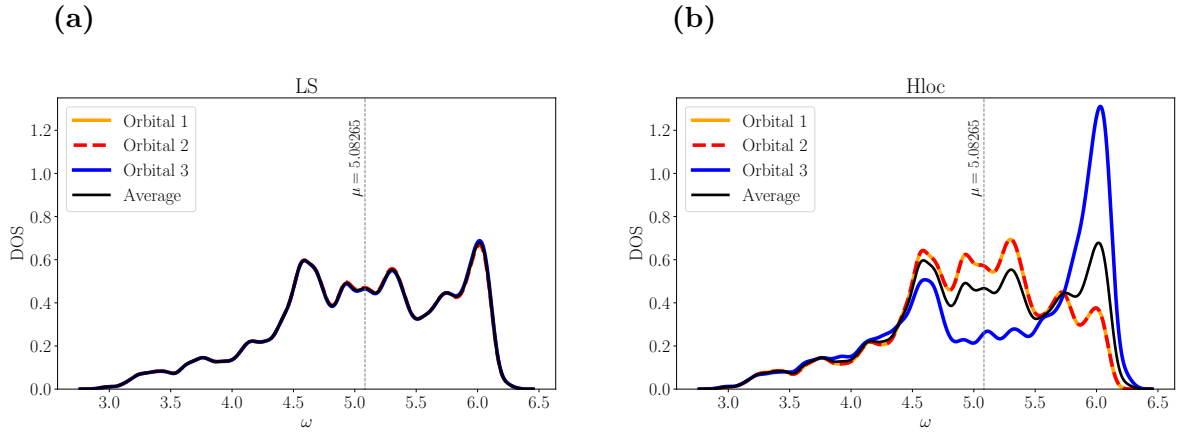

Figure 3.2: Comparison of the LDA density of states of the first atom in the standard LS and locally diagonal (Hloc) basis. The differences are significant. The third orbital exhibits a huge shift of weight towards $\omega = 6$, whereas orbital 1 and 2 shift to the interval $[4.5; 5.5]$ in the locally diagonal basis.

3.3 %. In the locally diagonal basis only two of the three t_{2g} orbitals are degenerate with an energy splitting of 230 meV to the third orbital. This is already about 80 % of the smallest (J=290 meV) and about 10 % of the largest (U=2.350 eV) interaction parameter in this basis and seems to be less negligible then the off-diagonal terms in the standard basis. This non-degeneracy is also well displayed in the LDA DOS corresponding to the one-particle Hamiltonian of atom 1 in the locally diagonal basis. The LDA DOS for both bases are shown in Figure 3.2. The degeneracy of the three orbitals in the standard basis is well pronounced. However, in the locally diagonal basis the spectral weight of orbital 3 gets drastically shifted from the proximity of the chemical potential towards higher frequencies whereas for orbital 1 and 2 it gets shifted from high frequencies to the proximity of the chemical potential. Therefore, in the locally diagonal basis, orbitals 1 and 2 will be more populated than orbital 3 resulting in a *non* half-filled system per orbital and therefore in a weakening of the Hund's localization.

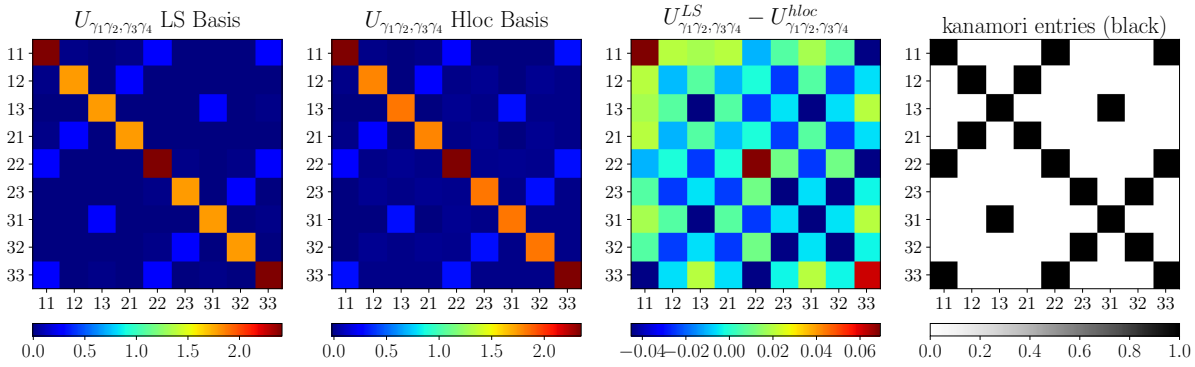

Figure 3.3: Graphical comparison of the matrix entries of $U_{\gamma_1\gamma_2\gamma_3\gamma_4}$ of the first atom without spin dependency for the standard (LS) and the locally diagonal (Hloc) basis. The panel to the right shows the entries corresponding to the Kanamori Approximation. The indices $\gamma_1\gamma_2$ and $\gamma_3\gamma_4$ are combined on the x and y-axis.

Parameter	LS	Hloc
U	2.412 eV	2.346 eV
V	1.791 eV	1.824 eV
J	0.261 eV	0.294 eV

Table 3.1: This table shows the Kanamori parameters for $LiOsO_3$ in two different bases in eV. The standard (LS) and locally diagonal (Hloc) basis. The Hubbard U in the Hloc basis is slightly lower indicating less localization, however, the Hund's Parameter J is slightly higher indicating more localization if the orbitals population is still approximately 0.5. Hence, it is a priori not possible to predict which basis will show more localizing effects.

The rotation of the one-particle Hamiltonian into a locally diagonal basis in Kanamori approximation, thus, is expected to lead to an overall delocalizing effect. In order to fully understand the effects of the rotation we now turn to the differences in the local interaction term. The coefficients and their differences are visualized in Figure 3.3 in the first three panels from the left. The panel to the right shows the coefficients contributing to the Kanamori approximation in black. Switching from the LS to the Hloc basis the local Hubbard U slighlty decreases, whereas all other Kanamori terms slightly increase. Averaging over the Kanamori entries to obtain U, V, J as in eq. (1.2) yields the values displayed in Table 3.1. The decrease of the Hubbard U by about 60 meV is opposed by an increase of V by about 30 meV and the increase of the Hund's parameter J by about 30 meV. In general a decrease in the Hubbard U yields a delocalization, however, for half filled orbitals a slight increase in the Hund's exchange parameter J favors a strong localization of charge carriers. It is a priori not clear whether a Kanamori approximated DMFT calculation of $LiOsO_3$ in the locally diagonal basis will yield a more or less metallic result then a calculation in the standard basis. However, the increases of J is also opposed by a loss of the t_{2g} degeneracy, yielding non half-filled orbital. The combination of all these factors suggests that the results of a Kanamori approximated DMFT calculation in the locally diagonal basis could indeed yield results more compatible with the full Coulomb calculation, which are more metallic.

3.2 Results for a Paramagnetic, Kanamori Approximated Calculation in the Locally Diagonal Basis

In this chapter we present the results of a paramagnetic, Kanamori approximated calculation at half filling in the locally diagonal basis and compare it to a calculation in the standard basis. All calculations have been performed with the w2dynamics [17] package. The input k-dependent one-particle coefficient matrix and the local interaction coefficient matrices in the standard basis was obtained with the VASP package [11–14] by the group of Professor Cesare Franchini at the University of Vienna and then rotated to the locally diagonal basis with the scripts of Appendix E and F. The Kanamori parameters used for this calculation are displayed in Table 3.1. All calculations are not spin dependent. For convenience we display only one spin channel in all figures. All analytic continuations are performed with the Maxent solver from the ALPS package [18]. All graphics display only the results of atom 1, because atom 2 shows very similar behavior.

As first result Figure 3.4 shows the diagonal entries of the imaginary part of the local self-

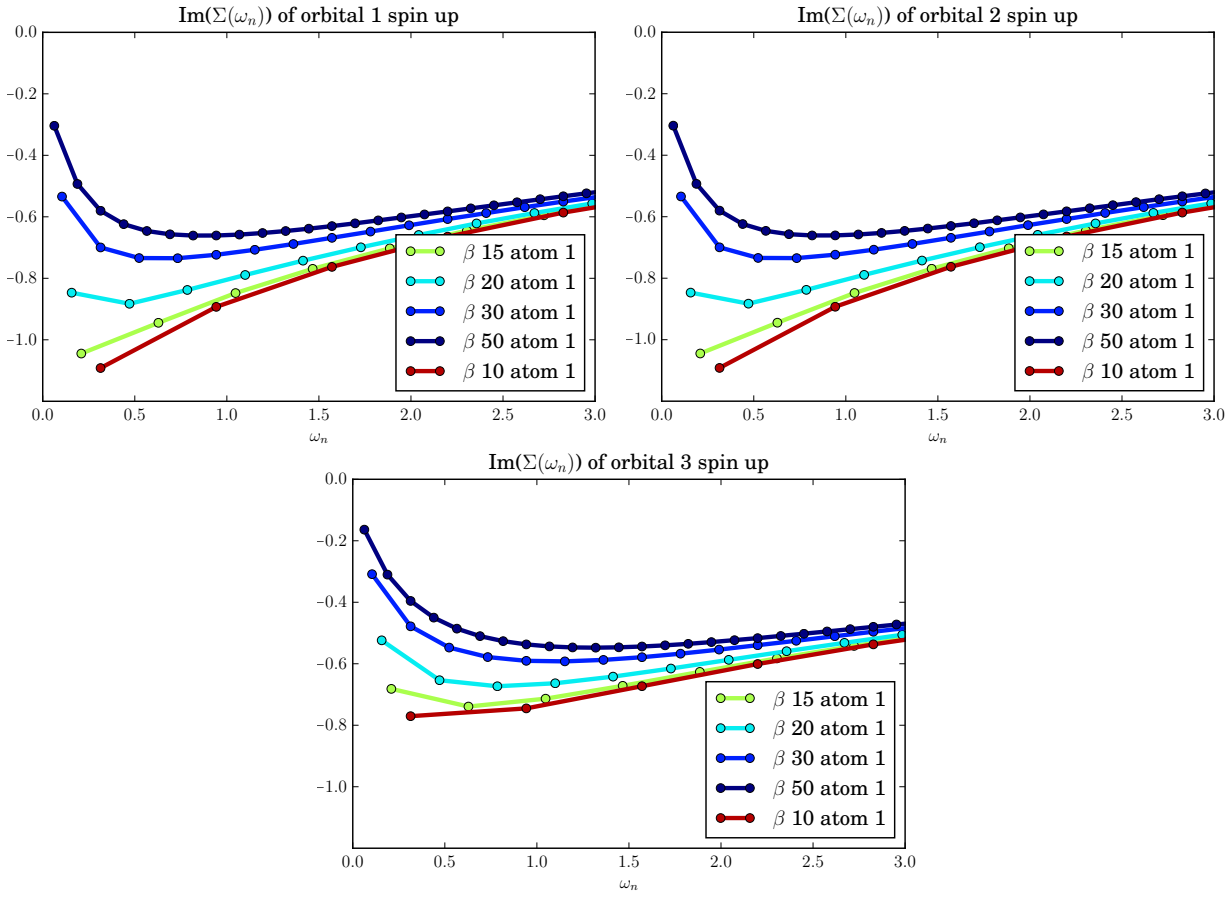

Figure 3.4: Diagonal entries of $\mathrm{Im}[\Sigma_{\gamma\bar{\gamma}}(\omega_n)]$ of $LiOsO_3$ in the locally diagonal basis, where $\beta = \frac{1}{k_b T}$. Orbitals 1 and 2 are degenerate and show a localizing behaviour for $\beta = 10, 15$ i.e. a positive slope close to $\omega_n = 0$. However, for orbital 3 only $\beta = 10$ shows a slightly positive slope around $\omega_n = 0$. It is not clear whether the high temperature trend is enough to display strong localization effects, especially for the third "a1g" orbital.

energy $\Sigma_{\gamma\bar{\gamma}}(\omega_n)$ on the Matsubara frequency axis for various temperatures i.e. β values. Orbital 1 and 2 (upper pannels) are degenerate and therefore the self-energies are equal. For those two orbitals $LiOsO_3$ displays a metallic behaviour for $\beta = 20, 30, 50$ and a bad metal behaviour for $\beta = 10, 15$, since the slope of the local self-energy is positive close to $\omega_n = 0$. In comparison, for orbital 3 the local self-energy has only for $\beta = 10$ a slightly positive slope close to $\omega_n = 0$ i.e. is shows a more metallic behaviour then the other two orbital. However, the visible trends are not pronounced enough to conclude the behaviour of $LiOsO_3$ at high temperatures directly from the local self-energy. To get a better understanding, Figure 3.5 shows the diagonal elements of the imaginary part of the Matsubara Green's function $G_{\gamma\bar{\gamma}}$ on the Matsubara axis. The upper panels of Figure 3.5 show orbital 1 and 2. The trend visible in the local self-energy is also visible in the Matsubara Green's function which displays a loss of weight around $\omega_n = 0$ for decreasing β, i.e. increasing temperature, indicating a bad metal behaviour. The positive slope in the self- energy close to $\omega_n = 0$ is not enough to change the slope in the Matsubara Green's function, which would represent a stronger indication for a pseudogap i.e. insulating behaviour. The temperature

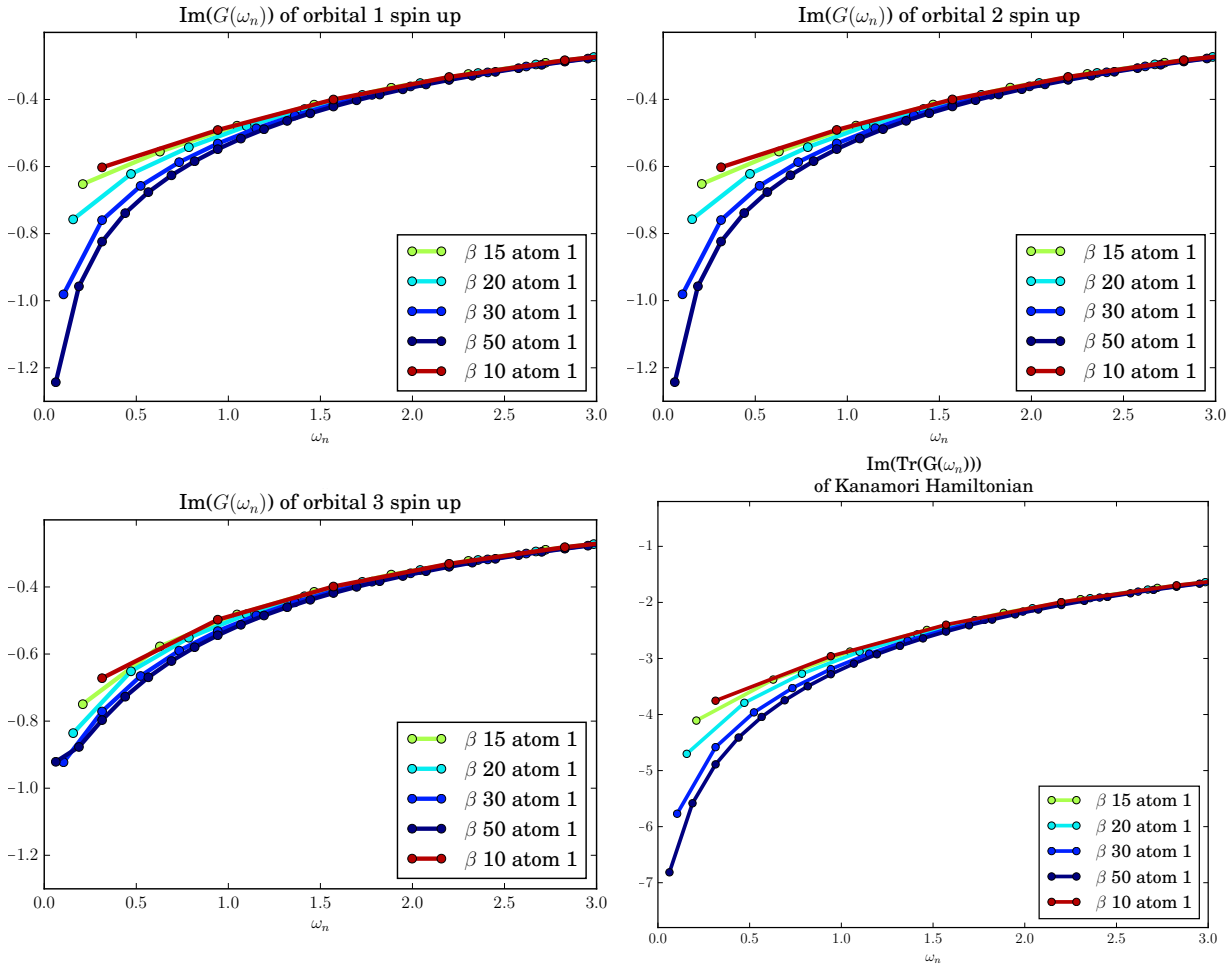

Figure 3.5: Diagonal entries of $\mathrm{Im}[G_{\gamma\bar{\gamma}}(\omega_n)]$ and the trace $\mathrm{Im}[G_{\gamma\bar{\gamma}}(\omega_n)]$ of $LiOsO_3$ in the locally diagonal basis, where $\beta = \frac{1}{k_b T}$. All orbitals display a metallic character i.e. the Green's function has significant weight around $\omega_n = 0$. The high-temperature trend, however, is towards a bad metal.

dependence of orbital 3 (lower left of Figure 3.5) is overall much less pronounced then for orbitals 1 and 2. The trace over all diagonal entries of the Matsubara Green's function is displayed in the lower right panel and shows a metallic slope for low temperatures inherited from the two energetic lower lying orbitals (1 and 2). Overall a gradual tendency towards a bad metal as temperature increases can be seen.

To understand where this tendency comes from we take a look at the occupancies displayed in Figure 3.6. As indicated by the split of the t_{2g} degeneracy by 230 meV the energetic lower lying orbitals 1 and 2 are more populated then the higher lying orbital 3 (upper right panel). This difference decreases with decreasing β, i.e. increasing temperature as higher temperature provides more thermal energy to lift electrons from the lower orbitals to the higher orbital. The orbital splitting is also reflected in the absolute value of the double occupancy (upper left panel), which increases for orbitals 1 and 2 with respect to orbital 3, denoting the fact that more electrons

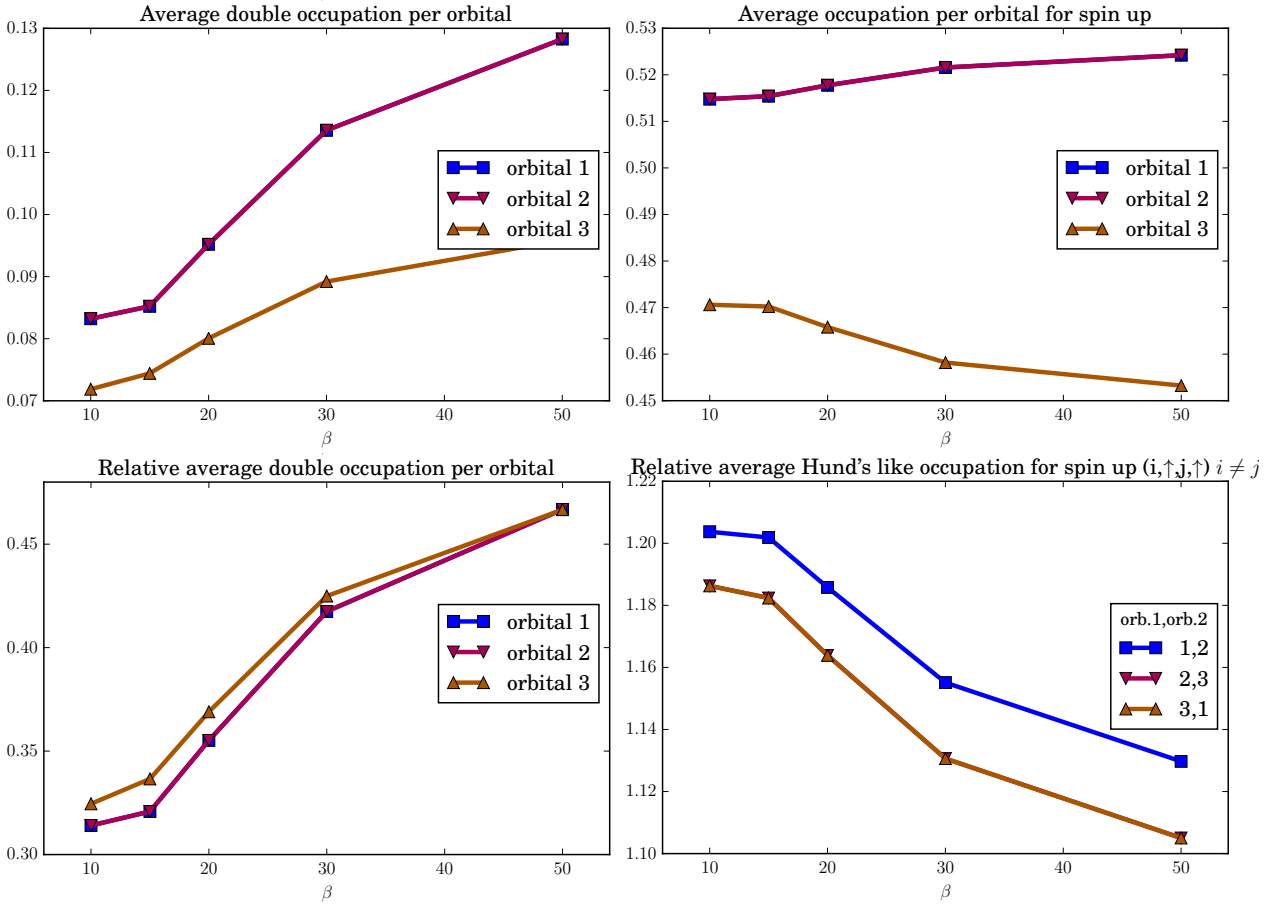

Figure 3.6: Occupancies of $LiOsO_3$, where $\beta = \frac{1}{k_b T}$ and "relative" refers to expression of the form $\frac{\langle n_\gamma n_{\bar{\gamma}} \rangle}{\langle n_\gamma \rangle \langle n_{\bar{\gamma}} \rangle}$. The average occupation per orbital shows the degeneracy of orbital 1 and 2, which are higher populated for the whole temperature range displayed. This difference decreases towards lower β. The relative double occupation and the relative Hund's like occupation (note that $i, j \equiv \gamma, \bar{\gamma}$) follow the same temperature trend for all orbitals but the opposite trend with respect to each other. Decreasing β lowers the double occupation as electrons become more mobile and start to populate the energetic higher orbital 3 with aligned spins.

populate orbital 1 and 2. The temperature trend for all orbitals is, however, qualitatively similar for all orbitals, especially for the most relevant parameter: the relative double occupancy (lower left panel). More specifically, as temperature increases the double occupancy decreases. This is opposed by the behavior of the relative Hund's like occupancy which shows an increase for increasing temperature. A decreasing double occupation paired with an increase in the Hund's like occupation is a strong indicator for localization of charge carriers in a per orbital half-filled system, driven by the Hund's exchange. In this basis, however, none of the orbitals is half-filled and we therefore have to inspect other quantities, such as the local Matsubara Green's function or the local spectral function.

Eventually the Matsubara results are continued to the real frequency axis yielding the local spectral functions shown in Figure 3.7. The energetic lower orbitals 1 and 2 (upper panels) display a quasi-particle peak for $\beta \geq 15$. For $\beta = 10$ the peak has vanished and left a dip formation indicating a bad metal behavior of this two orbital. The higher lying orbital 3 (lower left panel)

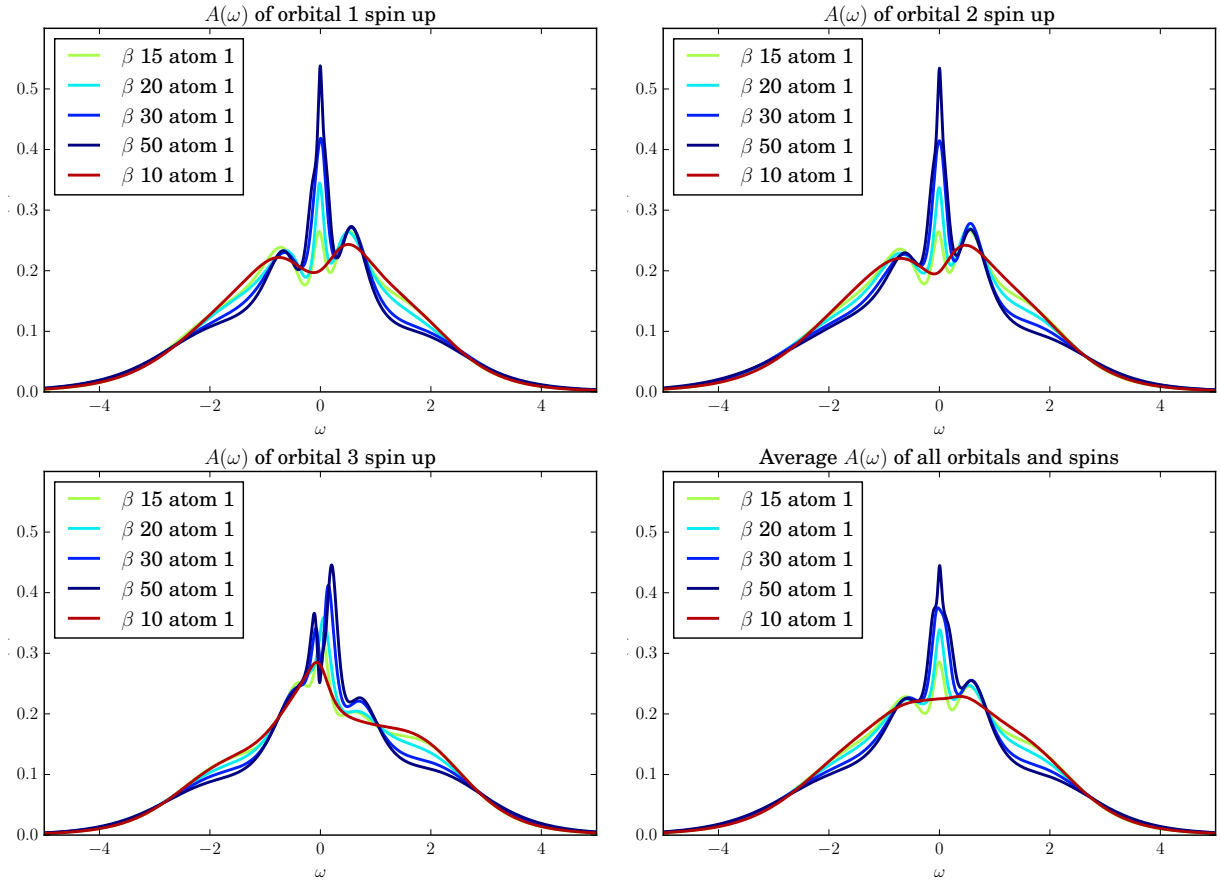

Figure 3.7: Diagonal entries of $A_{\gamma\bar{\gamma}}(\omega)$ and the average of $A_{\gamma\bar{\gamma}}(\omega_n)$ with respect to all orbitals and spins of $LiOsO_3$ in the locally diagonal basis, where $\beta = \frac{1}{k_b T}$. All orbitals display a metallic character i.e. the Green's function has significant weight around $\omega_n = 0$. The quasi particle peak in orbitals 1 and 2 quickly decreases as β decreases i.e. temperature increases. Orbital 3 does not display such a clear quasi-particle peak, but a significant asymmetry between $\omega < 0$ and $\omega > 0$. The average displays a quasi-particle peak for $\beta \geq 15$. However, for $\beta = 10$ the local spectral function around $\omega = 0$ is flat indicating a bad metal behaviour.

does display a quasi-particle peak for $\beta = 10, 15, 20$ and a dip for $\beta = 30, 50$. This dip, however, is only reflecting the decrease of spectral weight around μ in the non-interacting DOS of $LiOsO_3$ (compare Figure 3.2 right pannel). There is a well pronounced broadening of the spectrum with increasing temperature and also a formation of a flat level at $\omega > 0$. On average (lower right panel) the spectrum is perfectly flat around $\omega = 0$. The quasi particle peak has completely vanished.

The Kanamori results presented above show a temperature trend qualitatively consistent with the experimental results. However, the trend is much less pronounced than in the standard basis (Which was yielding a very good agreement with the experiments). A comparison of both bases is shown in Figure 3.8. The left panels show the results in the locally diagonal (Hloc) basis, the right panels show the results in the standard (LS) basis. In the standard basis all orbitals and spins are degenerate. Therefore, for the self energy and the Green's function only results of orbital 1 are displayed. The self energy (first row) shows huge differences for $\beta = 15, 20$. In the standard basis the self energy displays a clearly metallic behavior for $\beta = 30, 50$ and an almost insulating behavior for $\beta = 15, 20$. This rapid change is not exhibited in the locally diagonal basis, where the changes are a lot smaller and appear to be smooth. The high-temperature pseudogap behavior visible in the locally diagonal basis is not as well defined as in the standard basis. The difference between the two bases is also displayed in the Green's function (second row) and average local spectral function (third row). The Green's function shows an almost insulating behavior for $\beta = 20$ in the standard basis, however for $\beta = 15$ this trend is not continued. The locally diagonal basis does not show this change of trend, but a smooth transition towards a bad metal. This is best seen in the local spectral function, where in the locally diagonal basis the quasi-particle peak around $\omega = 0$ continuously vanishes at low β, i.e. high temperatures. In the standard basis this is not the case. Instead there is a sharp transition from a metal with a well pronounced quasi-particle peak to a bad metal with almost insulating character. For $\beta = 15, 20$ the local spectral function almost exhibits a gap at $\omega = 0$, i.e. it appears on the verge to a MIT.

A priori it is not clear which of the two bases provide the theoretical more accurate description. In the standard basis for the Kanamori approximation one neglects the off-diagonal one-particle matrix coefficients, which are responsible for the splitting of the t_{2g} manifold. However, in the locally diagonal basis the Kanamori parameters are different with respect to the standard basis. In order to decide which of the two bases is better suited to perform a Kanamori approximation it is necessary to take a look at the full Coulomb calculations which take into account the full one-particle coefficient matrix and the full interaction coefficient matrix and compare the results to the Kanampri approximated calculations presented in this chapter. This is the subject of the next section.

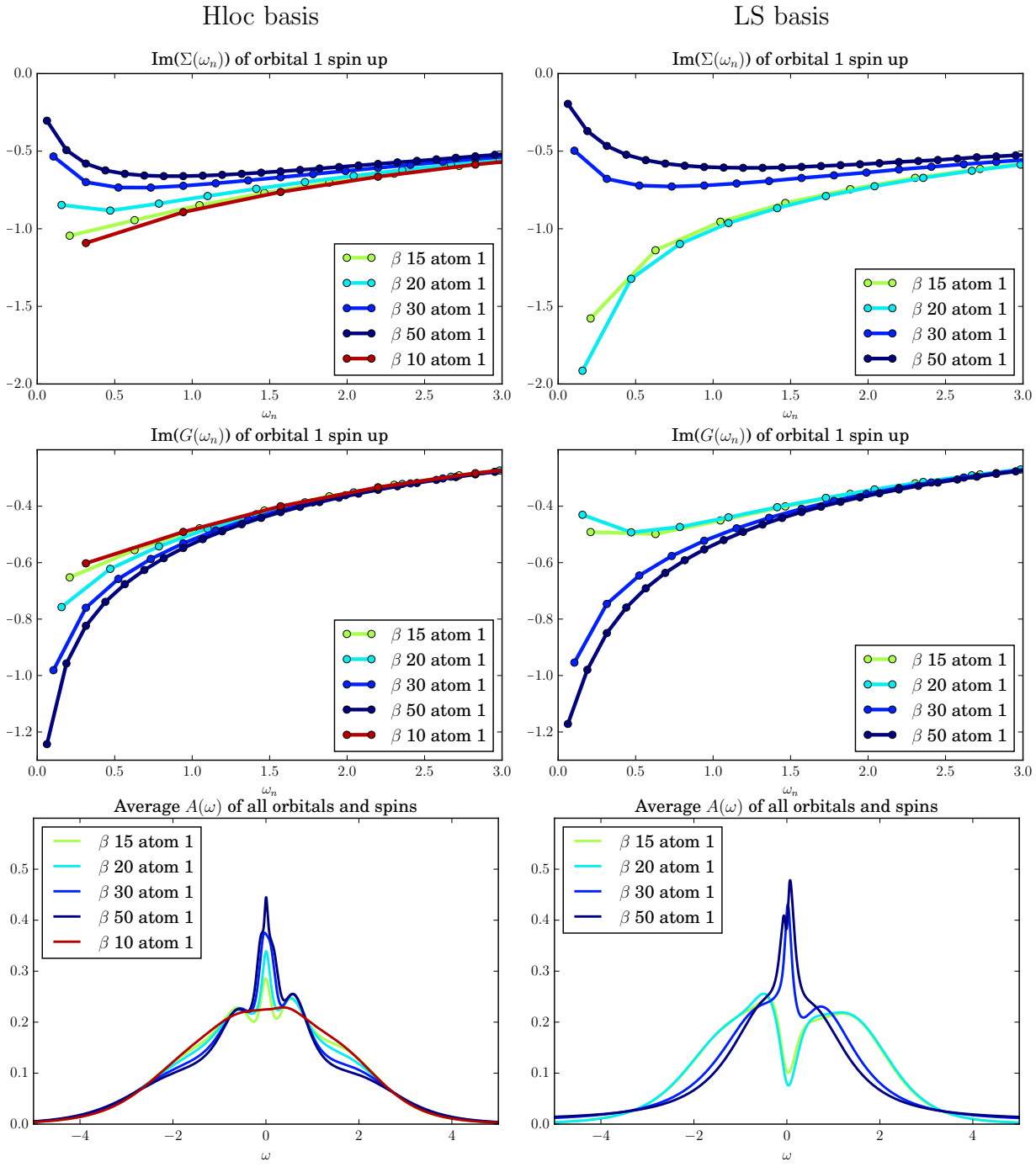

Figure 3.8: Comparison of the results of a Kanamori approximation in the locally diagonal basis (Hloc, left side) and the standard basis (LS, right side), where $\beta = \frac{1}{k_b T}$. Since in the LS basis all orbitals a degenerate only one orbital is displayed. The other orbitals of the locally diagonal basis are displayed in Figure 3.4 and Figure 3.5. The first row shows a comparison of the self energies, the second row a comparison of the Matsubara Green's functions and the third row of the averaged local spectral functions. In the standard basis the temperature trend is well pronounced in the self energy and Matsubara Green's function. It shows a sharp change of behavior between $\beta = 30$ and $\beta = 20$.

3.3 Results for a Paramagnetic, Full Coulomb Hamiltonian

In this chapter we present the results of a paramagnetic, full Coulomb DMFT calculation, meaning a calculation that takes into account the full one-particle coefficient matrix and the full interaction coefficient matrix, at half filling. This is the most general calculation possible on the level of DMFT. As example Table B.1 and Table B.2 show the local one-particle coefficients and the local interaction coefficients for atom 1. All other atoms have very similar coefficients, which is why this tables can be taken as example for all atoms. This calculations take significantly more time to converge then the Kanamori approximated calculation to reach the same accuracy, since now a lot more terms have to be included into the sampling routine.

In the following, the results of a full Coulomb calculation in the locally diagonal basis are presented. Again we display only the results of atom 1, because atom 2 is very similar. The full Coulomb result should not be basis dependent i.e. the results in an other basis should be obtained by rotation. We will verify this as an additional stringent benchmark of our calculations by comparing some of the results to a full Coulomb calculation in the standard basis.

In Figure 3.9 the diagonal elements of the local self-energy $\Sigma_{\gamma\bar{\gamma}}(\omega_n)$ (left side) and the diagonal elements of the Matsubara Green's function $G_{\gamma\bar{\gamma}}(\omega_n)$ (right side) are displayed. Both look very similar to the results of the Kanamori approximated calculation in the locally diagonal basis Figure 3.4, Figure 3.5. The local self-energy shows a trend towards a bad metal for low β values, i.e. high temperatures, as does the Matsubara Green's function. Orbitals 1 and 2 are degenerate and less metallic then orbital 3 which decreases its metallic characteristic slower. This trend continues in the local spectral function which is shown in Figure 3.10 row 3 and 4. With decreasing β the quasi-particle peak around $\omega = 0$ decreases and for $\beta = 10$ a dip evolves for orbitals 1 and 2 indicating the bad metal behaviour. However, orbital 3 does not display this behavior. The quasi-particle peak of orbital 3 (not visible for high β values (30, 50), which reflects the non-interacting DOS around μ shown in Figure 3.2.) is slightly pronounced for lower β values (10, 15, 20). At high temperatures orbital 3 appears to be more metallic than orbitals 1 and 2, though it is still less occupied (Figure 3.10). On average (lower right panel) a quasi-particle peak is observed, loosing coherence at higher β values until it essentially vanishes at $\beta = 10$. Further does the local spectral function shows progressive broadening of the central coherent peak with decreasing β. The double and Hund's like occupancy follow opposite temperature trends. With decreasing β, i.e. increasing temperature, the double occupancy decreases and Hund's like occupancy increases. A reason for this is the increased thermal energy which allows more charge carriers to populate the energetic higher lying orbital 3, where they tend to align spins with respect to orbitals 1 and 2. If all three orbitals are populated also spins in orbital 1 and 2 prefer to be spin aligned, as a result of the Hund's exchange. In fact, the more similar population of all three orbitals observed at higher temperatures enhances the Hund's driven tendency towards a more insulating behavior.

In summary, the full Coulomb calculation in the locally diagonal basis shows a definite trend towards a bad metal behavior for increasing temperature, which is in general consistent with the experimental results. However, the observed trend is only visible at temperatures much higher then in the experiments (1160 K in our calculations versus 300 K in the experiment).

Finally, the results of a full Coulomb calculation are in general not basis dependent. Of course it is necessary to rotate all quantities generated by the calculation from one basis to the other in order to compare. However, the trace over orbital and spin of an object e.g. $\mathrm{Tr}[G_{\gamma\bar{\gamma}}(\omega_n)]$ and $\mathrm{Tr}[A_{\gamma\bar{\gamma}}(\omega_n)]$ is basis independent and can be compared directly.

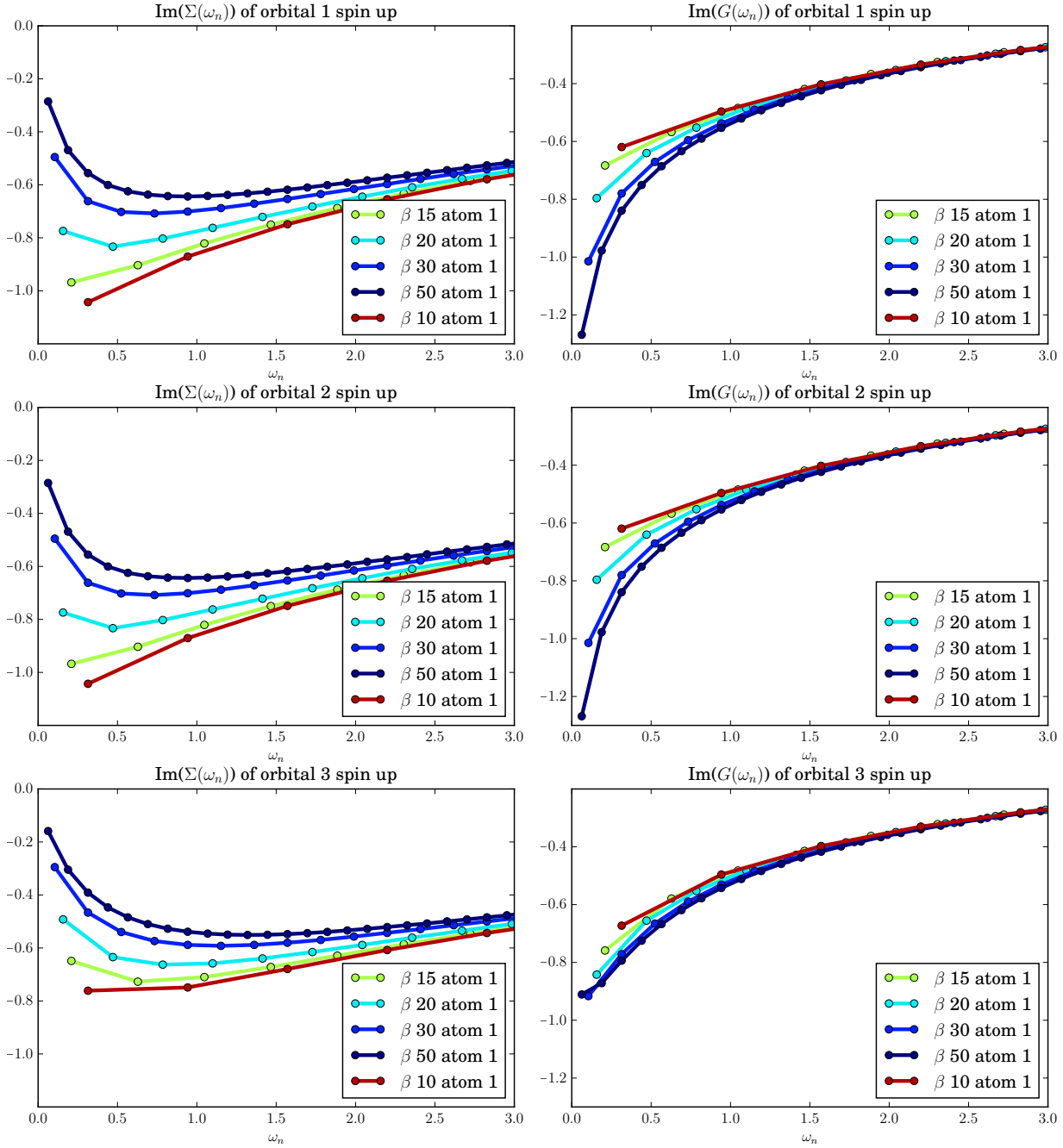

Figure 3.9: Diagonal entries of the local self-energy and Green's function of $LiOsO_3$ for a full Coulomb calculation in the locally diagonal basis. The similarity to the Kanamori approximated calculation in the locally diagonal basis displayed in Figure 3.4 and Figure 3.5 is self-evident.

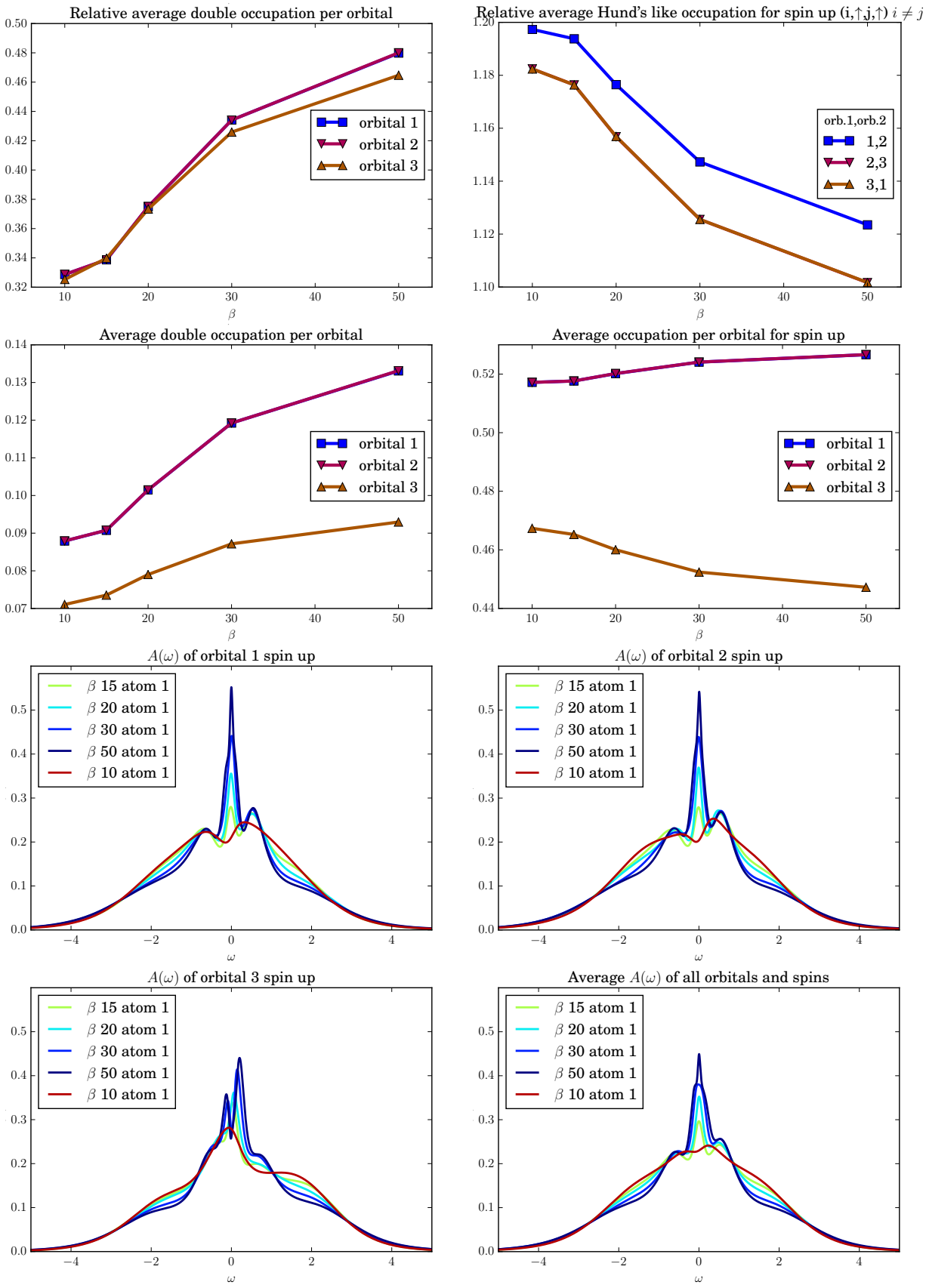

Figure 3.10: Occupancies and diagonal elements of the local spectral function of LiOsO3 for a full Coulomb calculation in the locally diagonal basis, where relative refers to expressions of the form $\frac{\langle \hat{n}_\gamma \hat{n}_{\bar{\gamma}} \rangle}{\langle \hat{n}_\gamma \rangle \langle \hat{n}_{\bar{\gamma}} \rangle}$.

A comparison of the result in the locally diagonal basis and the standard basis for atom 1 is shown in Figure 3.11. The left panels show the trace of the Matsubara Green's function (upper left) and the average local spectral function (lower left) in the locally diagonal (Hloc) basis. The right panels show the trace of the Matsubara Green's function (upper right) and the average local spectral function (lower right) in the standard basis. The Matsubara Green's functions show no visible difference for all β values displayed. The trend towards a bad metal is equally pronounced in both bases. Minor differences could be observed only in the analytically continued local spectral function, especially close to $\omega = 0$. For both analytic continuations the parameters where set equally. Therefore, these differences, not visible with the naked eye in the Matsubara

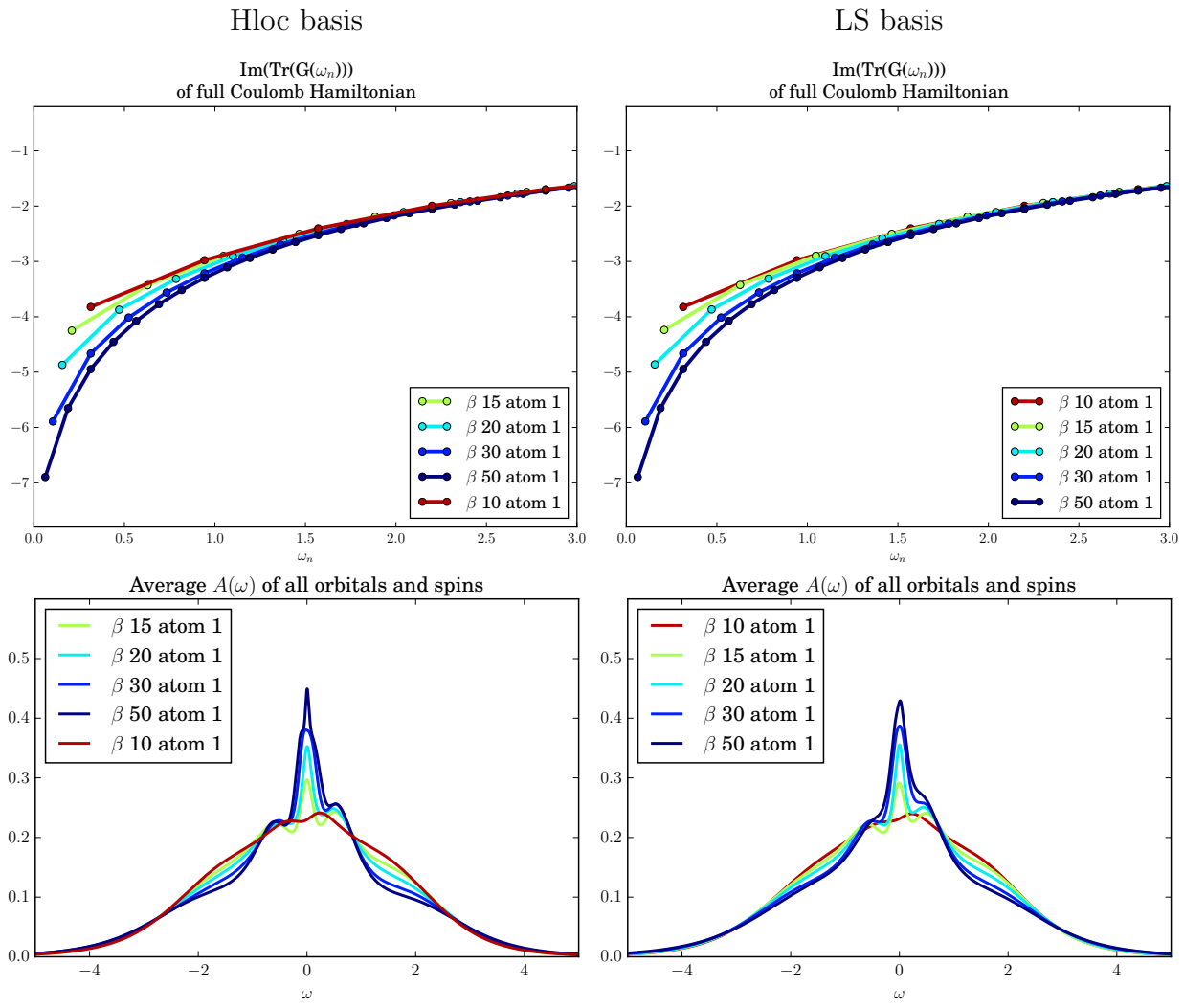

Figure 3.11: A comparison of the trace of the Green's function and the averaged local spectral function between the locally diagonal basis (Hloc, left side) and the standard basis (LS, right side) for a full Coulomb calculation. The trace of the Green's function shows almost no difference between the two calculations. The averaged local spectral function shows slight differences close to $\omega = 0$. Those come from the numerical analytic continuation, which is extremely input dependent i.e. very small differences in the Green's function can lead to visible differences in the spectrum.

Green's function, show how sensible the analytical continuation is w.r.t minimal differences of the input Green's function. The general trend and shape of the continued spectra is the same and consistent with the expected basis independence of the calculations.

Finally the results obtained from the full Coulomb calculation are to be compared to the Kanamori approximated calculations to see which basis is better suited for approximations. A side by side comparison of the Kanamori approximated calculation to the full Coulomb calculation in the standard basis is not displayed as the huge differences can be easily seen by comparing the right panel in the third row of Figure 3.8 (the average spectrum of the Kanamori approximated calculation in the standard basis) to the right panel of the second row of Figure 3.11 (the average spectrum of the full Coulomb calculation in the standard basis).

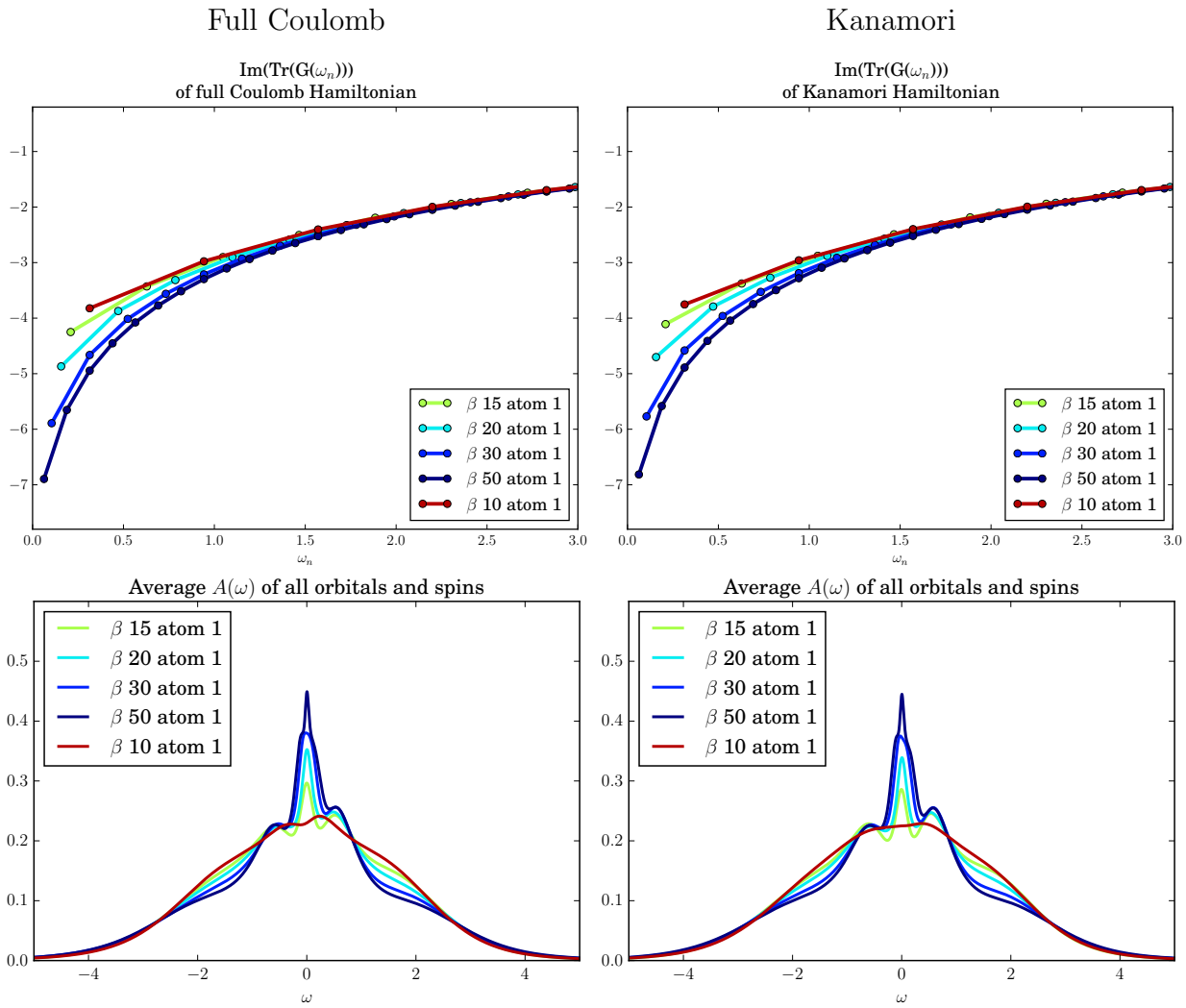

Figure 3.12: A comparison of the trace of the Green's function and the averages local spectral function between a full Coulomb (left side) and a Kanamori (right side) calculation in the locally diagonal basis. The Green's function display minimal differences close to $\omega = 0$. Those differences lead to small differences in the spectra, especially for $\beta = 10$ where the full Coulomb calculation shows a small dip and the Kanamori calculation is flat.

Instead, a side by side comparison of the Kanamori approximated calculation to the full Coulomb calculation in the locally diagonal basis is shown in Figure 3.12. In this case, the differences in the Matsubara Green's function (first row) are very small and only visible very close to $\omega_n = 0$. In general, the overall degree of agreement is remarkable. This is also reflected in the local spectral function (second row) where only for $\beta = 10$ a visible difference occurs. There the local spectral function of ω close to zero shows the onset of a dip in the full Coulomb calculation and a purely flat behavior in the Kanamori approximated calculation. The question which basis is better suited for making approximation, finds a clear favourite now. The locally diagonal basis seems the be the optimal choice as the degree of agreement to the full Coulomb calculation is remarkable. It appears that off-diagonal terms of about 80 meV of the diagonal terms are non-negligible in this case. The locally diagonal basis naturally incorporates these terms by a splitting of the t_{2g} degeneracy and so all approximated calculations, which neglect off-diagonal elements, are most accurate in this basis.

Chapter 4

Results with Spin-Orbit Coupling

In this chapter we present the DMFT results of a full Coulomb calculation including local spin-orbit coupling. In particular, we compare the effect of the addition of local (atom-like) spin-orbit terms to the one-particle Hamitlonian in the different bases introduced in the previous chapter. In general, a local spin-orbit coupling originates spin off-diagonal terms in the local one-particle coefficient matrix (1.3). As a practical consequence, our DMFT calculations can no longer be enforced to be paramagnetic, because in w2dynamics this is enforced by averaging over both spins. We find that $LiOsO_3$ shows a strong tendency towards antiferromagnetism and that local spin-orbit coupling is able to overcome this tendency, keeping the material in a paramagnetic phase as observed in experiments. However, both, the tendency towards a magnetically ordered state and its suppression, depend significantly on the basis in which the calculation is performed. In order to shed light on the underlying physics, we start by discussing the dependence of the eigenvalues of the local one-particle coefficient matrix on the strength of the local spin-orbit coupling (ξ). This shows that the energies of the t_{2g} orbitals in the locally diagonal basis further split up due to the local spin-orbit coupling. The estimated effect of this splitting is a further metallization, as it is the case in the Kanamori approximation in the locally diagonal basis. This is consistent with our results in the regime of the estimated strength of the local spin-orbit coupling. The results of the DMFT calculation, are structured into sections according to different bases in which the spin-orbit coupling is added and in which the calculations are performed. Each section contains subsections comparing results for either (i) varying temperatures and fixed ξ or (ii) varying ξ and fixed temperature (β).

In the following we present the results of the full Coulomb calculation including local (atomic-like) spin-orbit coupling in 4 different bases. 1.) The Wannier Hamiltonian in the standard basis supplemented with local spin-orbit coupling which will be referred to as standard (LS) basis. 2.) A basis where the Wannier Hamiltonian in the standard basis gets supplemented with local spin-orbit coupling and then diagonalized, which will be referred to as fully diagonalized standard (LS diagonal) basis. 3.) Since it is not clear in which basis the local spin-orbit coupling is to be added to obtain the best possible approximation, the third basis is the locally diagonal basis. Here we supplement the Wannier Hamiltonian, represented in the locally diagonal basis, with

local spin-orbit coupling. This basis will be referred as locally diagonal (Hloc) basis in agreement to the last chapter. 4.) A basis where the Wannier Hamiltonian represented in the locally diagonal basis gets supplemented with spin-orbit coupling and then diagonalized. This basis will be referred as fully diagonalised locally diagonal (Hloc diagonal) basis. The term supplemented with local spin-orbit coupling refers to adding (1.3) for every atom at every k point to the k-depended one-particle coefficient matrix (Wannier Hamiltonian).

In general eq. (1.3) can be naturally derived for a perfect t_{2g} Hamiltonian [41], which has no off-diagonal coefficients and is perfectly degenerate. Therefore, most probably the local spin-orbit coupling should be added in the locally diagonal basis, where, though not degenerate, the t_{2g} orbitals have no one-particle terms connecting them, i.e. the one-particle coefficient matrix is diagonal. The next section shows that the eigenvalues do not depend on the basis we choose to add the local spin-orbit coupling (the eigenvectors do).

4.1 Eigenvalues of the Local One-Particle Hamiltonian Extended with Spin-Orbit Coupling

The splitting of the t_{2g} degeneracy of $LiOsO_3$ is about 250 meV. An estimate of the local (atomic-like) spin-orbital coupling (SOC) strength on the Os atoms has been made to about 300 meV using DFT. This has been performed in the group of Cesare Franchini at the University of Vienna using VASP. The fact that those two energy scales have almost the same size rise hope that atomic-like spin-orbit coupling may counterbalance the loss of t_{2g} degeneracy, yielding a more localized system.

As first attempt to understand the influence of the local spin-orbit coupling we investigate the dependency of the eigenvalues of the local one-particle coefficient matrix on the spin-orbit coupling parameter ξ. Figure 4.1 shows the calculated eigenvalues on the ξ axis. In particular, the upper left panel shows the eigenvalues where the local spin-orbit coupling was added in the standard basis, the upper right panel shows the eigenvalues where the local spin-orbit coupling was added in the locally diagonal basis and the lower panel shows a direct comparison of both. Quite remarkably, we notice that all three panels show *equal* curves, i.e. the eigenvalues of the local one-particle Hamiltonian do *not* depend on the basis in which the local spin-orbit coupling is added. In the lower panel one can see that the eigenvalues in both bases are exactly the same. This does not mean that our DMFT calculations will yield the same result in these two cases, because the corresponding eigenvectors are unequal. It means, however, that the local "non-interacting" (one-particle) eigenenergies, corresponding to the same orbital numbering, are equal. Hence, the next observations will hold for all three panels. First, all eigenenergies come in pairs, i.e. two orbitals are energetically degenerate which we will denote by labeling them 12,12; 21,22; 31,32. Second, increasing ξ further splits the orbitals. The orbitals, which are energetic higher lying without spin-orbit coupling, get shifted to even higher energies and the orbitals, which are lower lying without spin-orbit coupling, to even lower energies. For large values of $\xi > 0.35$ meV this change is linear in ξ. A zoom of the non-linear regime (0 eV$< \xi <$ 0.35 eV) is

displayed in the insets. Third, the insets show how the 4 initially degenerate lower lying orbitals get split up in pairs of two which are for very high ξ are eventually separated by about 150 meV. For the realistic estimate of the spin-orbit coupling strength ξ of 300 meV the lower orbitals are split by 125 meV, which has to be compared to the 430 meV splitting between the upper two orbitals and the intermediate two orbital. This means that the two lowest lying orbitals will be most populated, whereas the occupation of the two intermediate orbitals will be lower and the

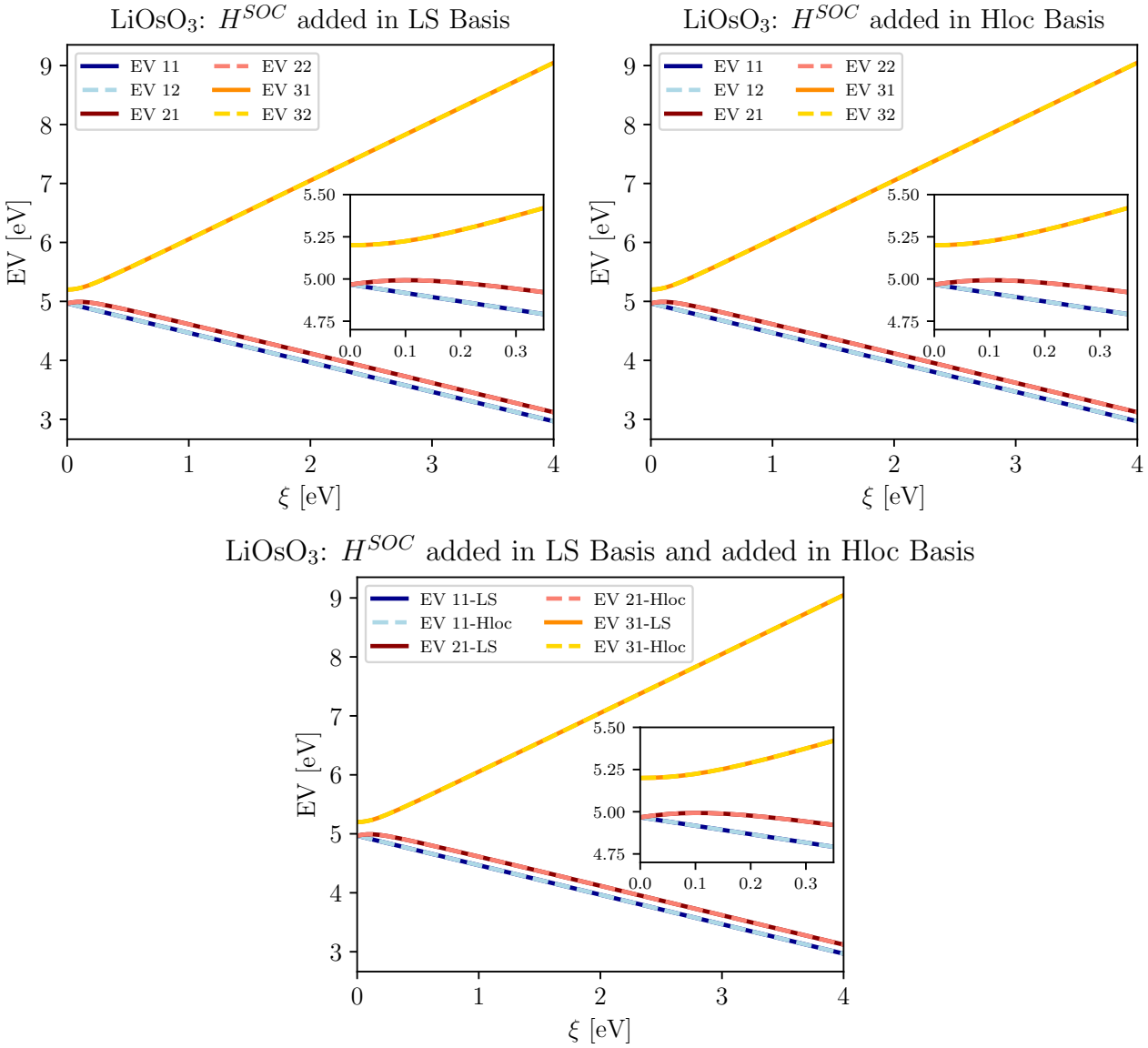

Figure 4.1: ξ dependence of the eigenvalues of the local one-particle coefficient matrix of atom 1. Spin-orbit coupling added in the standard (LS) basis (upper left panel), spin-orbit coupling add in the locally diagonal (Hloc) basis (upper right basis), comparison of both (lower panel). The eigenvalues are *independent* of the basis in which the spin-orbit coupling is added. Always two eigenvalues of the six in total are degenerate. The splitting of the t_2 degeneracy is increases with increasing ξ.

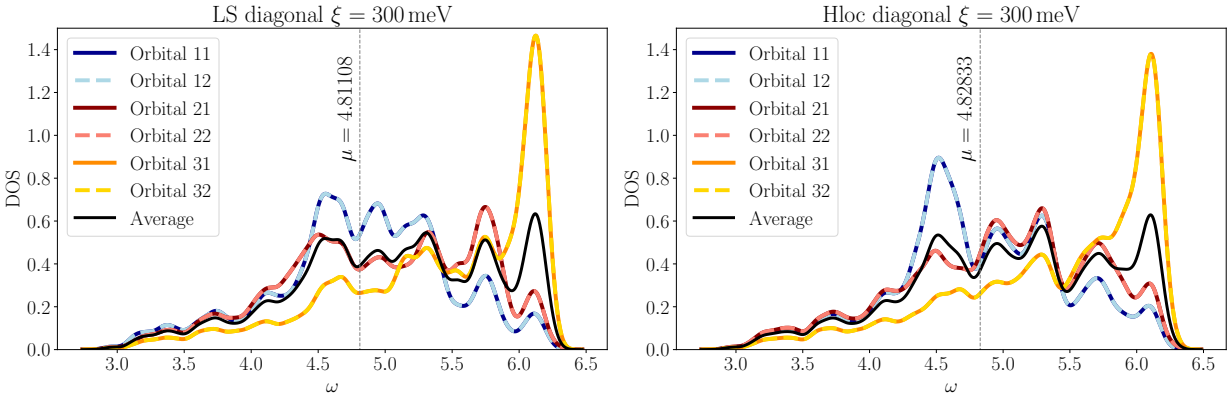

Figure 4.2: Orbital resolved density of state (DOS) derived by LDA for $\xi = 300\,\mathrm{meV}$ in the LS diagonal (left panel) and the Hloc diagonal (right panel) basis. Colors are chosen equivalent to Figure 4.1. The difference for ω close to μ is significant. In the LS diagonal basis the weight close to μ of the energetic lower lying orbitals is different, where in the Hloc diagonal basis it is not. Therefore orbitals 11 and 12 contribute more to charge transport than orbitals 21 and 22.

occupation of the highest orbital. will be lowest. The difference between the orbitals can also be seen in the corresponding (orbital resolved) LDA density of states, which is shown in Figure 4.2 for $\xi = 300\,\mathrm{meV}$. In the LS diagonal basis (left panel) the energetic lowest lying two orbitals have the most spectral weight around $\omega = \mu$, compared to the other orbitals. A lower spectral weight around the Fermi-level is found for the intermediate two orbitals and the lowest spectral weight for the energetic highest orbitals. The later, however, shows a large peak for large $\omega > 5.5$. Without considering the effect of electronic correlations, one would than expect that the highest lying orbitals 31 and 32 should contribute least to charge transport and orbitals 11 and 12 should contribute most. This situation is slightly different in the Hloc diagonal basis (right panel) where close to $\omega = \mu$ all four energetic lower lying orbitals have to same weight. This means that here one would expect orbitals 11, 12, 21, 22 to contribute equally to charge transport. The lowest orbitals have a significantly larger weight for $\omega < \mu$.

To sum it all up, the overall effect of introducing a local spin-orbit coupling term in $LiOsO_3$ further splits the t_{2g} manifold into three non-degenerate orbitals, i.e. it does *not* compensate for the initial splitting by the non-vanishing offdiagonal one-particle coefficients. Therefore, all orbitals will be even more away from satisfying the half-filling condition as it was already the case without local spin-orbit coupling in the locally diagonal basis. This effect increases with increasing ξ, which would suggest that, after all, local spin-orbit coupling makes $LiOsO_3$ more metallic. This expectation will be examined throughout this chapter.

4.2 Standard Basis Extended with Spin-Orbit Coupling

In this section we present all results computed in the standard (LS) basis. This means that spin orbit coupling is added in the standard basis, using the script from Appendix H. There is no diagonalization or rotation involved even when the DMFT calculation is eventually performed. An example parameters.in file for a spin-orbit calculation is in Appendix C, where the [Atom] section needs to be replaced with the [Atoms] section from the parameters.in file without spin-orbit coupling. All calculation have been performed with w2dynamics [17] on 480-800 cores on the Vienna Scientific Cluster (VSC3). Analytical continuations have been performed with Maxent [18] also on VSC3.

Calculations of $\beta \geq 10$ show an antiferromagnetic phase for a wide range of ξ parameters. This is also seen for $\beta = 15$. Therefor most of this section will focus on the influence of local spin-orbit coupling on the magnetic phase of $LiOsO_3$. At $\beta = 5$ it does not show an antiferromagnetic phase. This corresponds to 2320 K which is far above measured temperatures and $LiOsO_3$ is most probably melted at this point. The results of this calculation are presented in Appendix (A).

Most of the figures show only the results of atom 1, because the other atoms are similar. If this is not the case, more atoms are displayed. The same holds for the displayed orbitals.

4.2.1 $\beta = 10$

This subsection contains results for ξ values in the range of 0-8 eV [1] for $\beta = 10$, i.e. T=1160 K. Already at such a high temperature $LiOsO_3$ displays a strong tendency towards an antiferromagnetic phase, as it is displayed in Figure 4.3. The left side shows the occupancies for spin up (upper panel) and spin down (lower panel) of atom 1, the right side shows the occupancies for spin up (upper panel) and spin down (lower panel) for atom 2. The ξ dependence of the atoms (1 and 2) is inverse to each other, as it is for the spins within one atom. For $\xi < 500$ meV $LiOsO_3$ shows an antiferromagnetic phase, which rapidly vanishes for ξ between 400 meV and 500 meV. In fact, it appears that local spin-orbit coupling is capable of driving the CT-QMC calculation towards a paramagnetic solution. It is yet not fully understood where and why such a strong antiferromagnetic phase originates and whether it is to be trusted as possible thermodynamically stable solution. To try and shed some light into this, Figure 4.4 displays the diagonal elements of the imaginary part of the local self-energy (upper panels) and diagonal elements of the imaginary part of the local Matsubara Green's function (lower panels) of orbital 1 for spin up (left panels) and spin down (right panels). All other orbitals show equivalent behavior. The local self-energy shows a metallic behaviour for all displayed values of ξ for both spins, i.e. the antiferromagnetic behavior is not reflected in $\mathrm{Im}[\Sigma_{\gamma\sigma,\bar{\gamma}\bar{\sigma}}]$. However, there is a trend towards larger values for the first few Matsubara frequencies for 0 meV$< \xi <$ 500 meV which reverses for $\xi >$ 500 meV. The local Matsubara Green's function does display the same behavior for both spin channels. However, the antiferromagnetic phase for $\xi <$ 500 meV clearly induces an insulating character which is reflected in the slope of the Matsubara Green's function close to $\omega_n = 0$. The local Matsubara Green's

[1] Most of the figures show results from 0-2 eV. Of course a coupling strength larger than 1 eV does not refelct a realistic situation, however, in order to make a trend study we also include this results.

function shows a smooth transition from an insulating shape $\xi = 0\,\text{meV}$ to a metallic shape $\xi = 600\,\text{meV}$. For larger values of ξ this trend reverses and the Green's function slowly decreases again. However, this happens in a regime which is not realistic. Since the insulating behavior is not reflected in the imaginary part of the diagonal elements of the local self-energy, but only in the local Matsubara Green's function, it has to be induced by non-vanishing elements of the off-diagonal local self-energy or by the respective real part of the diagonal elements. Eventually, the behavior of the local Matsubara Green's function describes the physical behavior.

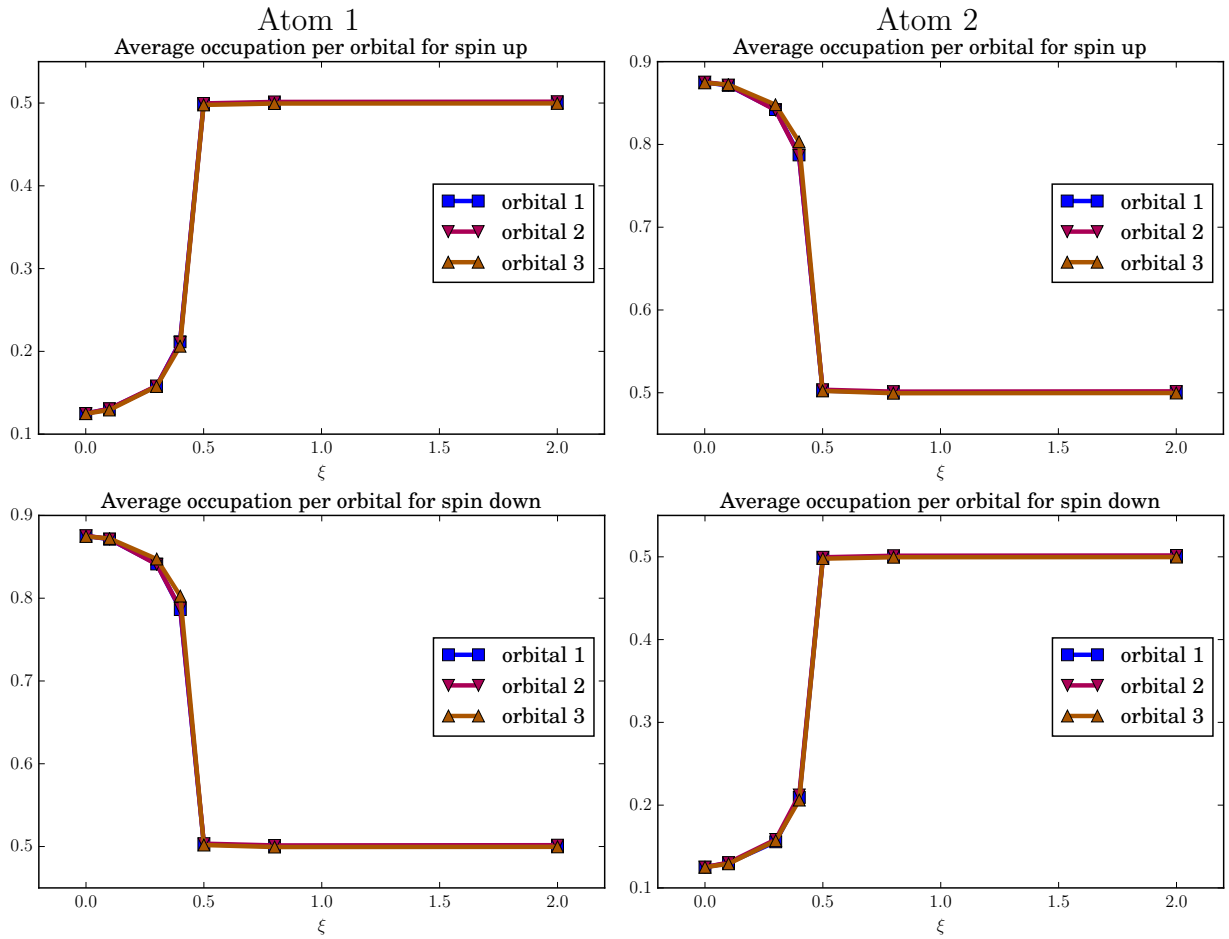

Figure 4.3: ξ (eV) dependence of the occupancies of the orbitals and spins at $\beta = 10$ for atom 1 (left panels) and atom 2 (right panels) in the LS basis. For $\xi < 500\,\text{meV}$ LiOsO3 shows antiferromagnetic behavior, which is gradually decreased from $0\,\text{meV} < \xi < 400\,\text{meV}$ and rapidly vanishes between $400\,\text{meV} < \xi < 500\,\text{meV}$. For $\xi \geq 500\,\text{meV}$ $LiOsO_3$ shows a paramagnetic phase. It appears that spin-orbit coupling strongly decreases the antiferromagnetic tendency of $LiOsO_3$.

Finally, Figure 4.5 displays the average sign of the CT-QMC sampling of atom 1. It rapidly decreases with increasing ξ, reaching its minimum of 0.25 at $\xi = 2\,\mathrm{eV}$, after which it slowly increases again. The decrease in the beginning is significant and this also decreases the calculations accuracy. This can only be overcome at the price of increasing the statistical parameters i.e. the number of measurements in the CT-QMC sampling, raising legitimate concerns about calculations at lower temperatures. However, at least for small spin-orbit coupling strength the sign stays at reasonable levels e.g. at $\xi = 300\,\mathrm{meV}$ the average sign is 0.7.

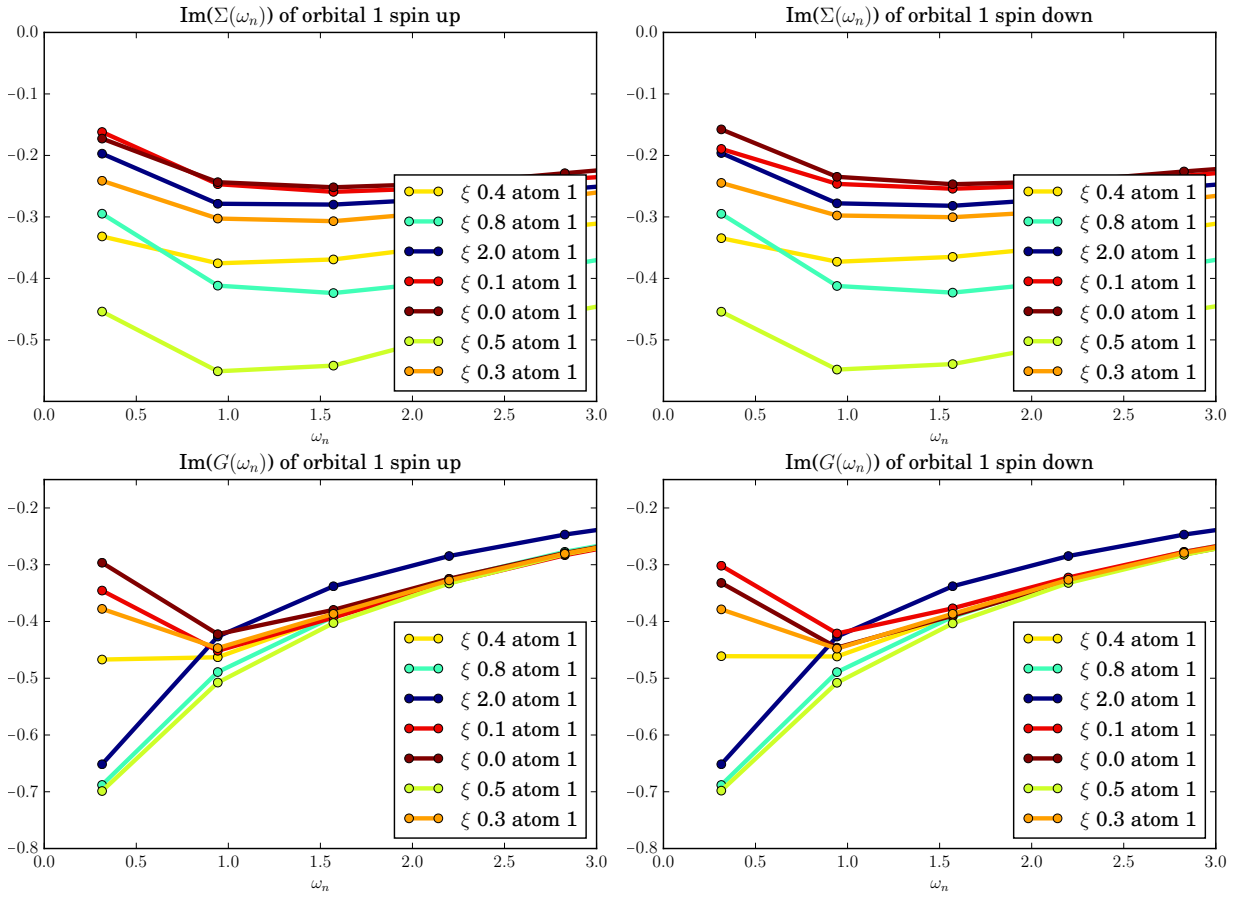

Figure 4.4: Diagonal entries of $\mathrm{Im}[\Sigma_{\gamma\sigma,\bar{\gamma}\bar{\sigma}}]$ (upper panels) and diagonal entries of $\mathrm{Im}[G_{\gamma\sigma,\bar{\gamma}\bar{\sigma}}]$ (lower panels) of orbital 1 (all other orbitals a similar) of atom 1 for various vales of ξ (eV). Neither in the self energy nor in the local Matsubara Green's function the differences of occupation from spin up and down (Figure 4.3) are visible. Although the local self-energy does not display an insulting character the local Matsubara Greens function does for $\xi < 500\,\mathrm{meV}$.

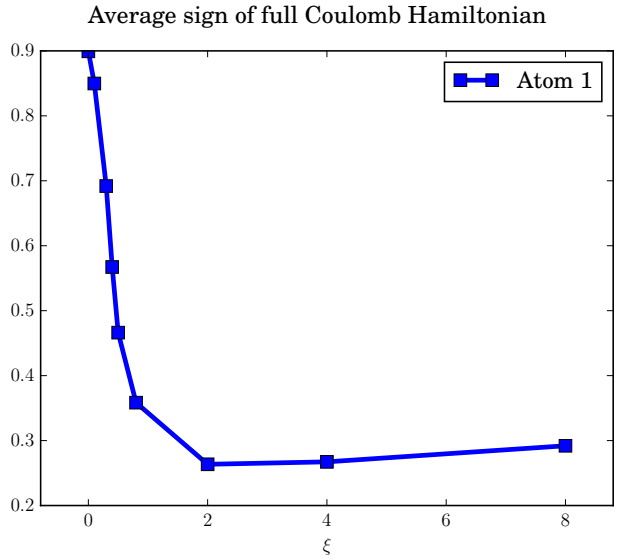

Figure 4.5: ξ (eV) dependence of the average sign of the CT-QMC sampling of atom 1 for $\beta = 10$. The rapid breakdown with increasing ξ is significant. At $\xi = 2$ it reaches a minimum of about 0.25 and it slowly increases for larger ξ.

4.2.2 $\beta = 15$

This subsection contains results for ξ values in the range of [0,8] eV [2] for $\beta = 15$, i.e. T=580 K. The average occupancies of all 3 orbitals and both spin channels are displayed in Figure 4.6 for both atoms. As for $\beta = 10$ it shows antiferromagnetic behavior for low values of ξ. However, the tendency is slightly stronger at $\beta = 15$, since for $\xi = 500$ meV the material is still antiferromagnetic and only at $\xi = 600$ meV it becomes paramagnetic again. Also the transition to a paramagnetic phase is not as s sharp as for $\beta = 10$. In Figure 4.7 both spins of the diagonal term of orbital 1 of the imaginary part of the local self-energy (upper panels) and the local Matsubara Green's function (lower panels) are displayed. The spin dependence of the occupancies is not inherited to neither the diagonal terms of the imaginary part of the local self-energy nor the diagonal terms of the imaginary part of the local Matsubara Green's function, as it was already the case at $\beta = 10$. The local self-energy displays a metallic behavior for all ξ and reverses its trend at $\xi = 0.6$ eV, where also the antiferromagnetic phase vanishes. The non smooth behavior of the local self-energy at $\xi = 2$ eV is induced by the very low average sign (0.09) (see Figure 4.8). In contrast to the metallic slope of the local self-energy the local Matsubara Green's function show a clearly insulting slope for $\xi \leq 500$ meV with a very sharp transition to a metallic shape at $500 <$ meV$\xi = 600$ meV. This also coincides with the onset of the paramagnetic phase. For even larger coupling strengths the local Matsubara Green's function shows a slightly insulating trend.[3]

The average sign of the CT-QMC sampling is displayed in Figure 4.8 and shows a rapid

[2] As in the previous subsection most figures display only results for ξ from 0 to 2.

[3] Since the estimated local (atomic) coupling strength is about 300 meV, those cases, where we observe an insulating trend, are probably unrealistic and shall only be understood as a trend study.

decrease with ξ. It reaches its minimum of 0.09 at $\xi = 2\,\mathrm{eV}$ and stays almost constant at this level for higher ξ. For $\xi \geq 2\,\mathrm{eV}$ calculation for even lower temperature are probably going to fail, unless an already converged solution from higher temperatures is used as a starting point.

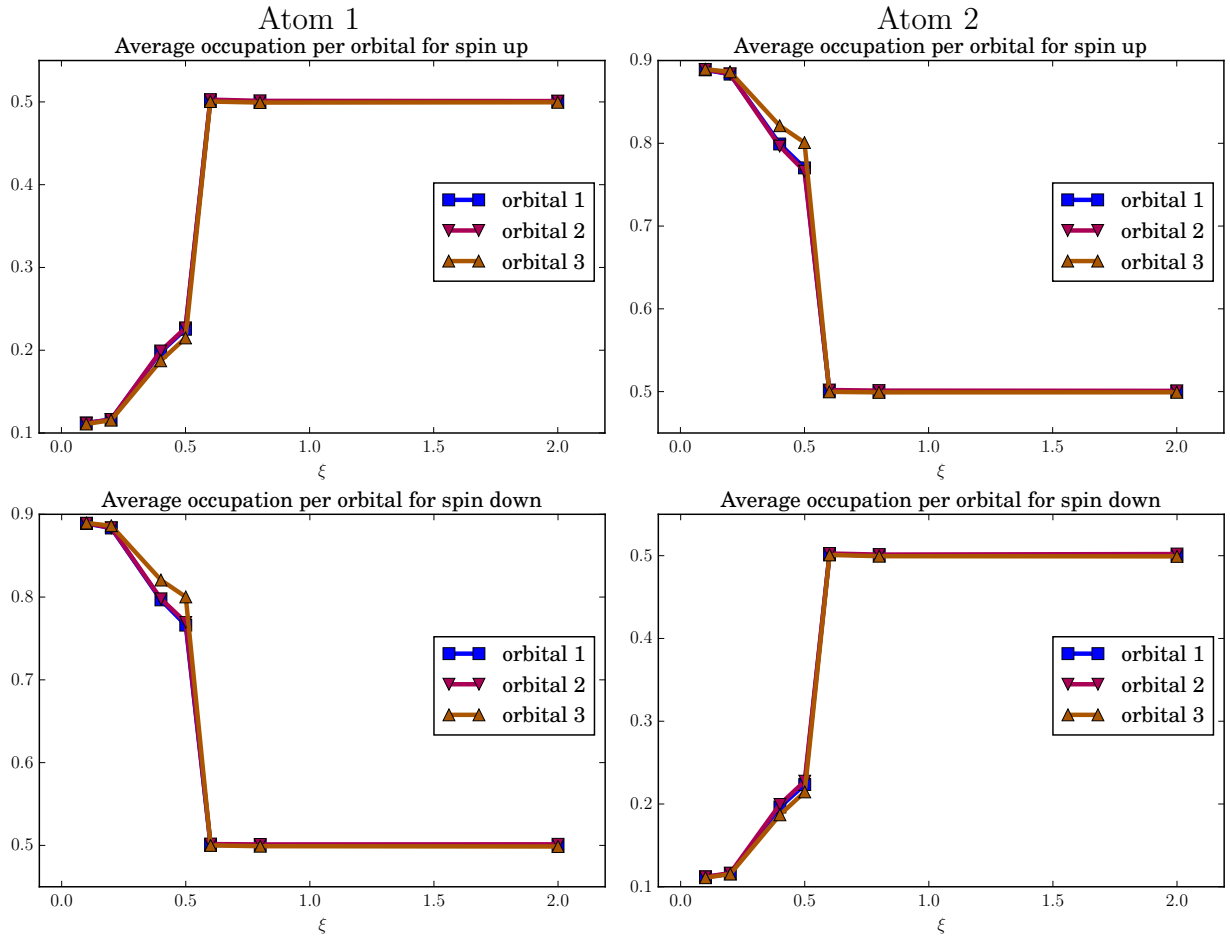

Figure 4.6: ξ (eV) dependence of the occupancies of the orbitals and spins at $\beta = 15$ for atom 1 (left panels) and atom 2 (right panels) in the LS basis. For $\xi < 600\,\mathrm{meV}$ $LiOsO_3$ shows antiferromagnetic behavior, which rapidly vanishes between $500\,\mathrm{meV} < \xi < 600\,\mathrm{meV}$. As the $\beta = 10$ calculation (Figure 4.3), the local spin orbit coupling decreases the antiferromagnetic tendency. Due to the lower temperature the spin-orbit coupling needs to be increased about 100 meV in order to obatin a paramagnetic solution.

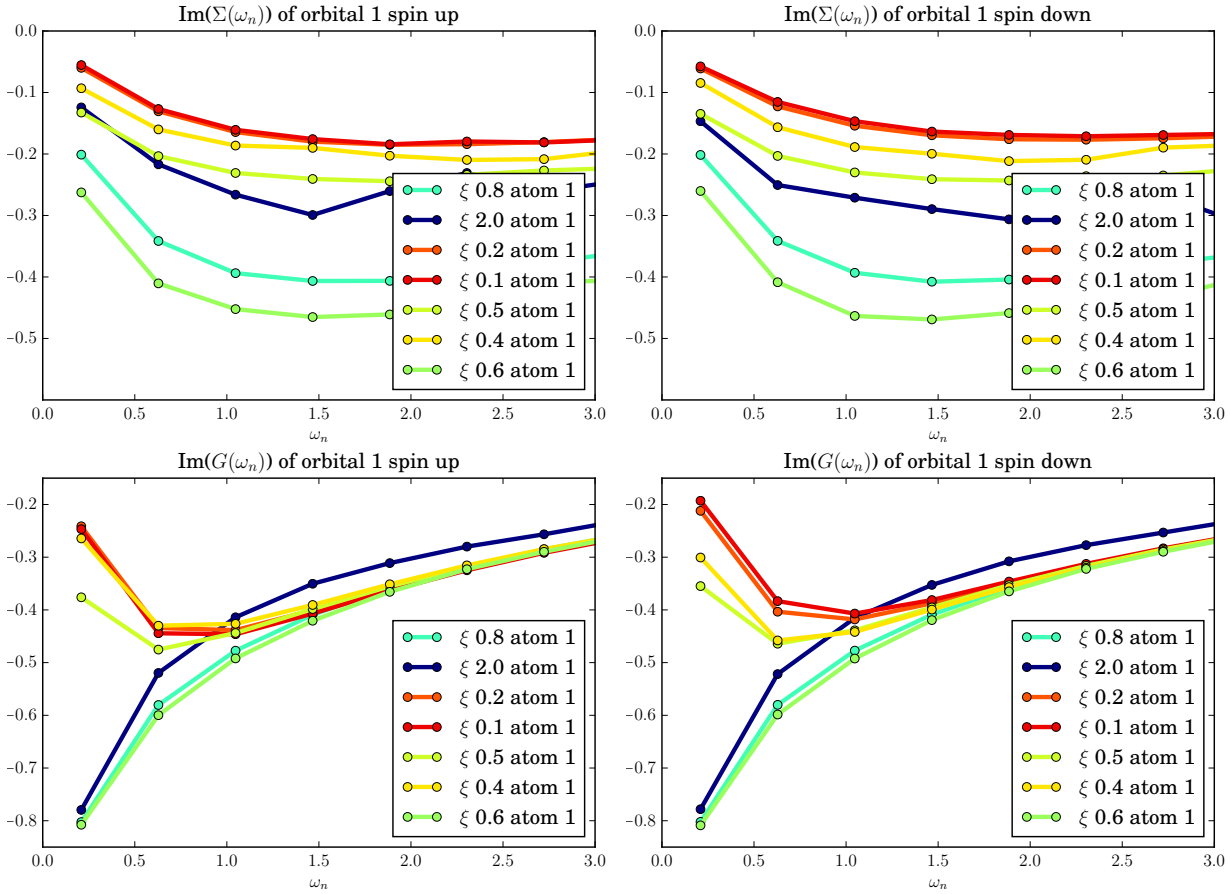

Figure 4.7: Diagonal entries of $\mathrm{Im}[\Sigma_{\gamma\sigma,\bar{\gamma}\bar{\sigma}}]$ (upper panels) and diagonal entries of $\mathrm{Im}[G_{\gamma\sigma,\bar{\gamma}\bar{\sigma}}]$ (lower panels) of orbital 1 (all other orbitals a similar) of atom 1 for various vales of ξ (eV). Neither in the self energy nor in the local Matsubara Green's function the differences of occupation from spin up and down (Figure 4.6) are visible. Although the local self-energy does not display an insulting character the local Matsubara Greens function clearly does for $\xi \leq 500\,\mathrm{meV}$.

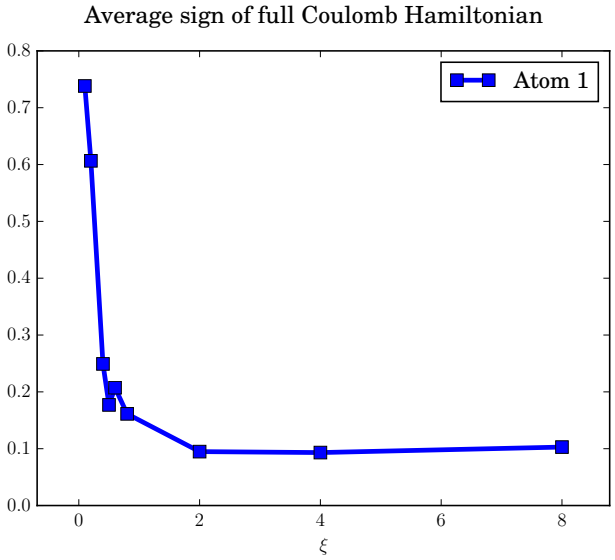

Figure 4.8: ξ (eV) dependence of the average sign of the CT-QMC sampling of atom 1 for $\beta = 15$. The rapid breakdown with ξ significant and even more pronounced than for $\beta = 10$ (Figure 4.5). At $\xi = 2$ it reaches a minimum of about 0.09 and stays almost constant for larger ξ.

4.2.3 $\xi = 0.3\,\mathrm{eV}$

In the following we present the results comparing different temperatures for the estimated spin-orbit coupling strength of $\xi = 300\,\mathrm{meV}$. The results for $\beta = 5$ and 20 has not been part of a previous section and additionally we show the local spectral functions obtained with Maxent.

Figure 4.9 displays the average occupancy for spin up (upper left panel) and down (upper right panel) the diagonal element of the imaginary part of the local self-energy of orbital 1 spin up (lower left panel) and the diagonal element of the imaginary part of the local Matsubara Green's function of orbital 1 spin up (lower right panel). For the local self-energy and the Green's function all other orbital and spin combinations show an equivalent behavior. The occupancies show how $LiOsO_3$ in the LS basis goes from a paramagnetic phase at $\beta = 5$ to an antiferromagnetic phase for $\beta > 5$. However, the strength of the antiferromagnetic phase decreases with increasing β. To better visualize this, let us imagine the point at $\beta = 10$ to be mirrored around a horizontal line at 0.5 [4]. For really high temperatures ($\beta = 5$) ordering is no longer a preferred configuration. At this temperature the local diagonal self-energy shows the features of a bad metal as does the local Matsubara Green's function. For $\beta = 10, 15, 20$ the local self-energy shows all features of a metal, whereas, the local Matsubara Green's function shows features of an insulator. For this temperatures the diagonal elements of the imaginary part of the self-energy do not directly describe the physical behavior. Figure 4.10 shows the local spectral function derived via Maxent. The upper left panel shows the local spectral function of orbital 1 and spin up, the upper right panel shows the local spectral function of orbital 1 and spin down. In the local spectral function

[4] It should not matter whether atom 1 or 2 is dominated by spin up or down. A solution where atom 1 is dominated by spin up and atom 2 is dominated by spin 2 should be equivalent to a solution with the spins exchanged as there is no reason for breaking this symmetry. The solution should take one of the two configurations by chance.

the differences between spin up and down in the antiferromagnetic phase are now well visible as shift of weight from $\omega < 0$ to $\omega > 0$ (or the other way around). The average local spectral function (lower panel) shows the transition from a bad metal at $\beta = 5$ to an insulator with a hap in the local spectral function at $\beta = 15$ ($\beta = 10$ is on the verge to an insulator.). The insulating phase coincides with the antiferromagnetic phase. This is reflected in the real part of the diagonal elements of the local self-energy, where spin up and spin down have have shifted (w.r.t each other) almost constant slopes. However, experimentally $LiOsO_3$ does not have an antiferromagnetic phase and this results have to be taken with care. It is not yet clear why exactly this system tends towards magnetic ordering so strongly and how to enforce paramagnetic ordering in spin-orbit dependent CT-QMC. This study is deferred to later projects.

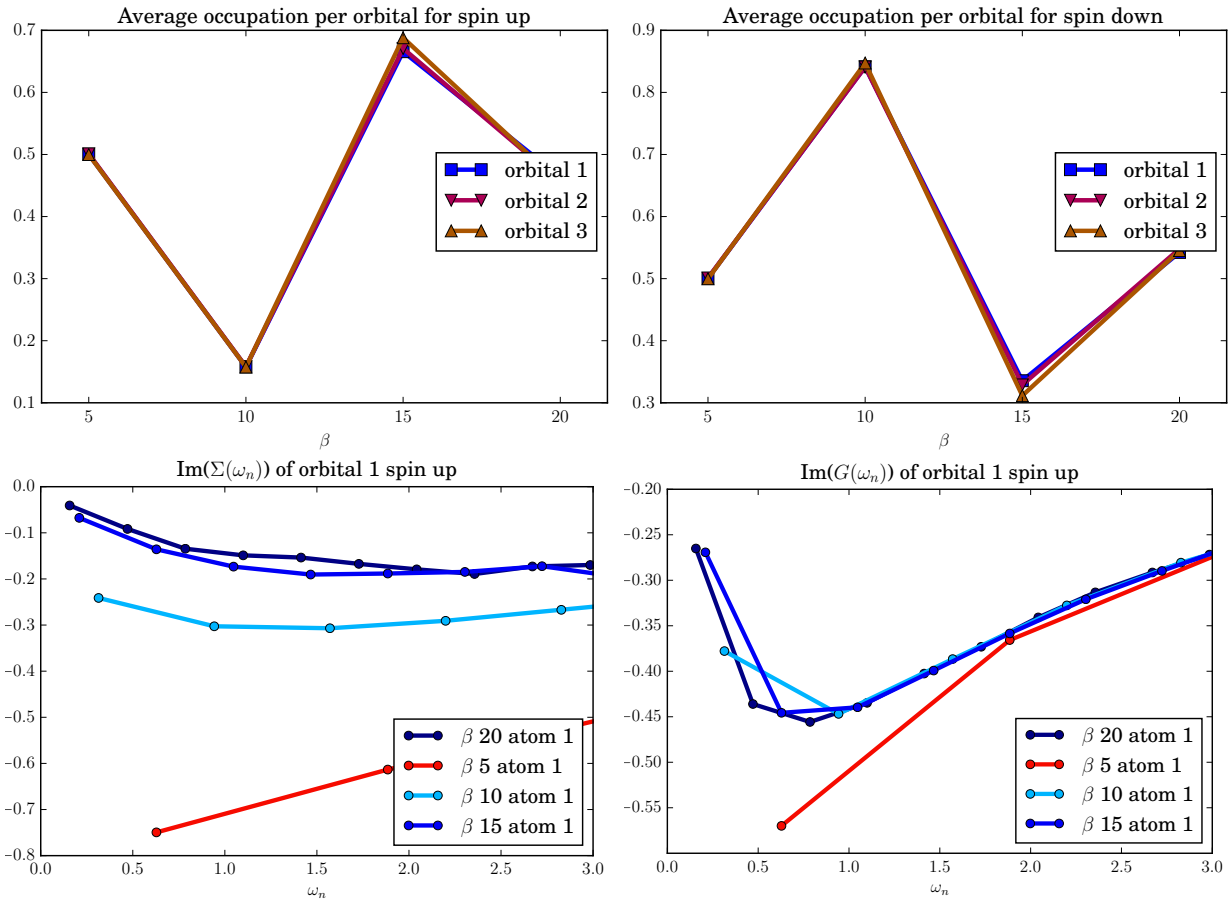

Figure 4.9: β dependence of the occupancy (upper panels), the diagonal entries of $\mathrm{Im}[\Sigma_{\gamma\sigma,\bar{\gamma}\bar{\sigma}}]$ (lower left panel, all orbitals and spins are equal) and diagonal entries of $\mathrm{Im}[G_{\gamma\sigma,\bar{\gamma}\bar{\sigma}}]$ (lower right panel, all orbitals and spins are equal) of atom 1 for $\xi = 300\,\mathrm{meV}$. The hidden last point in the upper left panel is at $\beta = 20$ and 0.45. The occupancies show a antiferromagnetic behavior for $\beta > 5$. However, the tendency decreases with increasing β. The local self-energy shows a bad metal behaviour for $\beta = 5$ and a metallic behavior for $\beta > 5$. The Greens functions show a clear insulating behavior for $\beta > 5$, which is most pronounced for $\beta = 15, 20$.

Eventually, Figure 4.11 shows the β dependence of the average sign of the CT-QMC sampling. As with ξ the sign also decreases with decreasing temperature. A calculation for $\beta = 30$ from scratch (this means that we did not use converged solution of another calculation as starting point) failed i.e. the sign drops to zero and the result are only noise. In order to go to lower temperatures in this basis it is necessary to use converged solutions from higher temperatures as starting point. This approach is regularly used and is known to give good results, though, it takes significantly longer to perform.

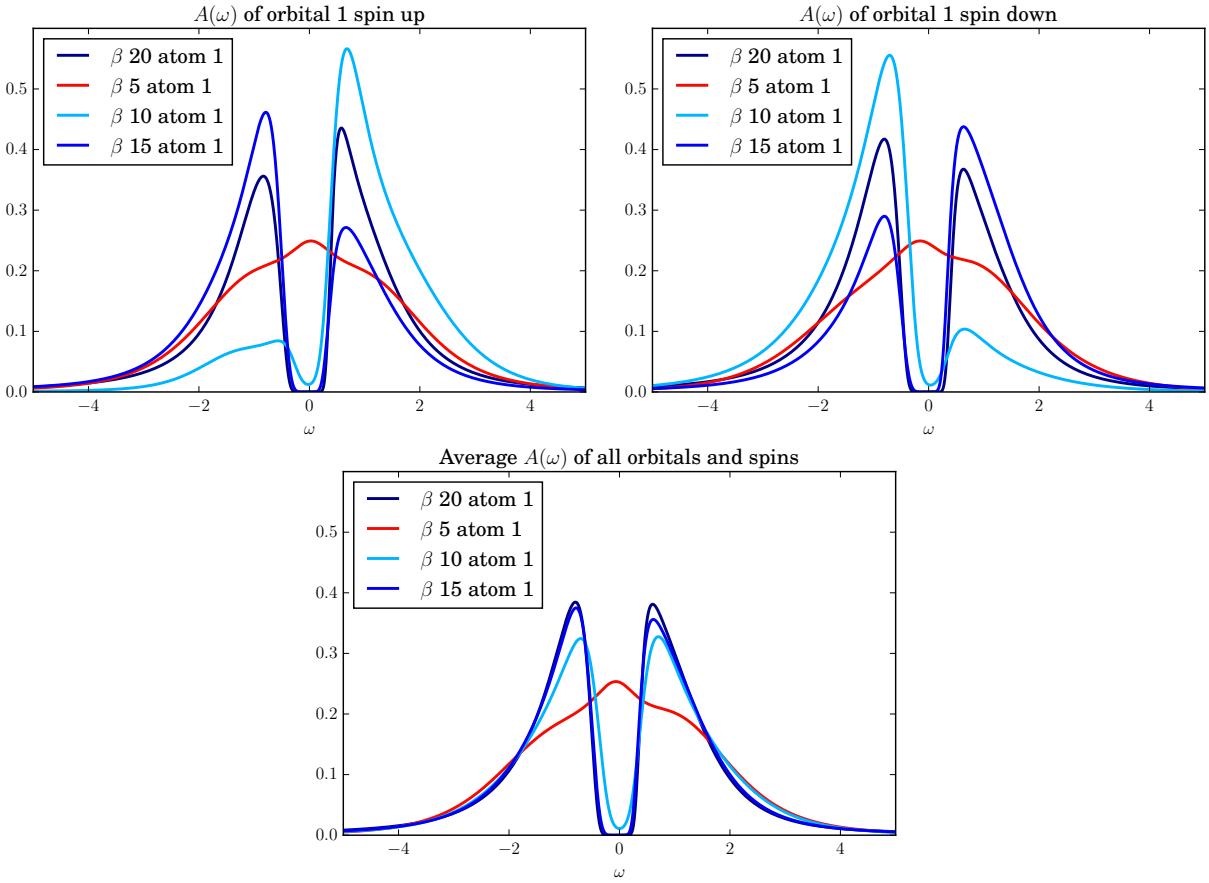

Figure 4.10: Local spectral function for orbital 1 and both spins (upper panels, all orbitals are similar) and averaged (band and spin) local spectral function (lower panel) of atom 1 for $\xi = 300\,\text{meV}$. $\beta = 5$ shows a bad metal behavior, with an almost vanished quasi-particle peak at $\omega = 5$. The differences in the occupancies (Figure 4.9) for $\beta = 10, 15, 20$ where, $\beta = 10$ is on the verge to an insulator and $\beta = 15, 20$ are insulating.

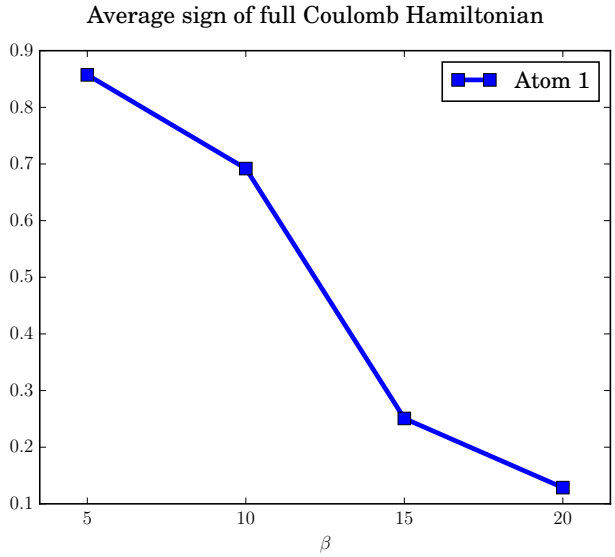

Figure 4.11: β dependence of the average sign of the CT-QMC sampling of atom 1 for $\xi = 300\,\text{meV}$. With increasing β the average sign quickly decreases to 0.12 at $\beta = 20$. This could become a serious problem for larger β as a decreasing sign quickly leads to failed calculations.

4.2.4 $\xi = 0.6\,\text{eV}$

In this section we compare the results of calculations for $\beta = 5, 10, 15, 20$ with a spin-orbit coupling strength of 600 meV [5]. The only calculation which is not part of any previous section is $\beta = 20$. For this spin-orbit coupling strength all calculations display a paramagnetic phase as displayed in the upper panels of Figure 4.12, which is consistent with experiments. For $\beta = 20$ there is a residual tendency towards an antiferromagnetic phase, even though, it does not appear in the spectra (compare Figure 4.13). Both the imaginary part of the diagonal elements of the local self-energy (Figure 4.12 lower left panel) and the imaginary part of the diagonal elements of the local Matsubara Green's function (Figure 4.12 lower left panel) of atom 1 show a metallic behavior. There is only orbital 1 spin up displayed because all other combinations are equivalent. The metallic coherence decreases with decreasing β, which is in agreement with the calculations without spin-orbit coupling as presented in section 3.3. This trend is also visible in the corresponding local spectral functions which are displayed in Figure 4.13. Both spin channels (upper panels) and also the averaged local spectral function (lower panel) display the same characteristics and with a well prounounced quasi-particle peak around $\omega = 0$ (it is actually slightly shifted towards $\omega < 0$). As in the case without spin-orbit coupling the quasi-particle peak decreases with increasing temperature, i.e. decreasing β. In difference to the calculations without spin-orbit coupling the breakdown of the quasi-particle peak is not visible and only at $\beta = 5$ (2320K) the coherent peak is significantly suppressed. Furthermore, there is second very flat peak for $\omega > 0$, which only very slightly temperature dependent.

[5] This coupling strength is only displayed for this basis, because it gives a paramagnetic solution. In general a study at this coupling strength would be interesting also in the locally diagonal basis. This is postponed to later projects.

Eventually, Figure 4.14 shows the β dependence of the average sign of the CT-QMC sampling. As for $\xi = 300\,\text{meV}$ the average sign quickly drops with increasing β. Higher values of β than 20 can only be calculated using converged solutions from lower β, i.e. cooling down the system step by step instead of directly performing the calculation from scratch.

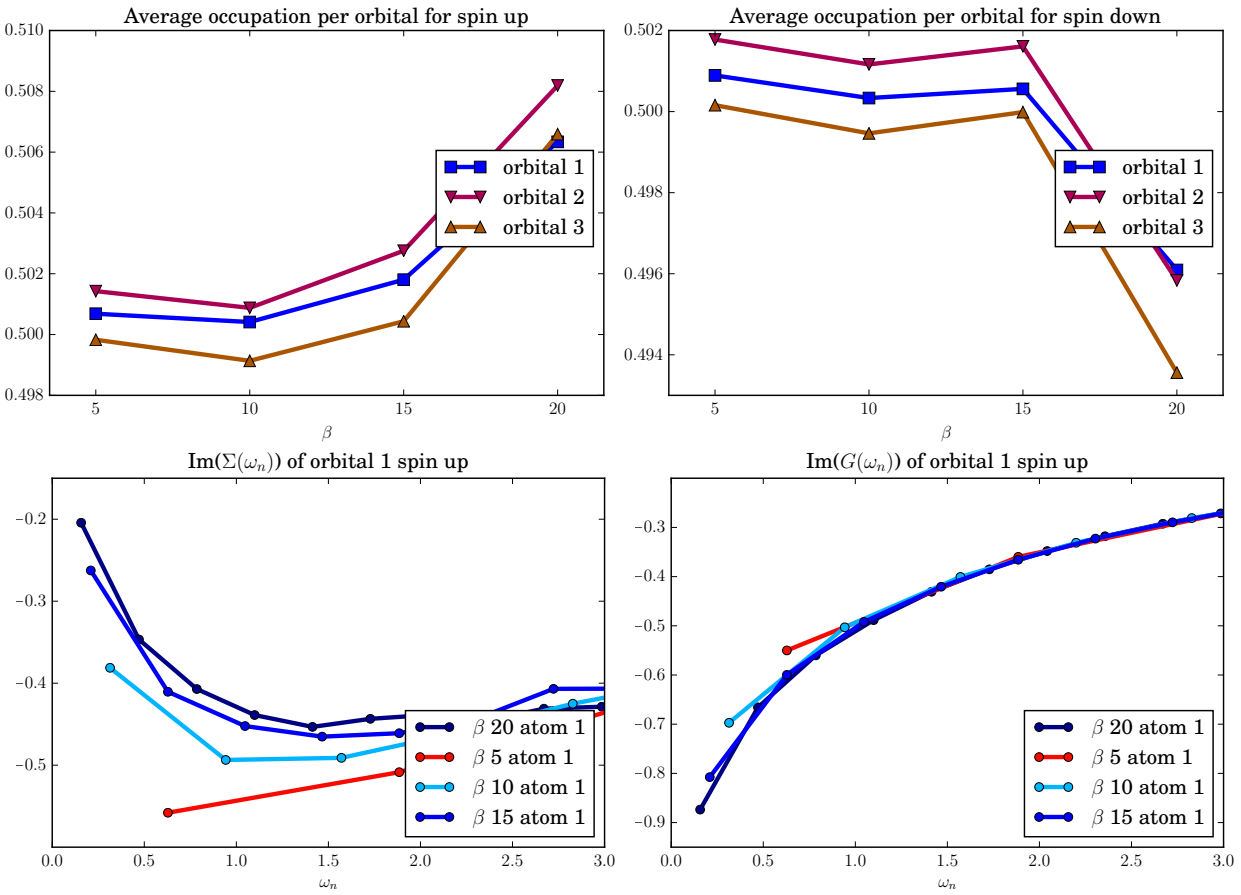

Figure 4.12: β dependence of the occupancy (upper panels), the diagonal entries of $\text{Im}[\Sigma_{\gamma\sigma,\bar{\gamma}\bar{\sigma}}]$ (lower left panel, all orbitals and spins are equal) and diagonal entries of $\text{Im}[G_{\gamma\sigma,\bar{\gamma}\bar{\sigma}}]$ (lower right panel, all orbitals and spins are equal) of atom 1 for $\xi = 600\,\text{meV}$. The occupancies show a very small antiferromagnetic tendency only for $\beta = 20$. The local self-energy shows a bad metal behaviour for $\beta = 5$ and a metallic behavior for $\beta > 5$. This is also reflected in the local Matsubara Greens functions, which show a clear metallic behavior for $\beta > 5$.

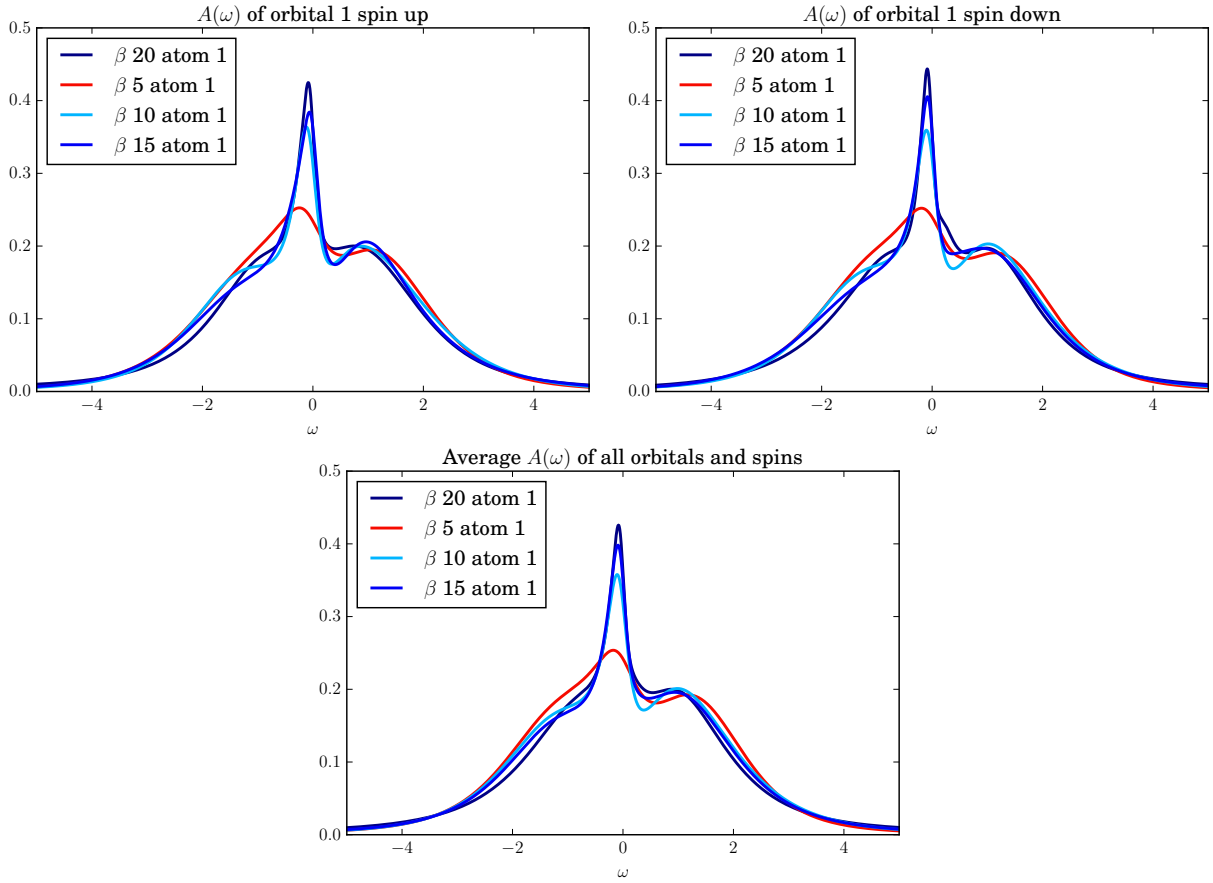

Figure 4.13: Local spectral function for orbital 1 and both spins (upper panels, all orbitals are similar) and averaged (band and spin) local spectral function (lower panel) of atom 1 for $\xi = 600\,\text{meV}$. All temperatures show a metallic behavior, although the quasi-particle peak decreases with decreasing β. The spin-orbit coupling leads to a pronounced side peak around $\omega \approx 1$.

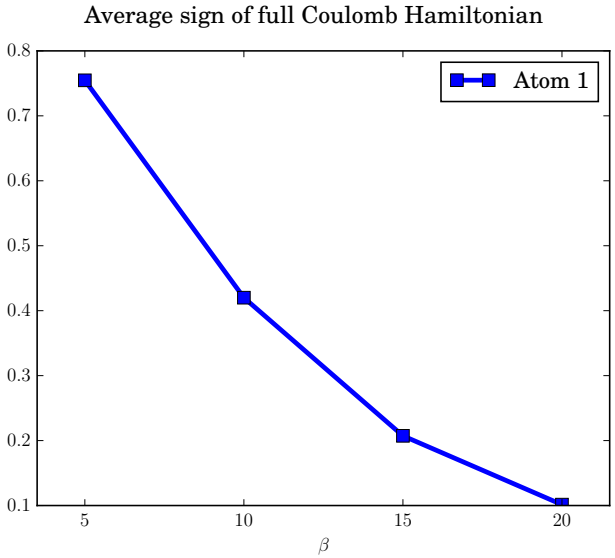

Figure 4.14: β dependence of the average sign of the CT-QMC sampling of atom 1 for $\xi = 600\,\text{meV}$. With increasing β the average sign quickly decreases to 0.1 at $\beta = 20$. This could become a serious problem for larger β as a decreasing sign quickly leads to failed calculations.

4.3 Locally Diagonal Basis Extended with Spin-Orbit Coupling

In this section we present the results calculated in the locally diagonal basis with local (atomic) spin-orbit coupling. This means that the Wannier Hamiltonian and the interaction coefficient matrix are rotated into the locally diagonal basis (using the script from Appendix E and F). Then the local spin-orbit coupling term (1.3) is added to the Wannier Hamiltonian at every k point using the script from Appendix H. In this basis the off-diagonal terms from the local one-particle Hamiltonian in the standard basis are incorporated in the diagonal elements, i.e. the t_{2g} are no longer degenerate and have a splitting of about 250 meV between the lower 2 and the higher orbital. An example Parameters.in file is presented in the second part of Appendix C (The "complex_umatrix = 1" line has to be omitted). All calculations have been performed on 480-800 cores on VSC3. Analytical continuations have been performed with Maxent [18] also on VSC3.

As in the standard basis calculations with $\beta > 5$ show an antiferromagnetic phase for low spin-orbit coupling strengths ($\xi < 400\,\text{meV}$).

Most of the figures show only the results of atom 1, because the other atoms are similar. If this is not the case, more atoms are displayed. The same holds for the displayed orbitals.

4.3.1 $\beta = 10$

In this subsection we present the results for $\beta = 10$, i.e. 1160 K, for various values of the spin-orbit coupling strength. At this temperature $LiOsO_3$ shows a paramagnetic phase for $\xi < 400\,\text{meV}$. This is shown in Figure 4.15. The left side displays the occupancies of atom 1, the right side the occupancies of atom 2. For $\xi = 200\,\text{meV}$ the calculations shows only a very small magnetization, however, we will see that the local Matsubara Green's function fits into the general trend. The

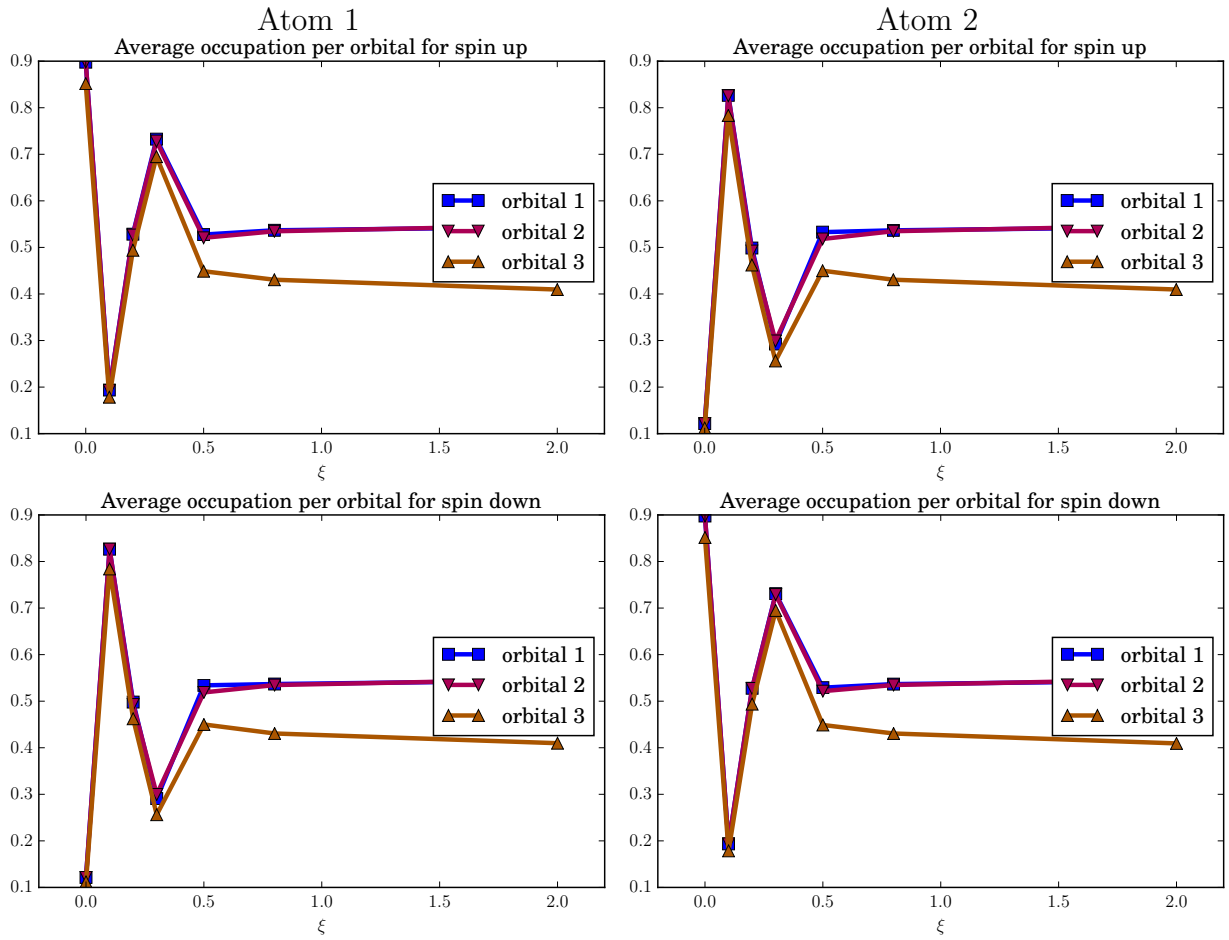

Figure 4.15: ξ (eV) dependence of the occupancies of the orbitals and spins at $\beta = 10$ for atom 1 (left panels) and atom 2 (right panels) in the Hloc basis. For $\xi < 400\,\text{meV}$ LiOsO3 shows antiferromagnetic behavior, which vanishes at 400 meV. For larger values of ξ there is an slightly increasing gap between orbitals 1 and 2 and orbital 3. It appears that spin-orbit coupling strongly decreases the antiferromagnetic tendency of LiOsO3 in the Hloc basis.

other two calculations for $\xi < 400\,\text{meV}$ show a strong antiferromagnetic ordering. Calculations with $\xi \geq 400\,\text{meV}$ show a paramagnetic ordering i.e. there is no significant difference between spin up and down and atom 1 and 2. There is, however, a difference between orbitals 1 and 2 and orbital 3, which is less occupied. This is, as for $\beta = 5$, in agreement to the lifting of the t_{2g} degeneracy in this basis, as well as the slight increase of the gap between orbital 1 and 2 and orbital 3 with increasing ξ.

The antiferromagnetic phase is, as for all previous calculations, not seen in the imaginary part of the diagonal elements of the local self-energy displayed in the upper panels of Figure 4.16. Both spins are, as in the standard basis, equivalent. In difference to the calculations at $\beta = 5$ the self energy does show a more metallic slope, especially for $\xi = 2\,\text{eV}$. There is also a well visible difference in the slopes of orbital 3 for $\xi = 0.8$ and 2 eV. This difference is also inherited to the imaginary part of the diagonal terms of the local Matsubara Green's function of atom 1, which is displayed in the lower panels of Figure 4.16. However, the trend towards metal or insulator is equal for all orbital. Calculations with $\xi \leq 400\,\text{meV}$ show insulating characteristics, whereas they

show metallic characteristic for $\xi \geq 500\,\text{meV}$. This is similar as in the standard basis, where this situation is just shifted up by 100 meV. The average sign of the CT-QMC sampling is displayed in Figure 4.17. It shows a significant decrease with increasing ξ, quickly dropping to 0.54 in the range 0 to 2 eV. Compared to the standard basis the locally diagonal basis performs better, w.r.t. the average sign, than the standard basis (compare Figure 4.5).

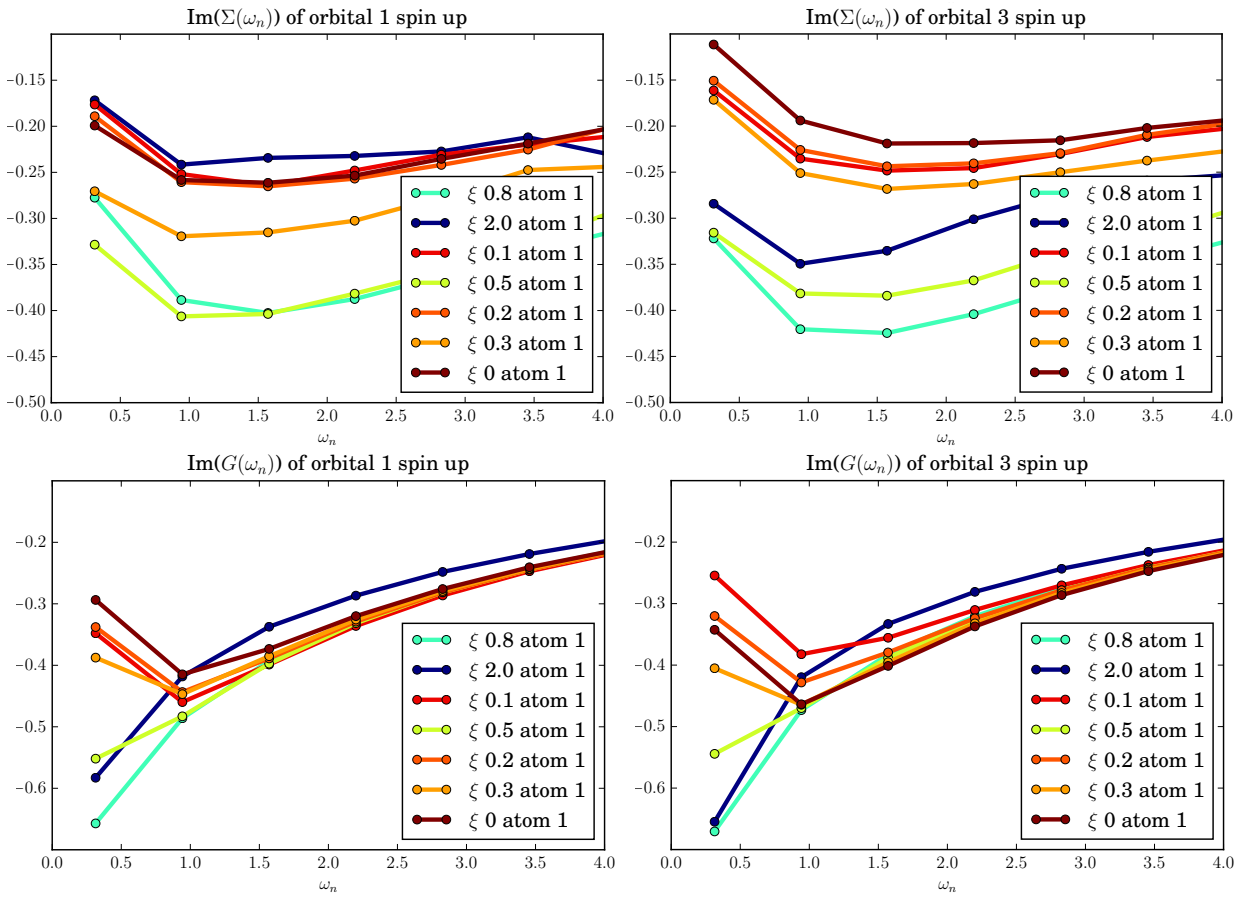

Figure 4.16: Diagonal entries of $\text{Im}[\Sigma_{\gamma\sigma,\bar{\gamma}\bar{\sigma}}]$ (upper panels) and diagonal entries of $\text{Im}[G_{\gamma\sigma,\bar{\gamma}\bar{\sigma}}]$ (lower panels) of orbital 1 and 3 (band 2 is equivalent to orbital 1) of atom 1 for various vales of ξ (eV). Neither in the local self-energy nor in the local Matsubara Green's function the differences of occupation from spin up and down (Figure 4.15) appear to have a great effect (spin down shows equivalent behavior and is not displayed). However, although the local self-energy does not display an insulting character the local Matsubara Greens function does for $\xi \leq 400\,\text{meV}$.

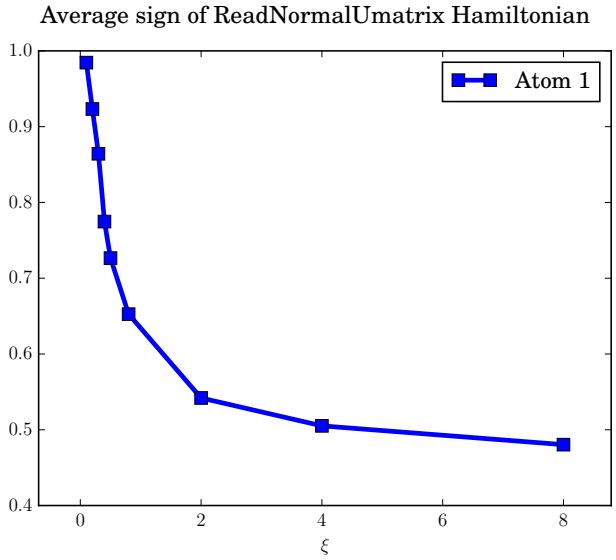

Figure 4.17: ξ (eV) dependence of the average sign of the CT-QMC sampling of atom 1 for $\beta = 10$. It rapidly decreases for $0\,\text{eV} < \xi < 2\,\text{eV}$ falling to 0.54 at 2 eV.

4.3.2 $\xi = 0.3\,\text{eV}$

In this subsection we compare the results for a spin-orbit coupling strength of 300 meV for $\beta = 5$ to 20. The results of $\beta = 5$, 10 and 20 have not been presented in the previous sections. The upper panels of Figure 4.18 display the average occupancies of atom 1 for spin up (left panel) and spin down (right panel). The calculation of $\beta = 10$ shows a very pronounced antiferromagnetic phase. Calculations for $\beta = 15$ and 20 do not display such strong antiferromagnetic ordering. It is, however strong enough to yield an "insulating-like" imaginary part of the diagonal elements of the local Matsubara Green's function (lower left panel). Note that although orbital 3 has a slightly different slope it is not explicitly displayed here, because there is no qualitatively new information contained in it. As it is the case in the standard basis the imaginary part of the diagonal terms of the local self-energy does not reflect the insulating character of the local Matsubara Green's function. For the paramagnetic phase at $\beta = 5$ both the local self-energy and the local Matsubara Green's function show bad metal characteristics. This is directly inherited to the local spectral function displayed in Figure 4.19 which shows an almost vanished quasi-particle peak at $\beta = 5$. For lower temperatures, i.e. higher β, the local spectral function shows a metal-insulator transition which is probably induced by the antiferromagnetic ordering ("Slater-like" MIT). As in the standard basis $\beta = 10$ is on the verge to such a MIT. The local spectral function shows the differences from the spin up and down channel. The spin up channel has weight shifted towards $\omega < 0$, the spin down channel towards $\omega > 0$.

The average sign of the CT-QMC sampling is displayed in Figure 4.20. It almost linearly decreases from 0.97 at $\beta = 5$ to 0.66 at $\beta = 20$. This is almost a factor of 6 better compared to the standard basis where the sign reduced to 0.12 at $\beta = 20$. The locally diagonal basis therefore offers the opportunity to reach much lower temperatures. This is, however, postponed to later projects.

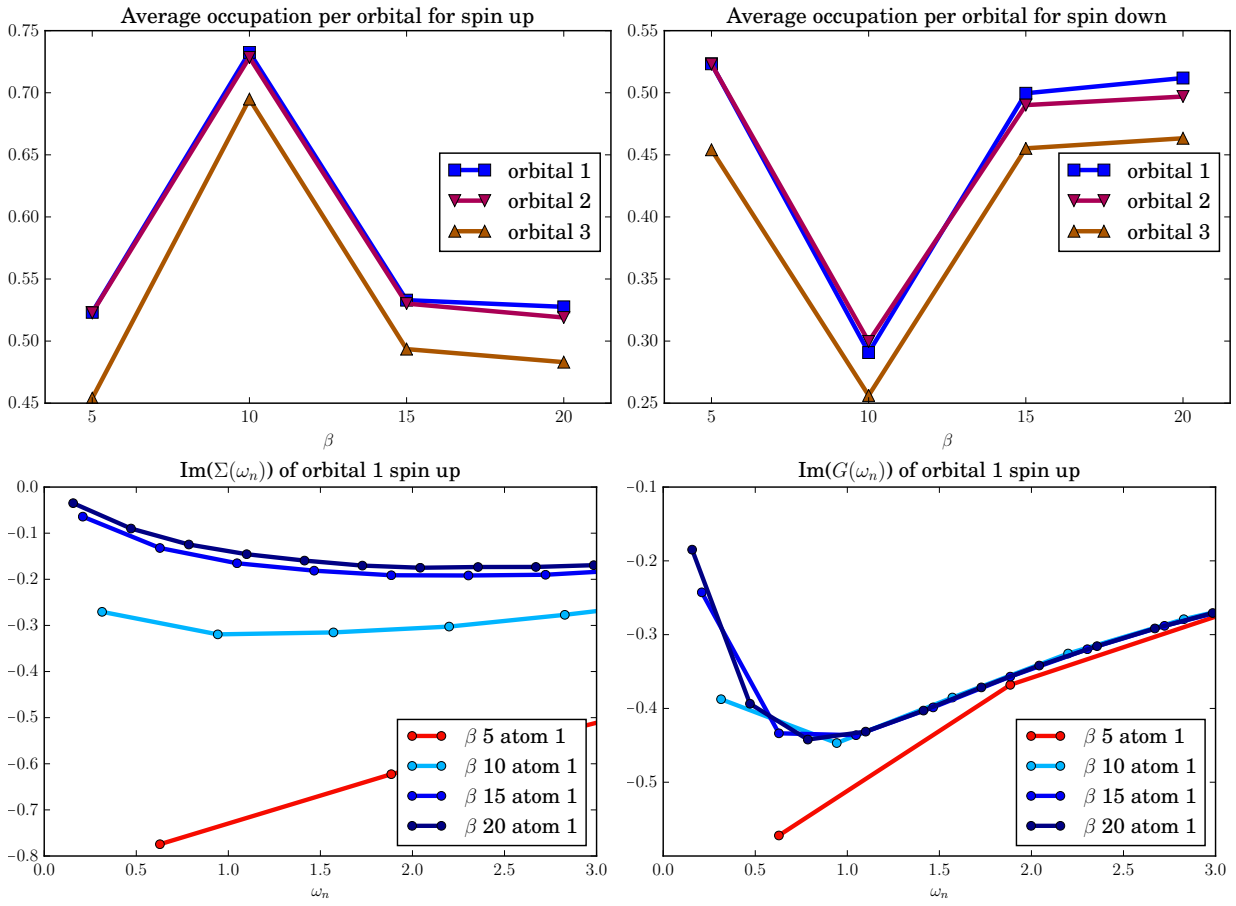

Figure 4.18: β dependence of the occupancy (upper panels), the diagonal entries of $\mathrm{Im}[\Sigma_{\gamma\sigma,\bar{\gamma}\bar{\sigma}}]$ (lower left panel, all orbitals and spins are equal) and diagonal entries of $\mathrm{Im}[G_{\gamma\sigma,\bar{\gamma}\bar{\sigma}}]$ (lower right panel, all orbitals and spins are equal) of atom 1 for $\xi = 300\,\mathrm{meV}$. The occupancies show a obvious antiferromagnetic behavior only for $\beta = 10$. For $\beta = 15, 20$ the tendency is graphically hardly visible. The local self-energy shows a bad metal behaviour for $\beta = 5$ and a metallic behavior for $\beta > 5$. However, the Greens functions show a clear insulating behavior for $\beta > 5$, which is most pronounced for $\beta = 15, 20$. It appears that a very weak antiferromagnetic phase suffices for a metall-insultor transition.

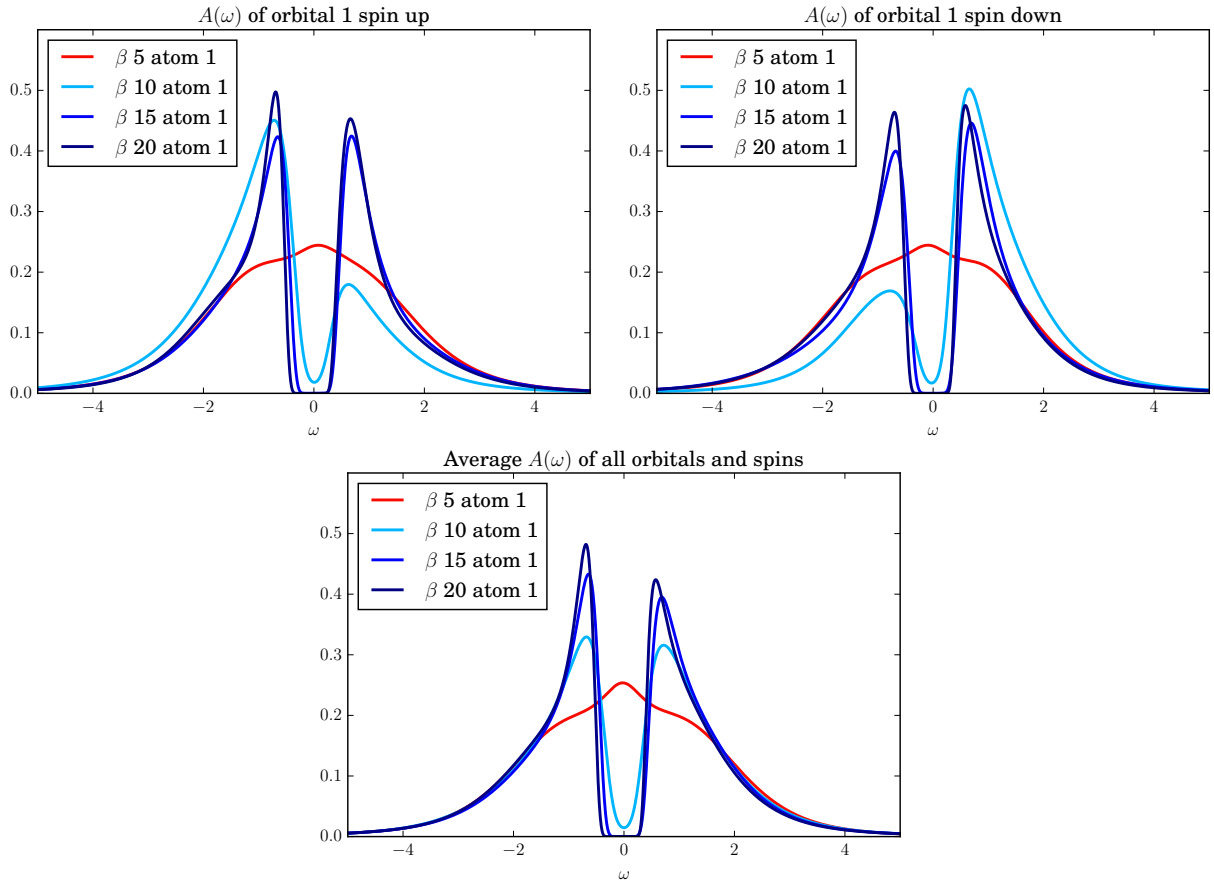

Figure 4.19: Local spectral function for orbital 1 and both spins (upper panels, all orbitals are similar) and averaged (band and spin) local spectral function (lower panel) of atom 1 for $\xi = 300\,\mathrm{meV}$. $\beta = 5$ shows a bad metal behavior, with an almost vanished quasi-particle peak at $\omega = 5$. The differences in the occupancies (Figure 4.18) for $\beta = 10, 15, 20$ where, $\beta = 10$ is on the verge to an insulator and $\beta = 15, 20$ are insulating. This trend is very similar to the LS basis Figure 4.10.

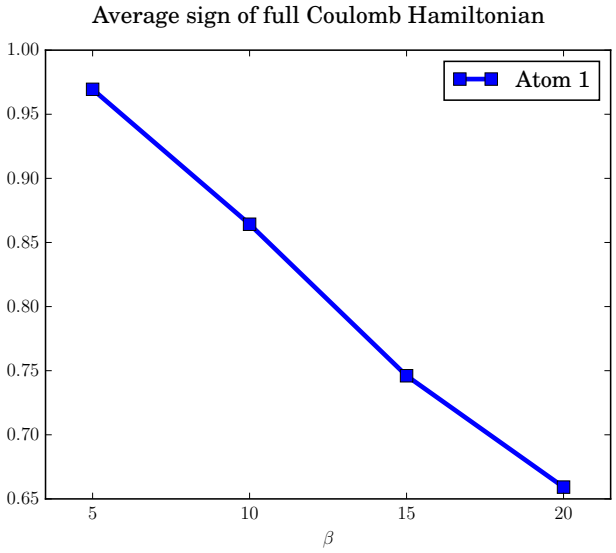

Figure 4.20: β dependence of the average sign of the CT-QMC sampling of atom 1 for $\xi = 300\,\text{meV}$. With increasing β the average sign almost linearly decreases to 0.66 at $\beta = 20$.

4.4 Standard Basis Extended with Spin-Orbit Coupling Diagonalized

In this section we present the results calculated in the fully diagonalized standard basis. This means that the local spin-orbit coupling is added to every k point of the Wannier Hamiltonian using the script from Appendix H. Then the local one-particle Hamiltonian is diagonalized and the Wannier Hamiltonian and the local interaction coefficient matrix are rotated into this diagonal basis (scripts from Appendix E and F). Therefore the local one-particle coefficient matrix is diagonal again. This increases the energetic splitting of t_{2g} orbitals (see Figure 4.1). What will be referred to as "spin" index is not a physical spin anymore since the diagonalization of the local one-particle coefficient matrix mixes both spin channels.

Most of the figures show only the results of atom 1, because the other atoms are similar. If this is not the case, more atoms are displayed. The same holds for the displayed orbitals.

4.4.1 $\beta = 10$

In this subsection we present the results for $\beta = 10$ and various values if ξ. The previously observed tendency towards magnetic ordering is only observed for very low values of ξ e.g. 20 meV. This can be seen from Figure 4.21, where the upper panels show the average occupancies of atom 1 for spin index up (left panel) and spin index down (right panel) (For atom 2 the situation is spin reversed). Quite remarkably, in this basis, only for $\xi = 0$ and 20 meV magnetic ordering is observed. For all other values the results show a paramagnetic phase. The gap between the energetic lower lying orbitals 1 and 2 and the higher lying orbital 3 rapidly increases. For $\xi = 2\,\text{eV}$ third orbital is almost unoccupied and all charge carriers are either in orbital 1 or 2. This is due to the large increase in the energetic gap which is about 3 eV at $\xi = 2\,\text{eV}$ (compare Figure 4.1).

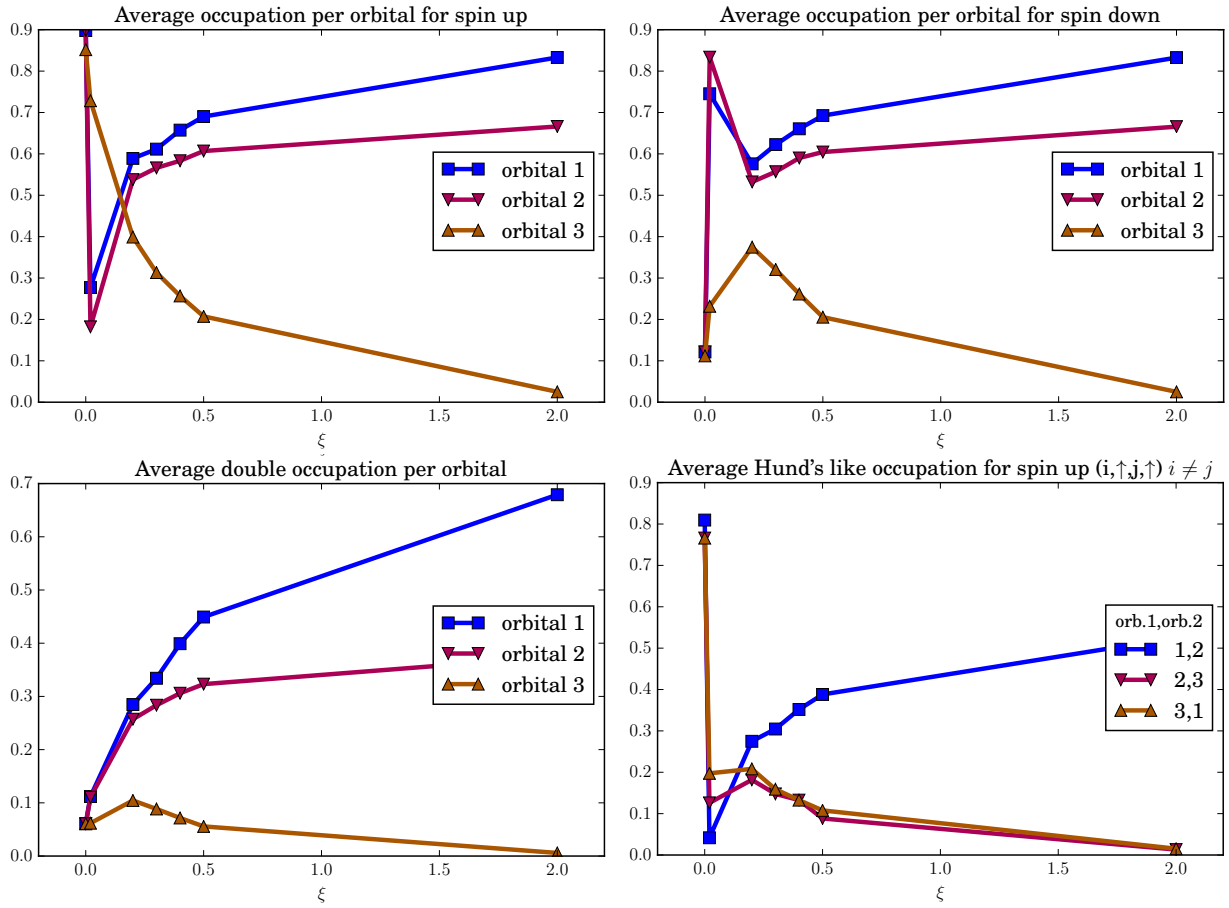

Figure 4.21: ξ (eV) dependence of the occupancies of atom 1 for $\beta = 10$. The non-visible point in the average double occupancy of orbital 2 is at 0.37. For $\xi = 20$ meV also this basis shows an antiferromagnetic phase, however, for $\xi > 200$ meV both spin channels display the same behavior. The double occupancy increases with increasing ξ for orbitals 1 and 2 and decreases for orbital 3. In contrast the Hund's like occupancy decreases for orbital combination 1/3 and 2/3 and increases for orbitals combination 1/2.

However the small gap of about 150 meV between orbital 1 and 2 also induces an enhancement of the occupation of orbital 1 of about 25% compared to orbital 2. This is also reflected in the average double occupancies where the increase for orbital 1 compared to orbital 2 is of about 85%. This follows from the average occupancy of 0.83 for each "spin" channel, which needs a high double occupancy. However, the occupancy of orbital 2 is only 0.66, which, apparantly can be obtained with a much smaller double occupation of this orbital. In difference to all previous calculation the Hund's like occupation of orbital 1,3 and 2,3 decreases, which is of course induced by the fact that orbital 3 is almost unoccupied. For orbitals 1,2 the Hund's like occupation quickly increases with increasing ξ.

In Figure 4.22 shows the imaginary part of the diagonal terms of the local self-energy (left side) and the imaginary part of the diagonal elements of the local Matsubara Green's function of atom 1. The local self-energy displays only small differences between the orbital. For $\xi = 200$ and 300 meV the slope close to $\omega_n = 0$ is is steepest, followed by orbital 2 and 3. The small

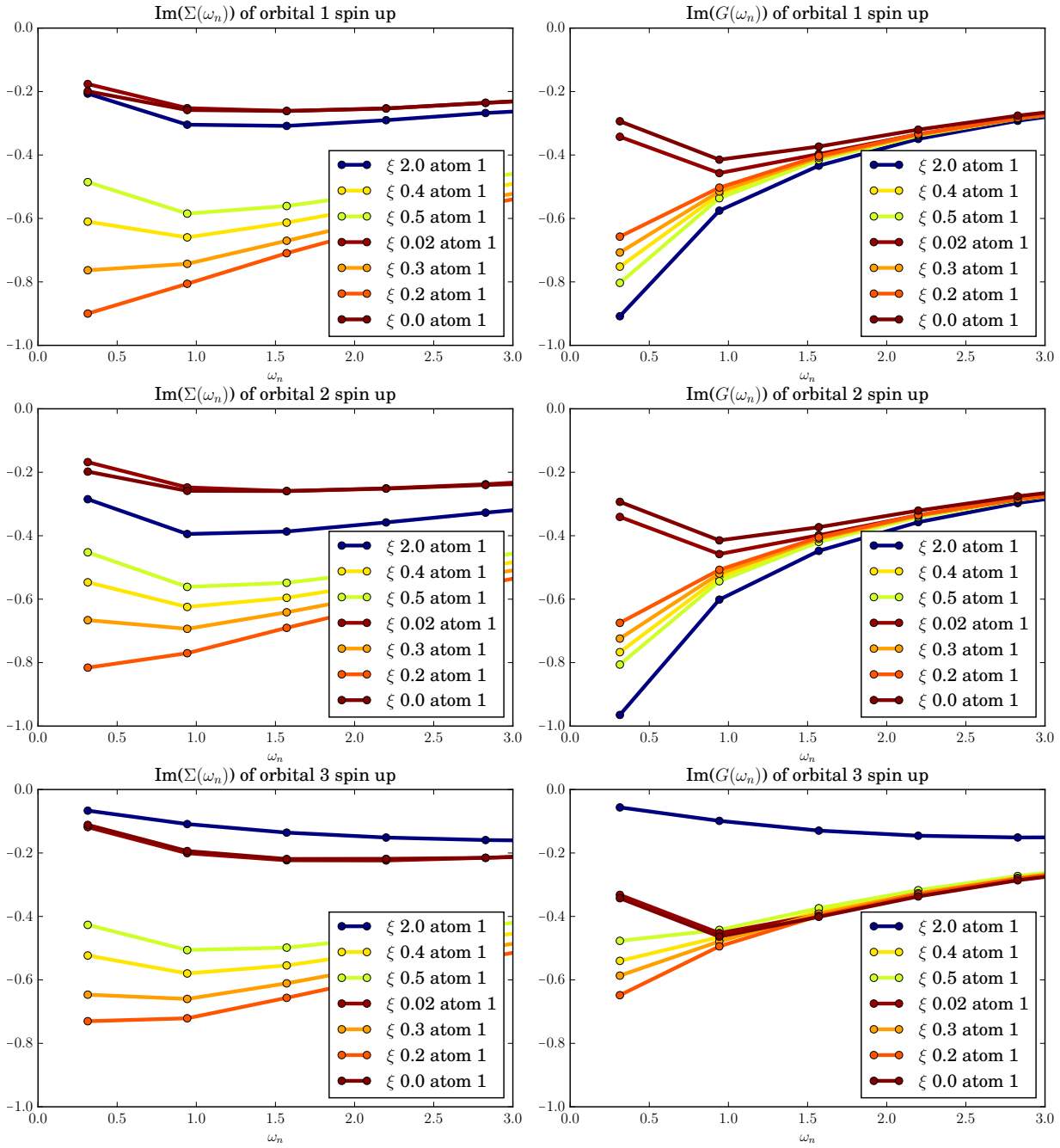

Figure 4.22: Diagonal entries of $\mathrm{Im}[\Sigma_{\gamma\sigma,\bar{\gamma}\bar{\sigma}}]$ (left panels) and diagonal entries of $\mathrm{Im}[G_{\gamma\sigma,\bar{\gamma}\bar{\sigma}}]$ (right panels) (spin up and down are equivalent) of atom 1 for various vales of ξ (eV). The local self-energy shows a bad metal to metal character for increasing ξ from 0.2 eV to 2 eV. The local Matsubara Green's function displays opposite trends for orbital 1 and 2 and orbital 3. Orbital 1 and 2 move towards a metal characteristic for larger ξ, whereas the opposite is the case for orbital 3. In the antiferromagnetic phase all orbitals display an insulating characteristic.

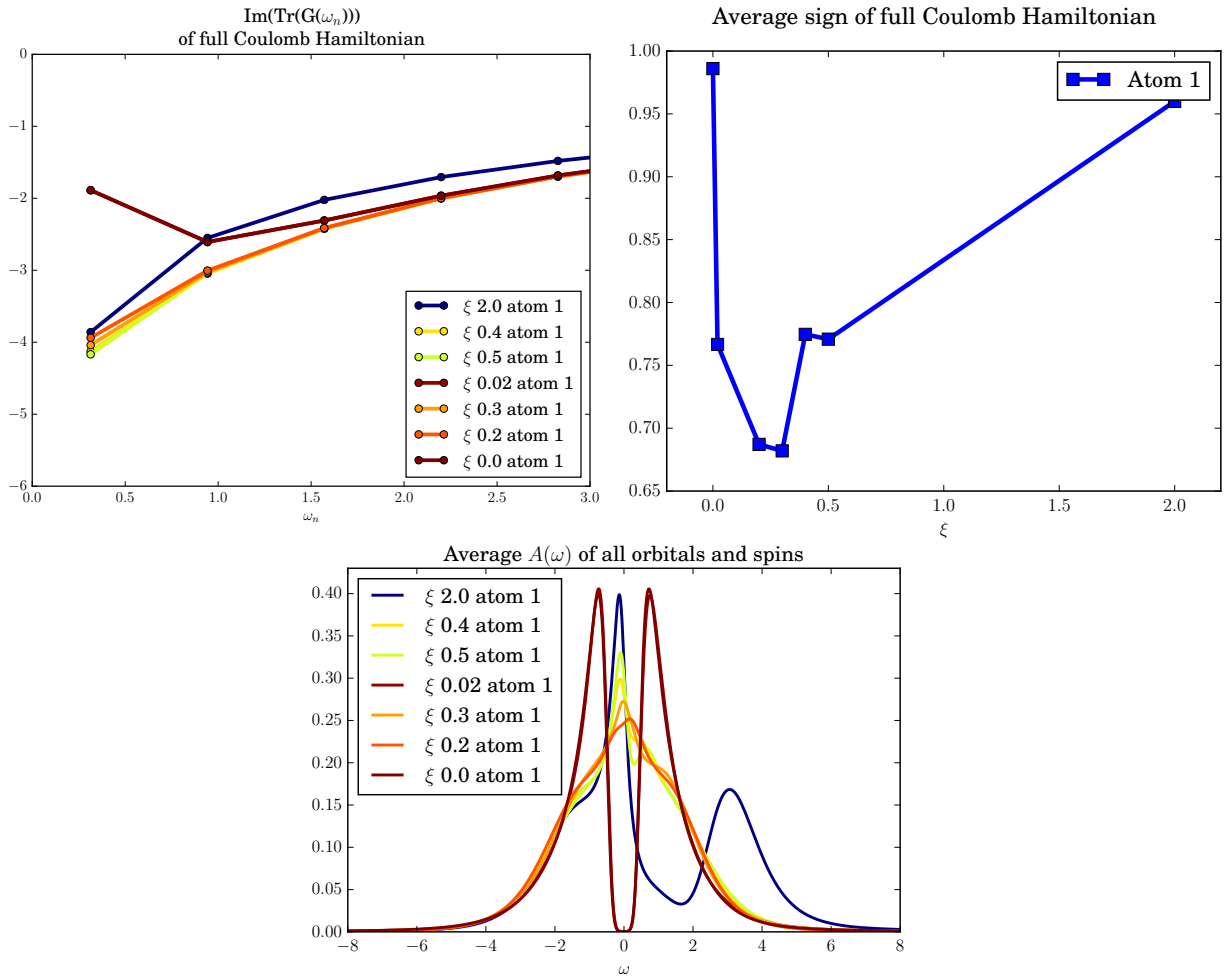

Figure 4.23: ξ (eV) dependence of the trace over all orbitals and spins of the local Matsubara Greens function (upper left panel), the average local spectral function (lower panel) and the average sign of the CT-QMC sampling (upper right) of atom 1 for $\beta = 10$. The trace of the local Matsubara Green's function both reflect the insulating behavior induced by the antiferromagnetic phase at very small ξ, a slight tendency towards metallicity in the intermediate regime $0.2\,\text{eV} < \xi < 0.5\,\text{eV}$ and a slight tendency towards a more insulating behavior for large $\xi = 2\,\text{eV}$. The average sign shows a minimum about 0.67 for $0.2\,\text{eV} \leq \xi \geq 0.3\,\text{eV}$ and increases again for larger ξ. This basis appears to have a significant sign problem only for a specific range of ξ.

differences are also visible in the local Matsubara Green's function. For $\xi = 20\,\text{meV}$ it displays insulating characteristics, consistent with previous antiferromagnetic results. For all other ξ orbital 1 and 2 display a metallic characteristic with a trend towards a better metal. This trend is reversed for orbital 3 which loses its metallic features with increasing ξ. This is inherited from its occupancy.

Eventually Figure 4.23 displays the trace of the imaginary part of the local Matsubara Green's function (upper left panel) the average sign of the CT-QMC sampling (upper right panel) and the average local spectral function (lower panel) of atom 1. The trace of the local Matsubara Green's function shows a slight trend towards a more metallic solution for $0\,\text{meV} < \xi < 500\,\text{meV}$. However, for $\xi = 2\,\text{eV}$ it shows a less metallic slope. This behavior is also reflected in the average

local spectral function. The decrease of the Matsubara Green's function at the first Matsubara frequency for $\xi = 2\,\mathrm{eV}$ induces a slight shift of the quasi-particle shift towards smaller ω in the local spectral function. Furthermore, the average local spectral functions shows a second peak around $\omega = 3$, which is separated from the quasi-particle peak by the onset of a gap.

The average CT-QMC sign decreases rapidly from $\xi = 0$ to 200 meV. It also displays a local minimum of 0.68 between 200 and 300 meV. In difference to the non-diagonalized calculation from the previous chapters, in this basis the average sign increases for $\xi > 0.5\,\mathrm{eV}$. The position of the minimum is unfortunate as it is exactly at our estimation of the local spin-orbit coupling strength. However, this basis appears to be a good choice if spin-orbit coupling is assumed to be one of the dominant interactions.

4.4.2 $\xi = 0.3\,\mathrm{eV}$

In this subsection we compare the results for $\xi = 300\,\mathrm{meV}$, which is the estimated strength of the local-spin orbit coupling in $LiOsO_3$, for $\beta = 10 - 30$. As in the last sections, we first present the occupancies of atom 1 in Figure 4.24. The average occupancy per orbital is displayed in the lower panel. A minor temperature trend is observed for orbital 1, which occupancy slightly increases with increasing β, and orbital 3, which becomes emptier with increasing β. The double occupancy shows a more pronounced trend for orbital 1, where the double occupancy increases with increasing β. This indicates a metallizing trend for this orbital. The trends in the Hund's like occupancy are again only weakly pronounced and show a slight increase for orbitals 1/2 and a slight decrease for orbitals 1/3 and 2/3. In order to obtain a deeper insight Figure 4.25 shows the imaginary part of the diagonal terms of the local Matsubara Green's function of atom 1. Orbitals 1 and 2 display a trend towards a good metal behavior for increasing β, whereas, as expected from the average double occupancy, this trend is more pronounced for orbital 1. In difference orbital 3 displays almost no β dependence is has bad metal characteristic on the whole β range presented. Since the occupancy of orbital 1 is highest and the metallic coherence is also most visible in this orbital, this is a strong indication that $LiOsO_3$, also with the inclusion of local spin-orbit coupling, gradually loses its metallic properties with increasing temperature. This is also reflected in the trace of local Matsubara Green's function (lower right panel) which shows a clear decrease of its metallic character with increasing temperature.

The corresponding local spectral functions, are displayed in Figure 4.26. Orbital 1 (upper left panel) shows the strongest temperature dependence, with a quickly decreasing quasi-particle peak for increasing β, which is in agreement to the Matsubara Green's function. Orbital 2 also shows this temperature dependence it is however less pronounced. Orbital 3 displays a broad peak between $\omega = 0$ and 3, which also decreases with decreasing β. The onset of this broad peak is also visible in orbitals 1 and 2, especially for $\beta = 30$. The average local spectral function (lower right panel) shows a quasi-particle peak, which loses its metallic coherence with decreasing β. The broad peak of orbital 3 is only visible as a broadening of the average spectrum for $\omega > 0$.

The average sign of the CT-QMC sampling of atom 1 is displayed in Figure 4.27. As for all previous calculations the average sign almost linearly decreases with β. At $\beta = 20$ the sign drops

down to 0.3. This is better by factor of 3 then the standard basis, however, it is worse by more than a factor of 2 then the locally diagonal basis.

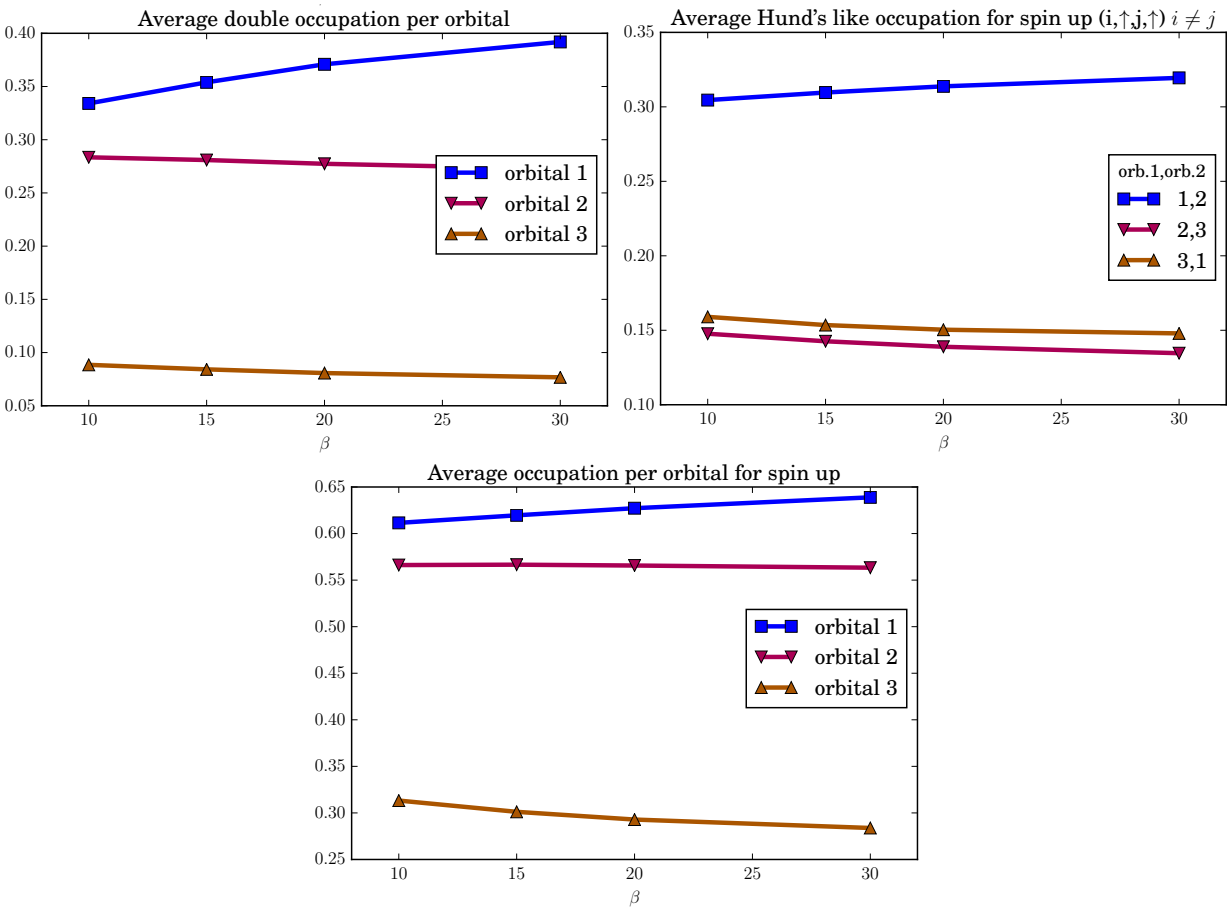

Figure 4.24: β dependence of the occupancies for $\xi = 300\,\text{meV}$ of atom 1. The non-visible point of the average double occupancy of orbital 2 is at 0.27. Both spin channels display the same behavior. The average occupancy and the average double occupancy shows the energetic difference between the orbitals with the biggest occupancy for the energetic lowest lying orbital 1 and a slightly lower occupancy for orbital 2 and much lower occupancy for the energetic highest lying orbital 3. The average double occupancy increases with increasing ξ only for orbital 1, whereas for orbital 2 and 3 it stays almost constant. The Hund's like occupancy shows a large gap between the spin alignment of orbital 1/2 and orbital 1/3 and 2/3. However, there is only a small temperature dependence.

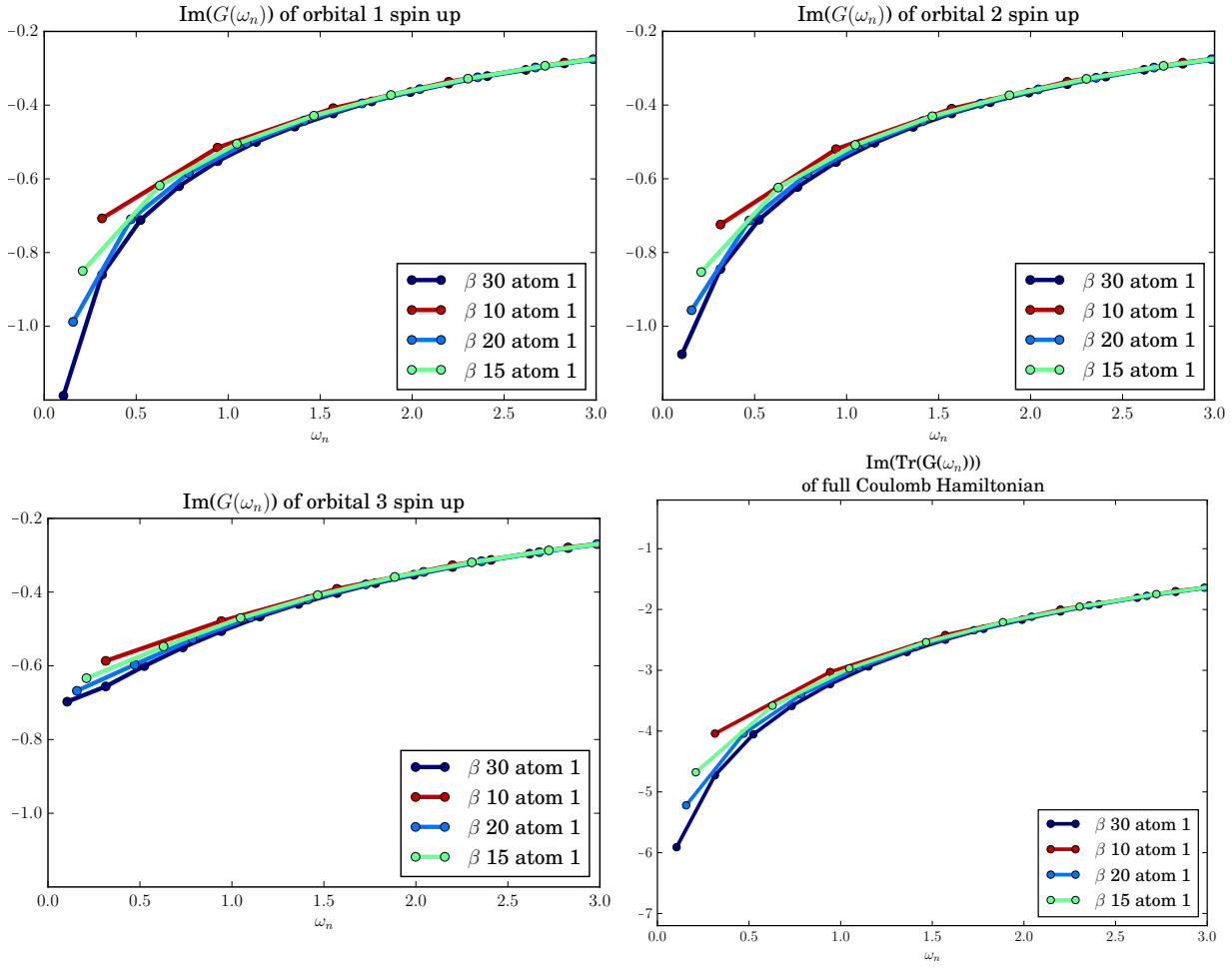

Figure 4.25: Diagonal entries of $\mathrm{Im}[G_{\gamma\sigma,\bar{\gamma}\bar{\sigma}}]$ for $\xi = 300\,\mathrm{meV}$ for atom 1. Both spin channels have equivalent results. There are significant differences between the orbital. Orbital 1 appears overall to be most metallic and also displays the strongest β dependence. Orbital 3 on the other side displays bad metal characteristics for all β values. However, the occupancy of orbital 1 is higher and therefore it contributes most to charge carrier transport.

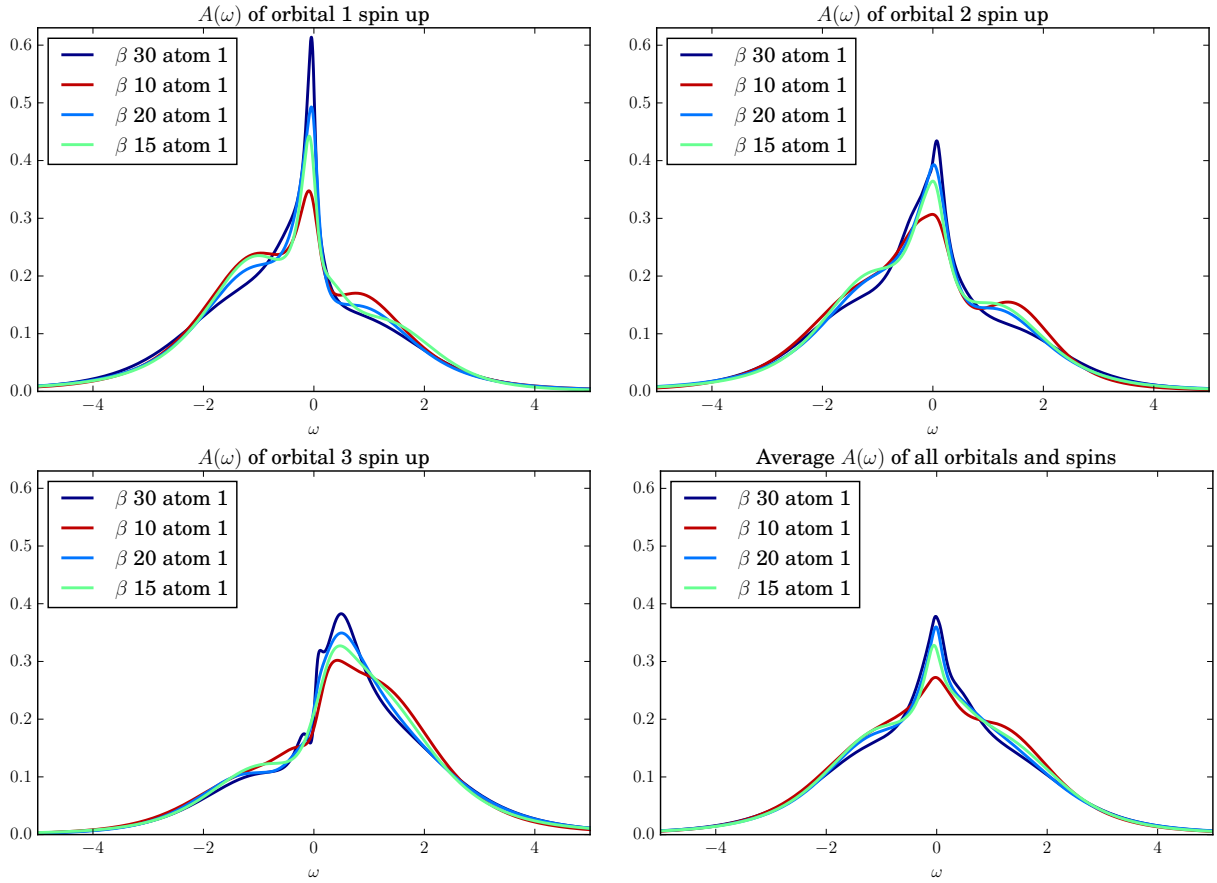

Figure 4.26: Local spectral function for all orbitals (spins are equivalent) and averaged (band and spin) local spectral function (lower right panel) for $\xi = 300\,\text{meV}$. Orbital 1 shows a metallic character for all temperatures, such as orbital 2, which shows less temperature dependence. Orbital 3 has a quasi-particle peak shifted from $\omega = 0$ towards higher ω. The averaged local spectral function shows a well pronounced quasi-particle peak which decreases with decreasing β.

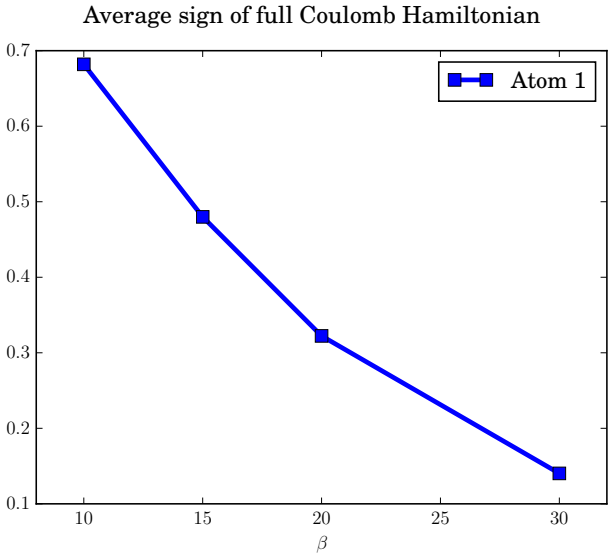

Figure 4.27: β dependence of the average sign of the CT-QMC sampling of atom 1 for $\xi = 300\,\text{meV}$. With increasing β the average sign quickly and almost linearly decreases to 0.14 at $\beta = 30$.

4.5 Locally Diagonal Basis Extended with Spin-Orbit Coupling Diagonalized

In this section we present the results calculated in a fully diagonalized basis, where the spin is added in the locally diagonal basis [6]. This means, in practice, that the Wannier Hamiltonian and the local interaction matrix are rotated into the locally diagonal basis using the scripts from Appendix E and F and, that afterwards, the local spin-orbit coupling is added to every k point of the Wannier Hamiltonian using the script from Appendix H. Eventually the local one-particle coefficient matrix is diagonalized again and the Wannier Hamiltonian and the local interaction coefficient matrix are rotated into this again diagonal basis (scripts from Appendix E and F). Therefore the local one-particle coefficient matrix is diagonal again and the energy splitting of t_{2g} orbitals gets increased with ξ (see Figure 4.1). Once again, what will be referred to as "spin" index is not a physical spin anymore since the diagonalization of the local one-particle coefficient matrix mixes both spin channels.

Most of the figures show only the results of atom 1, because the other atoms are similar. If this is not the case, more atoms are displayed. The same holds for the displayed orbitals.

4.5.1 $\xi = 0.3\,\text{eV}$

In this subsection we present the last results of this thesis. We compare the results of a calculation for $\xi = 300\,\text{meV}$ and $\beta = 10 - 20$ calculated in a fully diagonalized basis with spin-orbit coupling added in the locally diagonal basis. In Figure 4.28 the occupancies of atom 1 are displayed. The general trends are very similar to the results in the fully diagonalized standard basis. Only the

[6] For this basis we where not able to perform a study with increasing ξ for $\beta = 10$ in the given time.

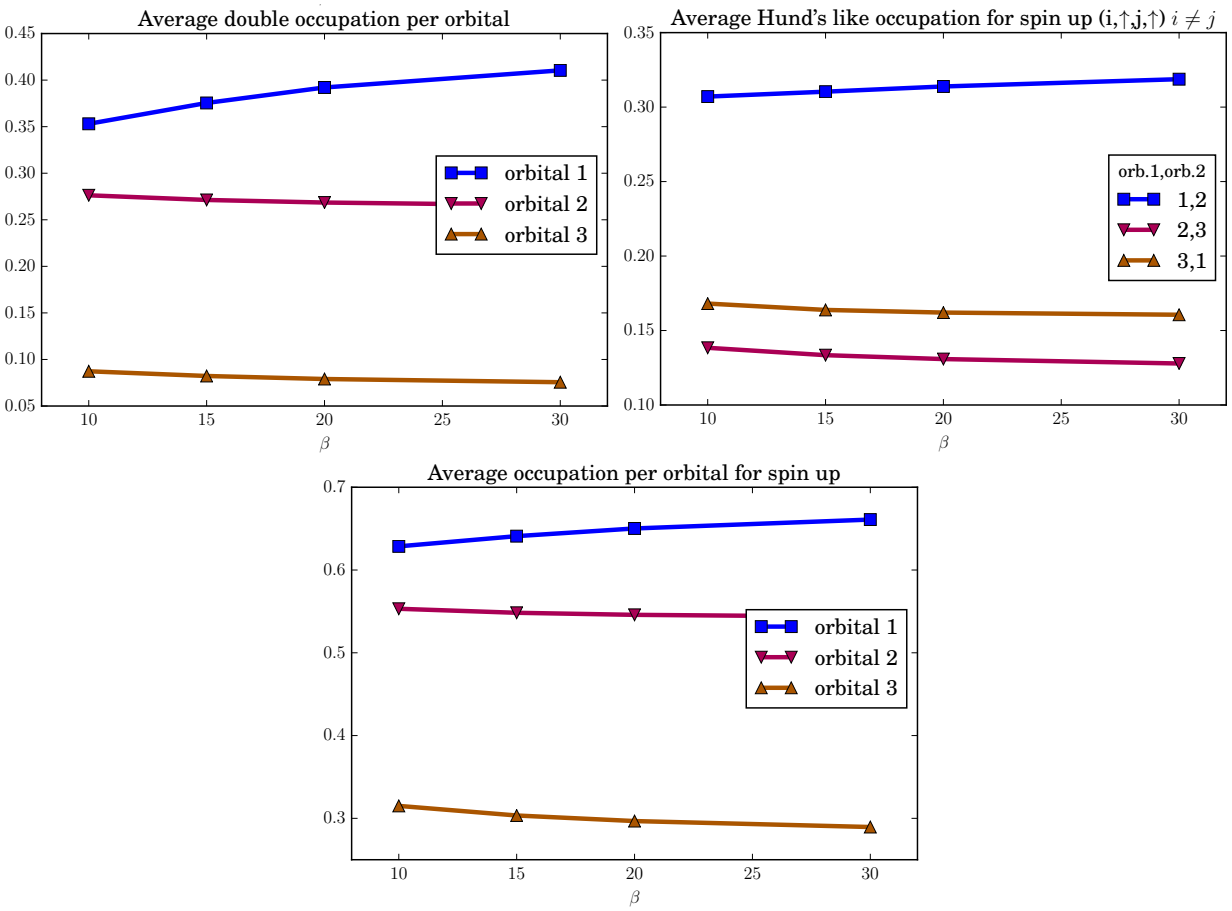

Figure 4.28: β dependence of the occupancies of atom 1 for $\xi = 300\,\text{meV}$. Both spin channels display the same behavior. The average occupancy and the average double occupancy shows the energetic difference between the orbitals with the biggest occupancy for the energetic lowest lying orbital 1 and a slightly lower occupancy for orbital 2 and much lower occupancy for the energetic highest lying orbital 3. The average double occupancy increases with increasing ξ only for orbital 1, whereas for orbital 2 and 3 it stays almost constant. The Hund's like occupancy shows a large gap between the spin alignment of orbital 1/2 and orbital 1/3 and 2/3 and a small one for the later two. However, there is only a small temperature dependence.

separation of the average Hund's like occupation of orbitals 1,3 and 2,3 is increased, indicating an increase of localization in orbital 1 compared to the fully diagonalized standard basis. This is directly inherited to the imaginary part of the diagonal terms of the local Matsubara Green's function of atom 1 displayed in Figure 4.29. In this basis orbital 2 displays more metallic characteristics than orbital 1. Also the temperature trend is more pronounced for orbital 2. Note that this is the reversed situation from the fully diagonalized standard basis, where orbital 1 is more metallic (compare Figure 4.25). Orbital 3 behaves like in the fully diagonalized standard basis and shows bad metal characteristics and almost no temperature trend. Also the trace of the Green's function behaves similar than in the fully diagonalized standard basis, losing its metallic properties with increasing β.

The local spectral function displayed in the upper four panels of Figure 4.30 shows different behaviour for all 3 orbital. Orbital 1 shows a quasi-particle peak which is broadened for $\omega < 0$ and decreases with decreasing β. Orbital 2 shows a very narrow quasi-particle peak, which loses

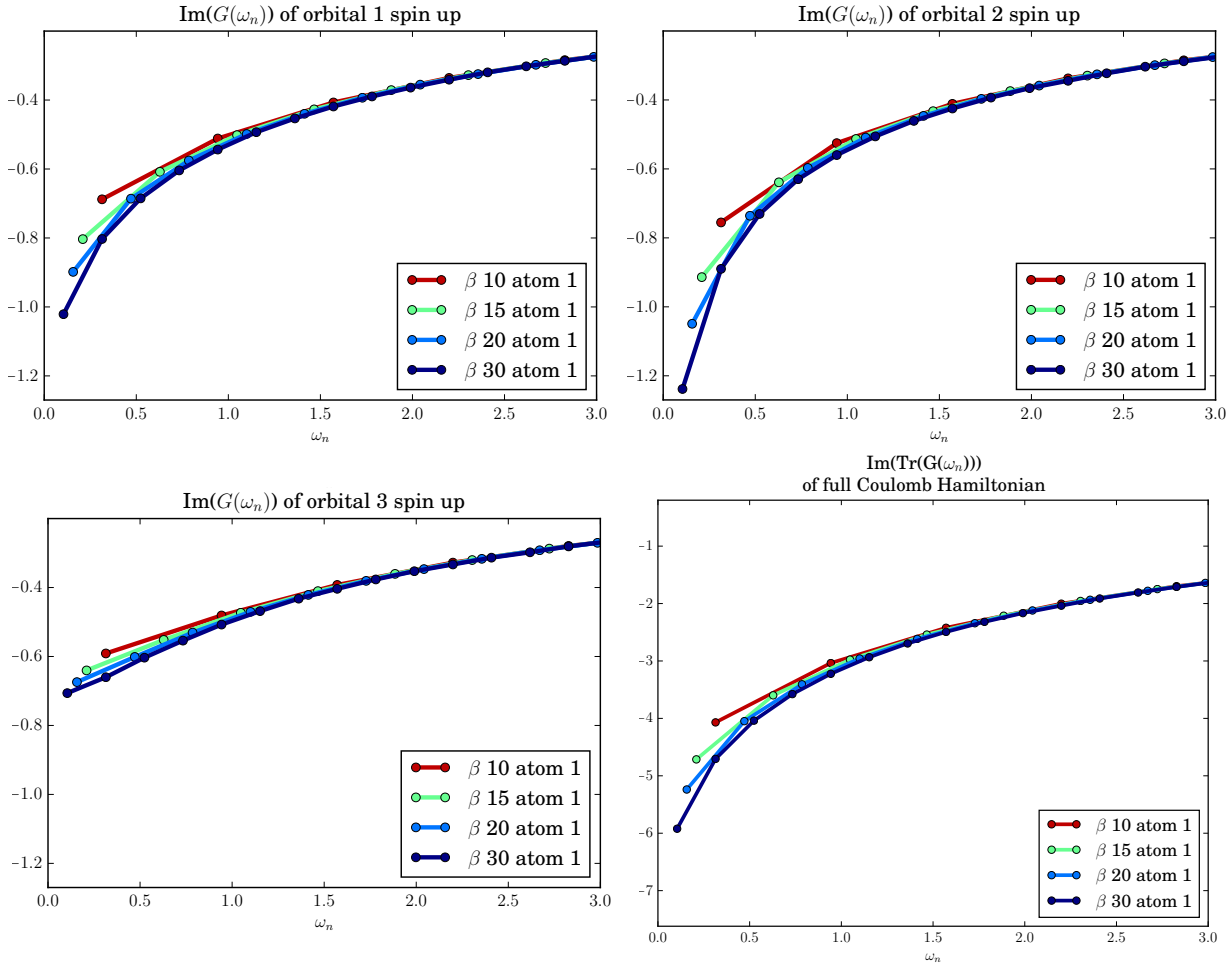

Figure 4.29: Diagonal entries of $\mathrm{Im}[G_{\gamma\sigma,\bar{\gamma}\bar{\sigma}}]$ of atom 1 for $\xi = 300\,\mathrm{meV}$. Both spin channels have equivalent results. There are significant differences between the orbital. Orbital 2 appears overall to be most metallic and also displays the strongest β dependence. Orbital 3 on the other side displays bad metal characteristics for all β values.

weight with decreasing β and the onset of a small side peak at $\omega = -2$, which slowly rises for decreasing β. Similar to the fully diagonalized standard basis orbital 3 shows a broad peak between $\omega = 0$ and 3. There is only very weak temperature trend, which slightly decreases the peaks high and broadens it with decreasing β. The average local spectral function is again very similar to the fully diagonalized standard basis and shows a quasi-particle peak which gradually loses weight and coherence with increasing temperature. This is very similar to the average local spectral function calculated in fully diagonalized standard basis, indicating that on average it is not so important whether the spin-orbit coupling is added in the standard or the locally diagonal basis.

The average sign of the CT-QMC sampling is displayed in the lowest panel of Figure 4.30. As for all previous calculations it almost linearly decreases with increasing β. At $\beta = 20$ it is 0.27, which is slightly lower than in the fully diagonalized standard basis. Although the calculations in the fully diagonalized bases do yield the experimentally observed paramagnetic phase the sign is significantly worse than in the locally diagonal (Hloc) basis.

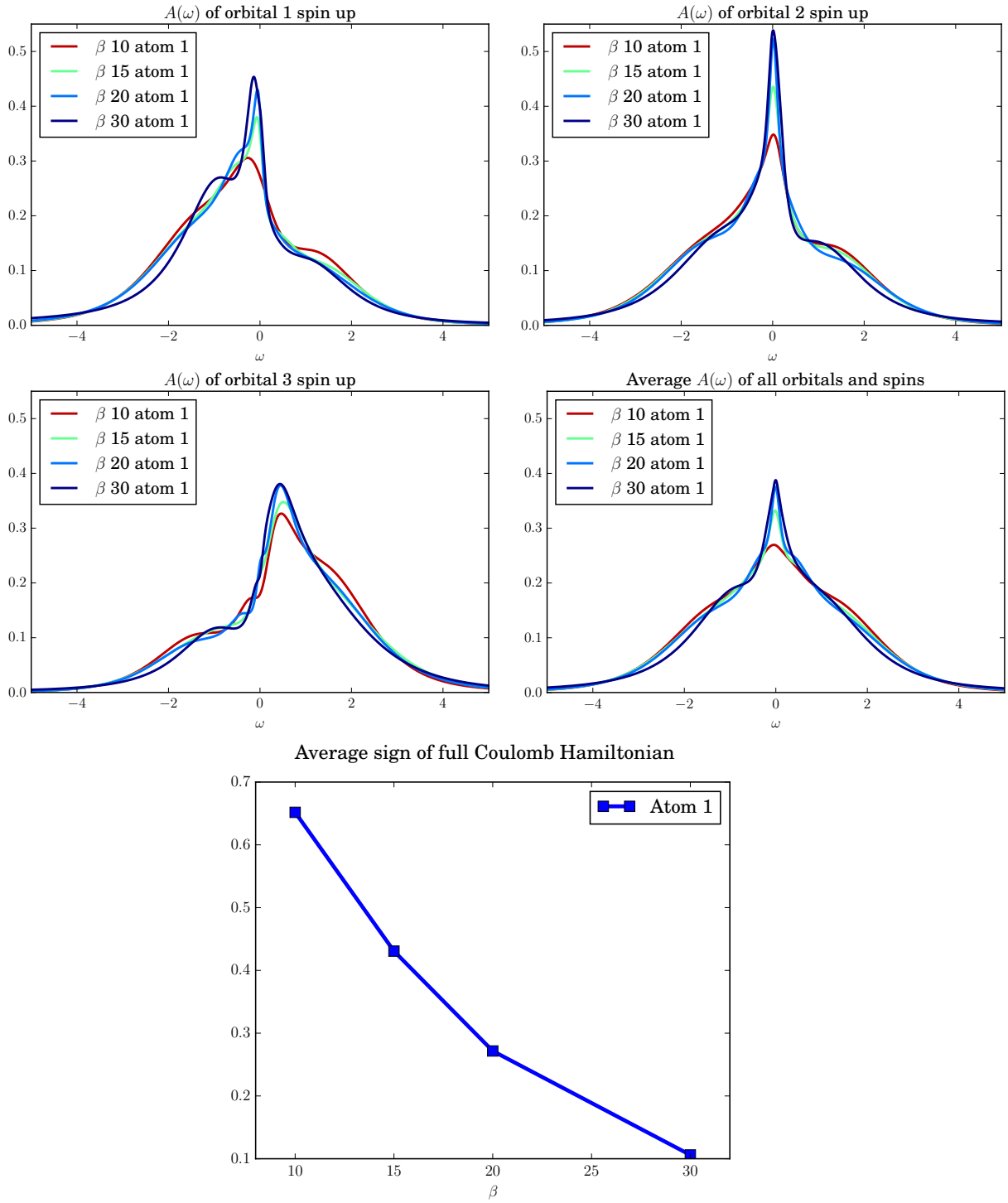

Figure 4.30: Local spectral function for all orbitals (spins are equivalent), averaged (band and spin) local spectral function (middle right panel) and average CT-QMC sign of atom 1 for $\xi = 300\,\text{meV}$. The local spectral function of orbital 2 shows a metallic character for all temperatures, such as orbital 1, which shows less temperature dependence. Orbital 3 has a quasi-particle peak shifted from $\omega = 0$ towards higher ω. The averaged local spectral function shows a well pronounced quasi-particle peak which decreases with decreasing β. The average CT-QMC sing quickly decreases almost linearly with increasing β. At $\beta = 20$ it is already down to 0.1.

Chapter 5

Conclusion

The numerical results presented in this work have revealed multifaceted aspects of local spin-orbit coupling effects in $LiOsO_3$.

First of all, we have found that the splitting of the t_{2g} degeneracy induced by the trigonal distortion of the oxygen octahedron in $LiOsO_3$ becomes further enhanced when local spin-orbit coupling is included to the one-particle Hamiltonian of the 5d t_{2g} orbitals of Os. This is directly reflected in the local orbital occupancies, as the four energetic lower lying orbitals get on average significantly more populated than the two higher lying orbitals (further magnifying a trend already observed in the absence of local spin-orbit coupling). Therefore, introducing the local spin-orbit coupling drives the t_{2g} manifold of $LiOsO_3$ further away from the half-filling condition for each orbital, gradually weakening the Hund's localization effects. At the same time, the double occupancy for the lower orbitals increases with increasing coupling strength. Both effects are expected to drive the system towards a more metallic solution. In fact, this trend is indeed observed in our DMFT results. A comparison of the local spectral function at various temperatures for calculations with and without local spin-orbit coupling is presented in Figure 5.1. Our calculations with the estimated coupling strength of $\xi = 300\,\mathrm{meV}$ appear to be overall more metallic than the ones with $\xi = 0\,\mathrm{meV}$, with larger differences observed at very high temperatures (T=1160 K). This trend can already be inferred from the first few Matsuabra frequencies of the local Matsubara Green's function, avoiding the analytical continuation, displayed in the inset of Figure 5.1. Local spin-orbit coupling also smears out the slightly pronounced side peaks, which are present in the local spectral functions without local spin-orbit coupling.

Evidently, the possible compensation between the lifting of the t_{2g} degeneracy due to the trigonal crystal field splitting in $LiOsO_3$ and the local spin-orbit coupling strength, which are roughly of the same magnitude, does *not* actually occur. Hence, the theoretical explanation of the high temperature bad metal behavior of $LiOsO_3$ needs further investigation. There are two possibilities which seem to be quite plausible: (i) The screening of the local Coulomb interaction is overestimated by cRPA, which yields too small U, J and V interaction parameters and a too weak localization. This will be rather simple to investigate by gradually increasing the whole $U_{\gamma_1\gamma_2\gamma_3\gamma_4}$ local interaction matrix. (ii) The *non-local* spin-orbit coupling effect play a pivotal role in this material. To investigate this, a first insight can be obtained by comparing a DFT

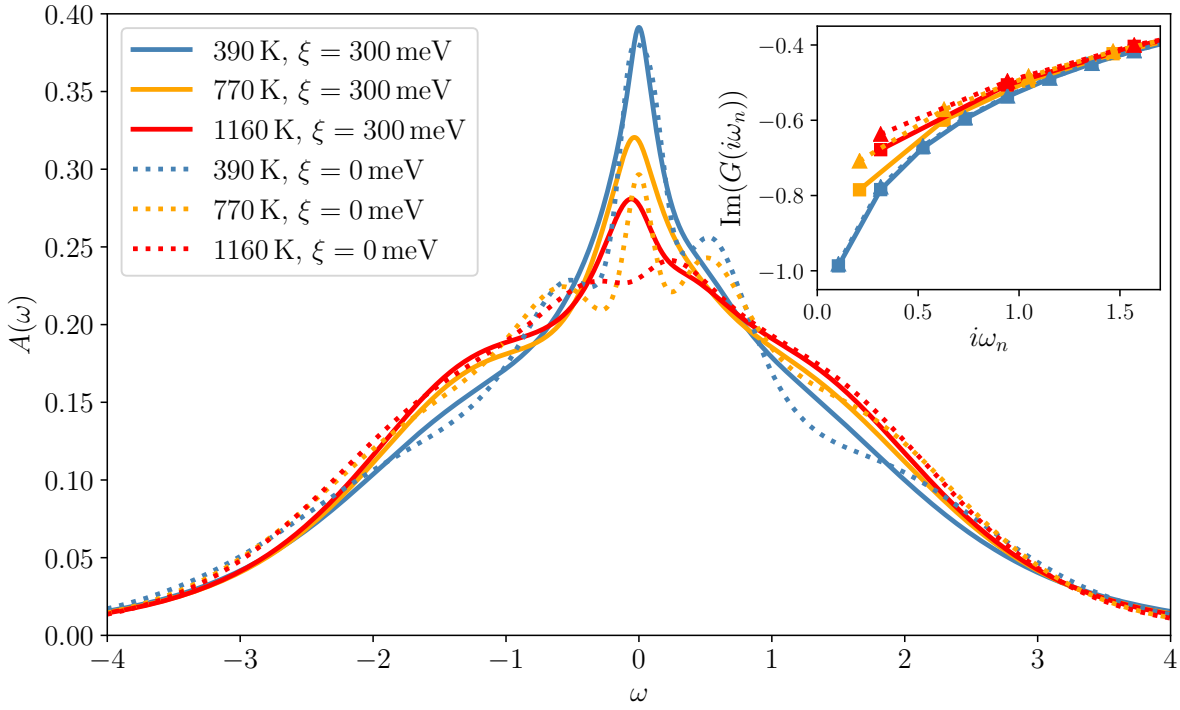

Figure 5.1: Local spectral function of $LiOsO_3$ averaged over all orbitals and spins of atom 1 at various temperatures with (full lines) and without (dashed lines) local spin-orbit coupling calculated in the fully diagonalized locally diagonal (Hloc diagonal) basis. The inset shows the corresponding local Matsubara Green's functions. The temperature trend is similar with and without local spin-orbit coupling, though in the former case the spectral functions are overall more metallic.

calculation including the full spin-orbit coupling to one with local (atomic) spin-orbit coupling only. If the *non-local* spin-orbit coupling turns out to be important at the level of DFT, it will most likely also influence the physics in this material in presence of correlations. However, in order to perform a fully ab-initio DFT+DMFT calculation in a Wannier basis including non-local spin-orbit coupling, to our knowledge, further implementations in the cRPA algorithm are necessary.

Another important extension of this work would be to compute the corresponding optical conductivities in the DFT+DMFT approximation. This has not been done in this project, because to do so it is necessary to analytically continue all elements of the local self-energy with a sufficient degree of precision. Especially for systems with large spin-orbit coupling strength and for low temperatures this will require much higher statistics, i.e. more runtime, to obtain smooth functions for the off-diagonal local self-energy in our CT-QMC framework. On the other hand, to make a more direct comparison to the experiment this step will be crucial for future studies on this subject.

This diploma thesis, in any case, has gone beyond showing that local spin-orbit coupling is *not* counterbalancing the observed metallicity from previous calculations (but reinforces it). In fact, our DMFT calculations without spin-orbit coupling have also shown that $LiOsO_3$ has a strong tendency to develop an antiferromagnetic long-range order. It is remarkable, that including local

Basis	0 meV	50 meV	300 meV	400 meV	500 meV	600 meV	≥2 eV
LS	**AF** ($\beta \geq 10$)	-	**AF** ($\beta \geq 10$)	**AF** ($\beta \geq 10$)	**AF** ($\beta \geq 15$)	**AF** ($\beta > 20$)	**PM**
Hloc	**AF** ($\beta \geq 10$)	-	**AF** ($\beta \geq 10$)	**AF** ($\beta \geq 15$)	**PM** ($\beta \leq 20$)	**PM** ($\beta \leq 20$)	**PM**
LS diagonal	**AF** ($\beta \geq 10$)	**PM** ($\beta \leq 20$)	**PM**	**PM**	**PM**	-	**PM**
Hloc diagonal	**AF** ($\beta \geq 10$)	**PM** ($\beta \leq 20$)	**PM**	-	-	-	-

Table 5.1: This table summarizes the magnetic order found in our DMFT calculations. The β values indicate the regime where the respective phase is stable. If there is no β value displayed the phase was stable in all our calculations and we assume it to remain stable also at lower temperatures.

spin-orbit coupling drives the material back towards a paramagnetic phase, where the transition appears rather abrupt than smooth. The strength of the local (atomic) spin-orbit coupling necessary to obtain a paramagnetic phase, is significantly basis dependent. This is displayed in Table 5.1. Both bases where the local one-particle coefficient matrix $\epsilon_{\gamma\sigma,\bar{\gamma}\bar{\sigma}}$ is diagonal (LS diagonal and Hloc diagonal) show a much weaker tendency towards an antiferromagnetic phase. Already a spin-orbit coupling strength ξ of 50 meV [1] is enough to overcome the border to a paramagnetic phase. In comparison to the non diagonal bases (LS and Hloc), where one needs a spin-orbit coupling strength ξ of about 400 meV [2]to 600 meV to suppress the antiferromagnetic order.

This phenomenon, which emerged from our most recent calculations, is not yet fully understood and needs further investigation to clarify whether it is in fact a numerical or truly physical effect. As a first step it is necessary to understand whether the inter-atomic terms of the first Brillouin zone included in the full Wannier Hamiltonian are most responsible for the development of the antiferromagnetic phase. If *not*, the intra-atomic interaction is inducing the antiferromagnetic phase and, furthermore, it is worth investigating whether this effect is driven by the local interaction terms $U_{\gamma_1\gamma_2\gamma_3\gamma_4}$ or by the local one-particle terms $\epsilon_{\gamma\bar{\gamma}}$.

Finally, the development of an algorithm enforcing a paramagnetic phase is needed for further realistic calculations including spin-orbit coupling of materials such as $LiOsO_3$, which are known to be paramagnetic in the whole experimentally accessible temperature range.

[1] Our most recent calculations in the LS diagonal and the Hloc diagonal basis for $\xi = 50$ meV show a paramagnetic phase for $\beta = 10$ and 20. We have no knowledge about lower temperatures yet.

[2] Our most recent calculations in the Hloc basis for $\xi = 400$ meV show the onset of an antiferromagnetic phase for $\beta = 15$ and 20.

Appendices

Appendix A

Additional Results

A.1 $\beta = 5$ Standard Basis

This subsection contains results for ξ values in the range of 0-8 eV [1] for $\beta = 5$, i.e. T=2320 K. This temperature is far above all measured temperatures and $LiOsO_3$ is most likely already melted at this temperature. However, it is interesting from a theoretical standpoint as the calculations do not show an antiferromagnetic phase at this temperature. Therefore, this temperature is suitable to describe the influence of spin-orbit coupling to a paramagnetic solution of $LiOsO_3$.

To get a first insight, the left panels of Figure A.1 display the imaginary part of the diagonal elements of the local self-energy $\Sigma_{\gamma\sigma,\bar{\gamma}\bar{\sigma}}(\omega_n)$ for ξ values ranging from 0 to 2 eV. Somewhat at first sight surprisingly, there are no differences between the diagonal self-energies of the orbitals. Apparently the orbital and spin off-diagonal elements introduced with the spin-orbit coupling (1.3) do *not* alter the orbital equivalence of the diagonal elements of the imaginary part of the self-energy. The changes driven by ξ are, in any case, well pronounced and show a visible decrease of the local self-energy close to $\omega_n = 0$, which would indicate a further metallization of this material at such a high temperature. However, in this basis there are also non-vanishing off-diagonal elements (not shown). For those, however, a direct physical interpretation is considerably more complicated as compared to the diagonal elements. The overall effect of the self-energy can be better understood by looking at the Matsubara Green's function.

However, before we do so, in order to obtain a deeper insight, we take a look at the right panels of Figure A.1, which shows the occupancies of the calculations. Consistent with the equivalence of the orbital diagonal terms of the self-energy, the average occupation of each orbital (lower right panel) is about 0.5 for all ξ, i.e. all orbitals are nominally half-filled. The average double occupation per orbital shows a strong ξ dependence, ranging from 0.09 at $\xi = 0$ eV to 0.2 at $\xi = 2$ eV. This trend decreases for even larger values if $\xi > 2$ (not displayed), probably converging towards a *relative* double occupation of 1, which is the non-correlated case. This trend is matched by the trend of the relative Hund's like occupation (upper right panel) which shows a decrease with increasing ξ, indicating a loss of localization of charge carriers. The differences of

[1] Most figures display only results for $\xi = 0 - 2$ eV. The results for $\xi > 1$ are, of course, not realistic. However, in order to show clear trends we include this calculations.

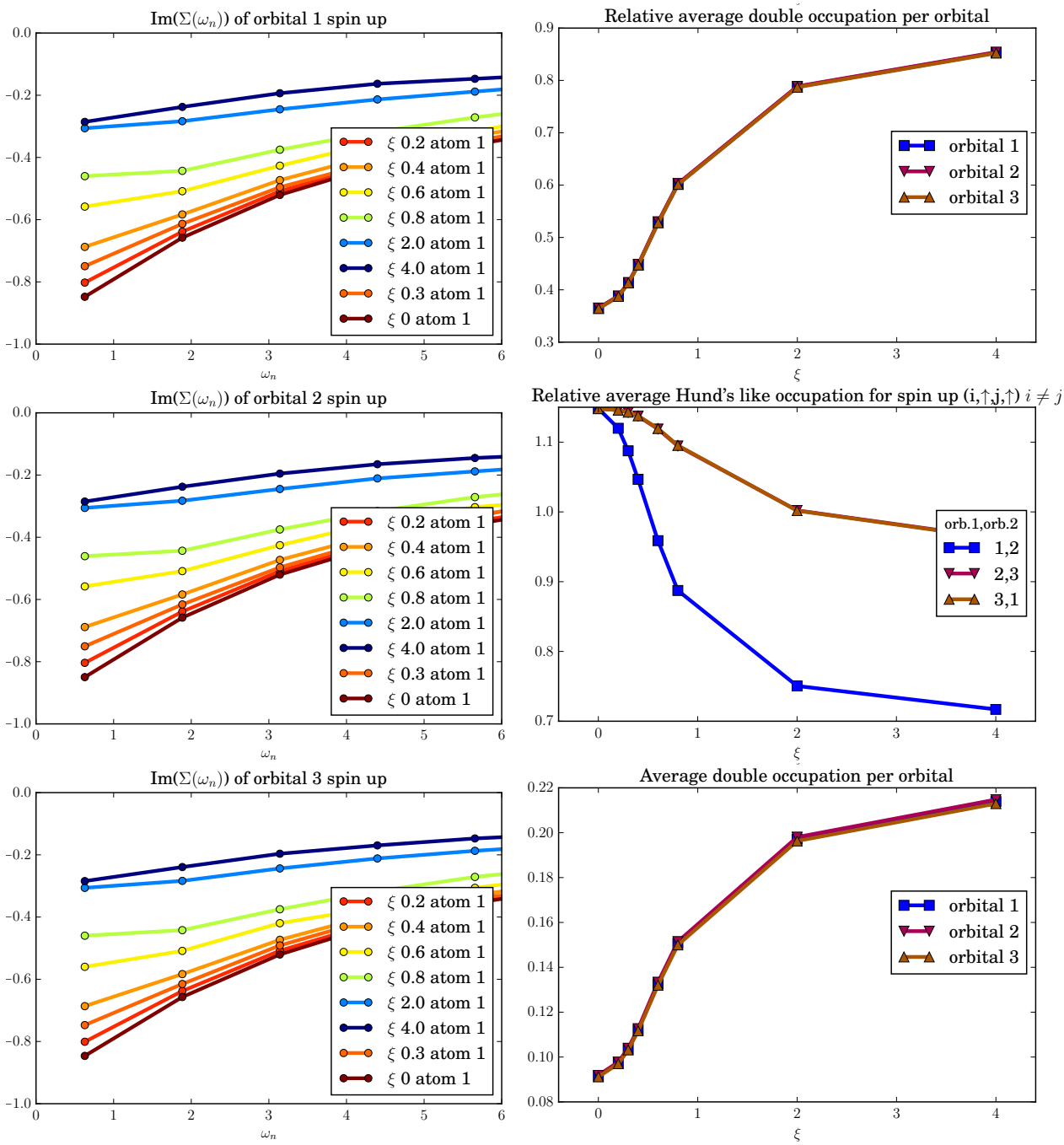

Figure A.1: Diagonal entries of $\mathrm{Im}[\Sigma_{\gamma\sigma,\bar{\gamma}\bar{\sigma}}]$ of atom 1 for $\beta = 5$ at various valus of ξ in eV and ξ (eV) dependence of the occupancies of atom 1 for $\beta = 5$, where the term "relative" refers to terms of the form $\frac{\langle n_{\gamma\sigma} n_{\bar{\gamma}\bar{\sigma}} \rangle}{\langle n_{\gamma\sigma} \rangle \langle n_{\bar{\gamma}\bar{\sigma}} \rangle}$. Both spin channels display the same behavior. At this temperature for the self-energy also the orbitals are equivalent. For the self-energy all orbitals display a slow trend towards small local self-energy for larger ξ. The double occupancy increases with increasing ξ, whereas the Hund's like occupancy decreases. The spin alignment between the orbitals 1 and 2 decreases very fast.

the spin alignment between orbitals 1,3 2,3 and 1,2 are significant and indicate that after all not all orbitals behave equivalent.

Finally Figure A.2 displays the imaginary part of the trace of the local Matsubara Green's function (upper left panel) (The diagonal elements of $G_{\gamma\sigma,\bar{\gamma}\bar{\sigma}}$ are equivalent for all orbitals and spins), the corresponding average local spectral function (lower panel) and the average sign of the CT-QMC sampling (upper right panel) of atom 1. The strong ξ dependency seen in the local self-energy (compare Figure A.1) is only partially reflected in the local Matsubara Green's function. Surprisingly, it shows a well pronounced tendency towards larger values for the first few Matsubara frequencies, i.e. an insulating trend. This is opposed to what we would expect from the diagonal elements of the self energy. Hence, this trend has to be induced by the off-diagonal

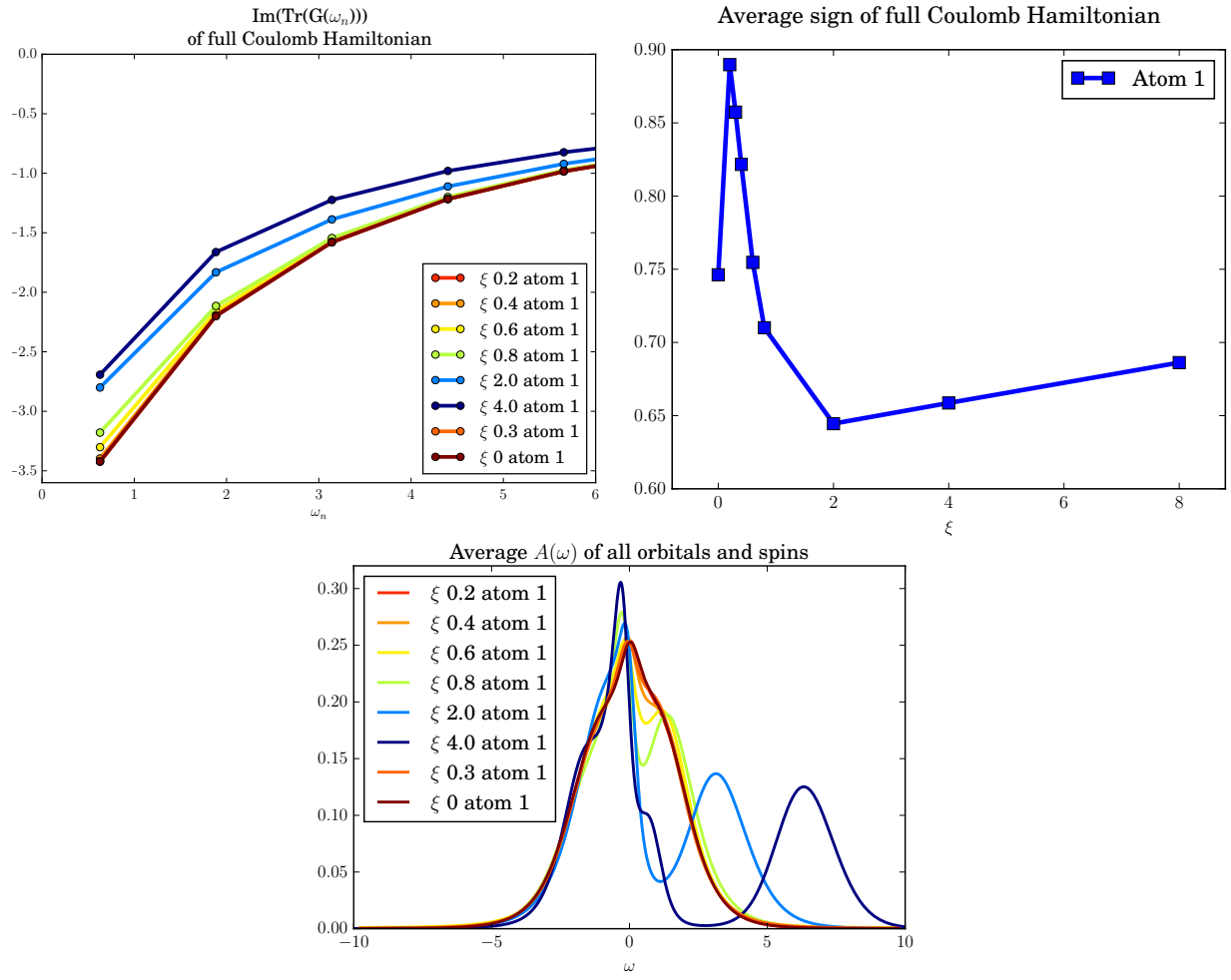

Figure A.2: Trace over all orbitals and spins of the local Matsubara Green's function for various values of ξ (eV) (upper left panel) and ξ (eV) dependence of the average sign of the CT-QMC sampling (upper right panel) and average local spectral function of atom 1. The changes with ξ in the self energy and the occupancies (Figure A.1) are also reflected in the local Matsubara Green's function and the average local spectral function. The local Matsubara Green's function shows an insulation trend with increasing ξ, as does the spectral function which gradually shifts weight towards the second peak at $\omega > 0$. However, the sign of the calculation is heavily influenced by ξ, quickly dropping to 0.64 at $\xi = 2\,\mathrm{eV}$. For larger $\xi > 2\,\mathrm{eV}$ the sign increases again.

terms. This insulating trend is reflected in the corresponding average local spectral function. The quasi-particle peak gets slightly shifted towards $\omega < 0$ reducing the spectral weight at $\omega = \mu$. At the same time, the peak significantly narrows and a second peak at $\omega > 0$ rises. For very high values of $\xi = 4\,\text{eV}$ where the spin-orbit coupling probably the dominate role this peak is separated from the quasi-particle peak by a gap (only almost for $\xi = 4$).

The average sign of the CT-QMC sampling shows a very significant trend, rapidly decreasing with increasing ξ (except at $\xi = 0$, where the sign is smaller). It reaches its minimum of 0.64 at $\xi = 2\,\text{eV}$. For larger $\xi > 2\,\text{eV}$ the sign slightly increases again.

Overall at this temperature there is trend towards a more insulting solution, which is displayed in the trace of the local Matsubara Green's function and the average local spectral function Figure A.2 but *not* in the double and Hund's like occupations (Figure A.1), which shows strong indications for a delocalization of electrons. However, eventually the physics is described by the local spectral function. The trend found at this temperature is yet not fully understood, as it is opposed to what we have seen at lower temperatures (compare the results from section 4.4.1) [2]. This is to be studied in upcoming projects.

A.2 $\beta = 5$ Locally Diagonal Basis

In this subsection we present the results $\beta = 5$, i.e. T=2320K, and various values of ξ. This temperature is of course, as already mentioned, far above experimental measurements, however, calculations do *not* show an antiferromagnetic phase at this temperature and are therefore suited to describe the influence of spin-orbit coupling on a DMFT (CT-QMC) calculation in the paramagnetic phase, which is also experimentally observed.

A first insight is given by Figure A.3 which shows the imaginary part of the diagonal elements of the local self-energy for all three orbitals (both spin channels are equivalent). Orbital 1 and 2 (upper panels) display equivalent bad metallic behavior, with decreasing values for increasing spin-orbit coupling strength. Also orbital 1 displays a bad metal behavior, however, for large spin-orbit coupling strength the slop close to $\omega_n = 0$ is more metallic than for orbitals 1 and 2. Overall the self-energy has a metallizing trend.

The occupancies shown in Figure A.4 have a very pronounced trend with increasing ξ. The loss of degeneracy in the orbitals is reflected in the average occupancy per orbital (upper right panel) which shows that the energetic lower lying orbitals 1 and 2 are more occupied than orbital 3. This difference increases with increasing ξ yielding a difference of 0.1 between the upper and the lower orbital. Furthermore, it is also reflected in the average double occupancy, where the gap between orbital 1 and 2 and orbital 3 also increases with increasing spin-orbit coupling strength and the relative average Hund's occupancy where the spin alignment between orbital 1 and 2 and orbital 1 and 3 is significantly larger then between orbital 1 and 2. In general increasing ξ decreases the (localizing) effect of the Hund's exchange. This is not surprising as spin-orbit coupling introduces spin flip terms to the local one-particle Hamiltonian allowing previously aligned spins to dis align.

[2] In the estimated realistic regime of $\xi = 300\,\text{meV}$ the calculation at $\beta = 5$ shows almost no change in the local spectral function w.r.t to the $\xi = 0\,\text{meV}$ calculation. Therefore, this is really to be understood as a trend study.

As in the standard basis the effect on the slope of the imaginary part of the trace of the local Matsubara Green's function, displayed in the upper left panel of Figure A.5, is counter intuitive. For increasing ξ the Green's functions slope for the first few Matsubara frequency shows an insulating trend. This is opposed to the self-energy and the behavior of the double occupancy. It is, however, also reflected in the average local spectral function, which is displayed in the lower panel of Figure A.5. As in the standard basis the more insulating slope in the Matsubara Green's function is reflected by a shift of the quasi-particle peak towards $\omega < 0$ and the onset of second peak. The second peak is located at $\omega > 0$ and separates form the quasi-particle peak with increasing ξ. Again, this behavior is in contrast to the trends observed at lower temperatures.

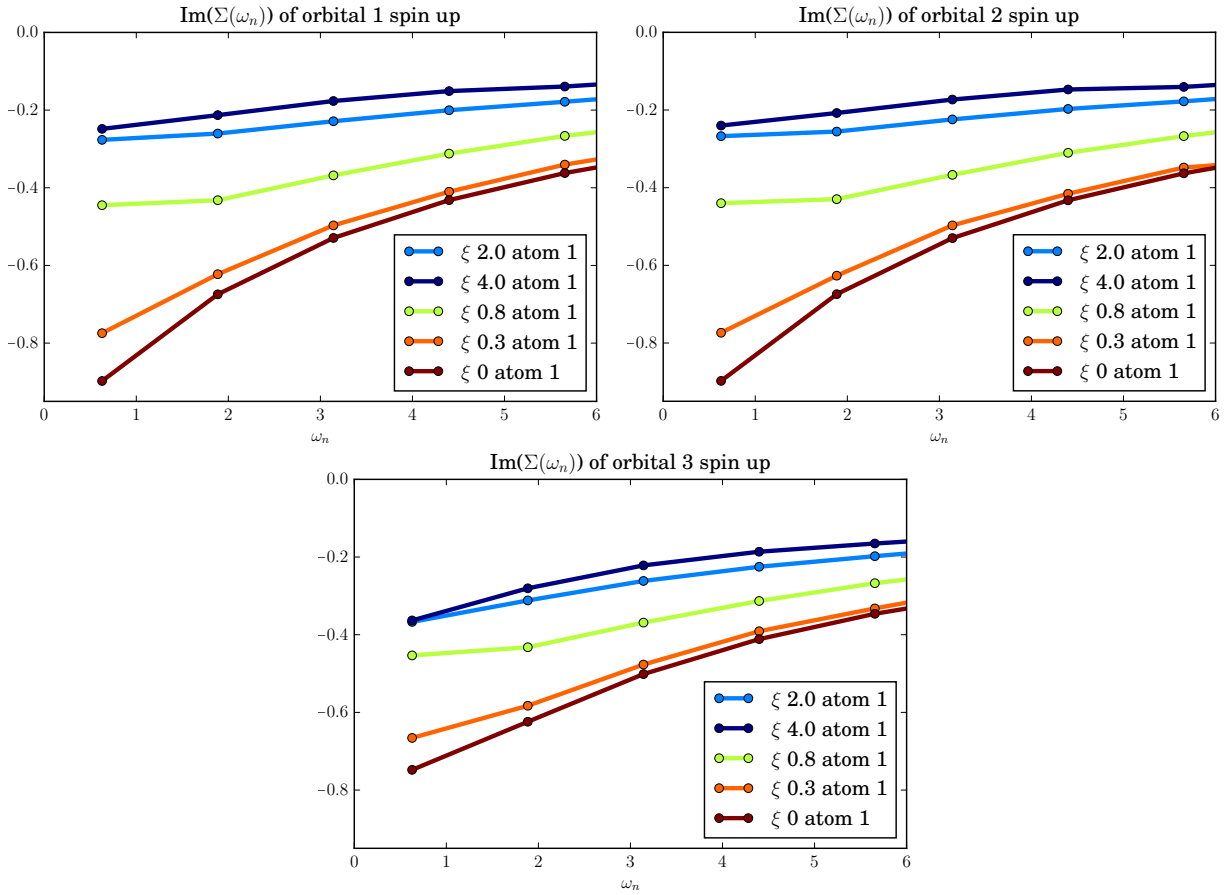

Figure A.3: Diagonal entries of $\mathrm{Im}[\Sigma_{\gamma\sigma,\bar{\gamma}\bar{\sigma}}]$ of atom 1 for $\beta = 5$ and various valus of ξ in eV. Both spin channels have equivalent results. All orbitals display a trend towards smaller local self-energy at the first few Matsubara frequencies for larger ξ. However, this trend converges around $\xi = 4\,\mathrm{eV}$. Orbital 3 appears slightly more metallic for $\xi = 0.3\,\mathrm{eV}$ and slightly less metallic for $\xi \geq 2\,\mathrm{eV}$.

The behavior of the average sign of the CT-QMC sampling, however, is in agreement with all previous calculation and is presented in the upper right panel of Figure A.5. It rapidly decreases with ξ (0.8 at $\xi = 2\,\mathrm{eV}$). However, in difference to the standard basis it does not show a minimum at $\xi = 2\,\mathrm{eV}$ but goes on decaying for all calculated values of ξ. From the collected data it is not possible to tell whether there is a minimum at higher ξ or whether the sign converges towards a fixed value. After all at this temperature the locally diagonal basis performs better than the standard basis for all calculated ξ w.r.t the average sign.

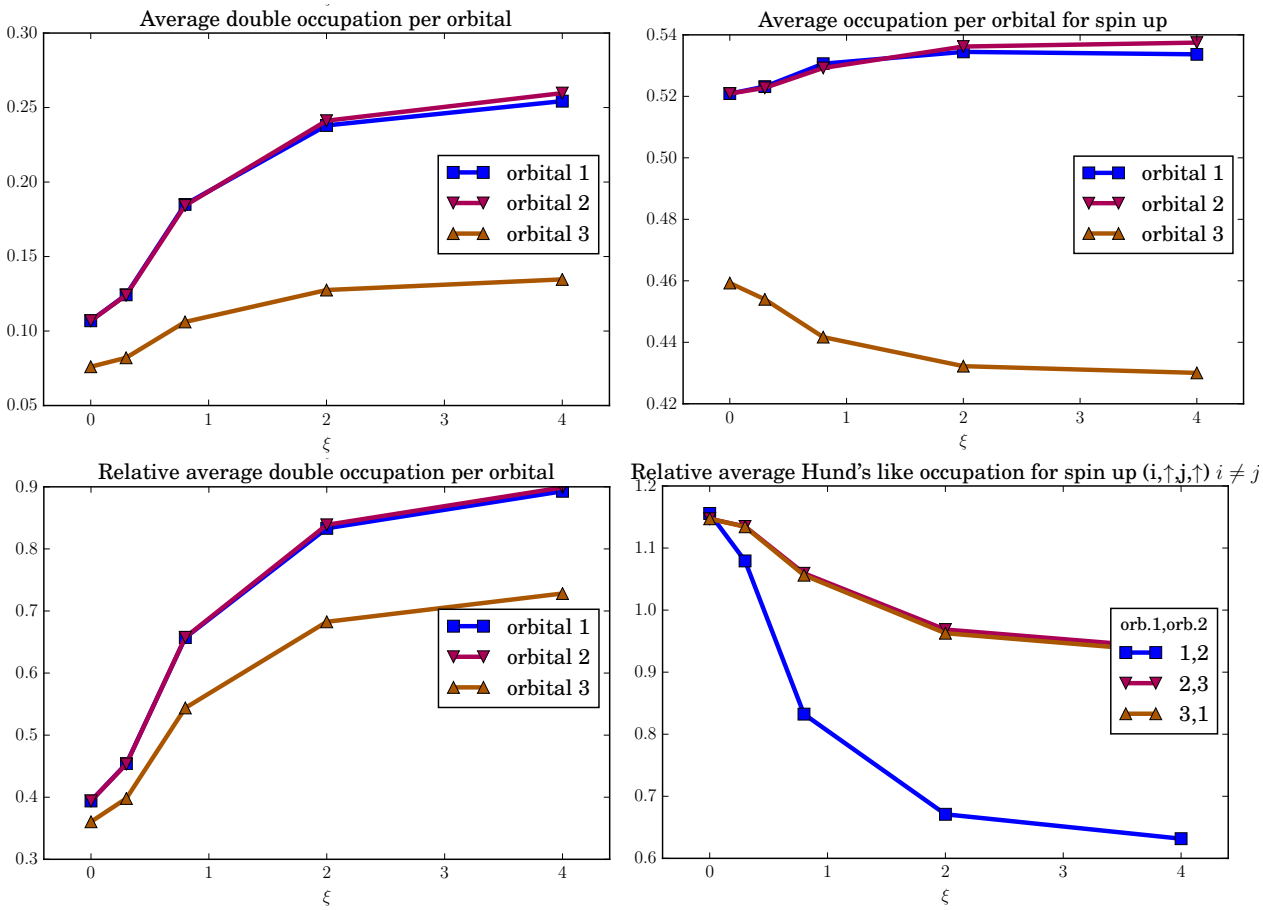

Figure A.4: ξ (eV) dependence of the occupancies of atom 1 for $\beta = 5$, where the term "relative" refers to terms of the form $\frac{\langle n_{\gamma\sigma} n_{\bar{\gamma}\bar{\sigma}} \rangle}{\langle n_{\gamma\sigma} \rangle \langle n_{\bar{\gamma}\bar{\sigma}} \rangle}$. Both spin channels display the same behavior. The average occupation for orbitals 1 and 2 slightly increases whereas the for orbital 3 it decreases. Overall this further increases the gap between orbitals 1 and 2 and orbital 3. The double occupancy increases with increasing ξ, whereas the Hund's like occupancy decreases. The spin alignment between the orbitals 1 and 2 decreases very fast, indicating a metallic behavior of this two bands.

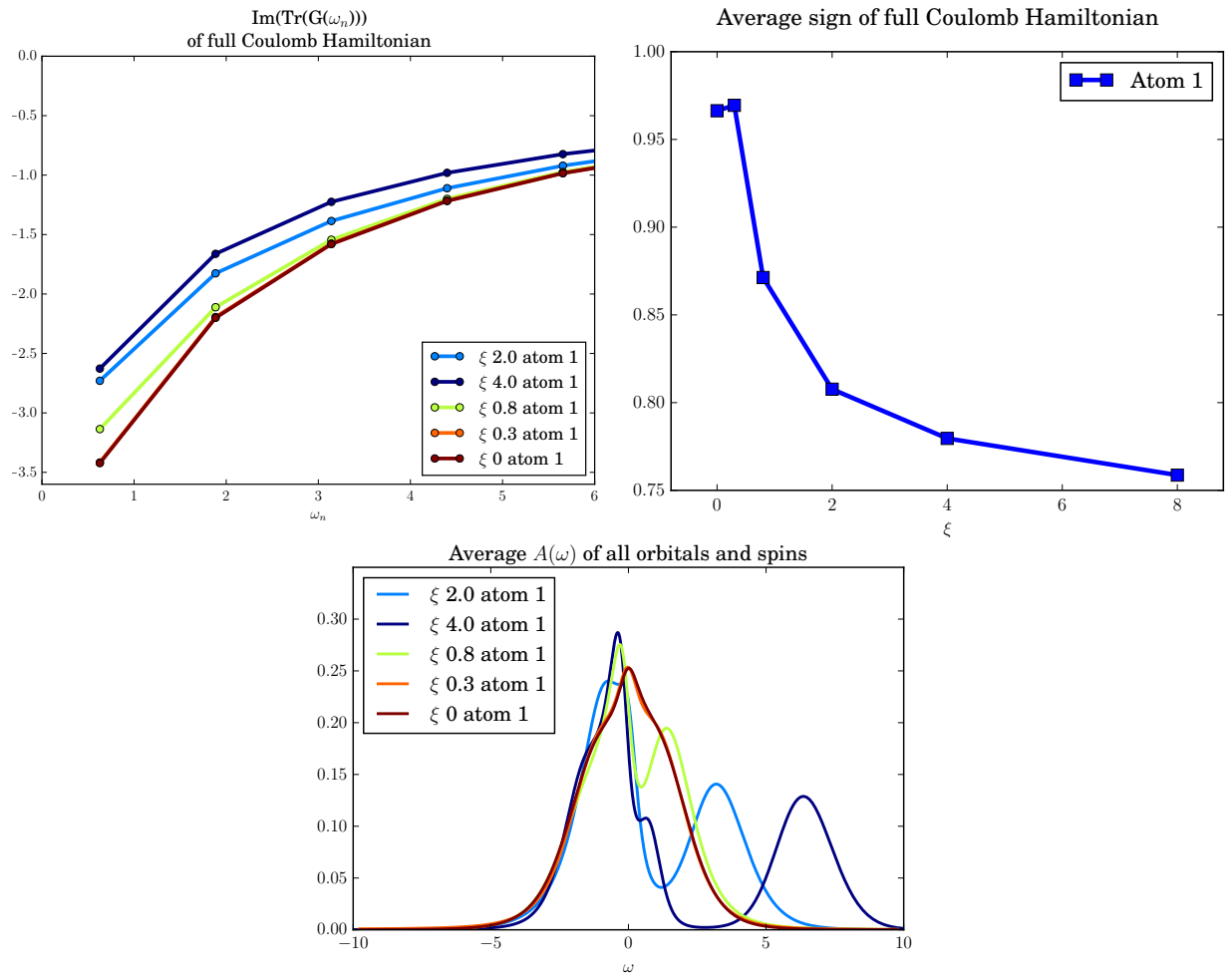

Figure A.5: Imaginary part of the trace over all orbitals and spins of the local Matsubara Green's function of atom 1 for various values of ξ (eV) (upper left panel) and ξ dependence of the average sign of the CT-QMC sampling (upper right panel) and average local spectral function of atom 1. The changes with ξ in the imaginary part of the diagonal elements of the local self-energy (Figure A.3) and the occupancies (Figure A.4) are reflected in the local Matsubara Green's function and the average local spectral function, which show an insulating trend for increasing ξ (This is similar to the standard basis). The sign of the calculation is strongly influenced by ξ. However, it is not as heavily influenced as in the LS basis (Figure A.2 dropping only to 0.8 for $\xi = 2\,\text{eV}$. In difference the sign keeps dropping also for larger ξ.

Appendix B

Local One-Particle Coefficients and Local Interaction Coefficients of Atom 1 of $LiOsO_3$

Here we dislpay the local one-particle coefficient matrix and the local interaction coefficient matrix for atom 1 of $LiOsO_3$. All other five atoms have very similar coefficients. The coefficients are derived from a DFT + cRPA calculation and are used as input for calculations of this thesis. In Table B.1 the local one-particle coefficients are displayed. The offidagonal elements are of the size of 30% of the Hund's J parameter (0.26). In Table B.2 the local interaction coefficients are displayed.

band1	band2	Value [eV]
1	1	5.0447
1	2	0.0765
1	3	0.0789
2	1	0.0765
2	2	5.0423
2	3	0.0777
3	1	0.0789
3	2	0.0777
3	3	5.0471

Table B.1: Local one-particle coefficients $\epsilon_{\gamma\bar{\gamma}}$ of atom 1 from a cRPA calculation. The other atoms are similar. The k-dependend one-particle coefficient matrix (Wannier Hamiltonian) is too large to display.

band1	band2	band3	band4	Value [eV]	band1	band2	band3	band4	Value [eV]
1	1	1	1	2.41278	3	2	2	2	0.02168
2	1	1	1	0.02057	1	2	3	2	-0.00455
3	1	1	1	-0.00123	2	2	3	2	0.02168
1	1	2	1	0.02057	3	2	3	2	1.79130
2	1	2	1	1.79087	1	3	1	2	-0.00467
3	1	2	1	-0.00467	2	3	1	2	-0.00503
1	1	3	1	-0.00123	3	3	1	2	-0.00547
2	1	3	1	-0.00467	1	3	2	2	-0.00503
3	1	3	1	1.79069	2	3	2	2	0.02168
1	2	1	1	0.02057	3	3	2	2	0.26119
2	2	1	1	0.26078	1	3	3	2	-0.00547
3	2	1	1	-0.00514	2	3	3	2	0.26119
1	2	2	1	0.26078	3	3	3	2	-0.00252
2	2	2	1	-0.00123	1	1	1	3	-0.00123
3	2	2	1	-0.00503	2	1	1	3	-0.00514
1	2	3	1	-0.00514	3	1	1	3	0.26058
2	2	3	1	-0.00503	1	1	2	3	-0.00514
3	2	3	1	-0.00499	2	1	2	3	-0.00455
1	3	1	1	-0.00123	3	1	2	3	-0.00547
2	3	1	1	-0.00514	1	1	3	3	0.26058
3	3	1	1	0.26058	2	1	3	3	-0.00547
1	3	2	1	-0.00514	3	1	3	3	0.02044
2	3	2	1	-0.00455	1	2	1	3	-0.00467
3	3	2	1	-0.00547	2	2	1	3	-0.00503
1	3	3	1	0.26058	3	2	1	3	-0.00547
2	3	3	1	-0.00547	1	2	2	3	-0.00503
3	3	3	1	0.02044	2	2	2	3	0.02168
1	1	1	2	0.02057	3	2	2	3	0.26119
2	1	1	2	0.26078	1	2	3	3	-0.00547
3	1	1	2	-0.00514	2	2	3	3	0.26119
1	1	2	2	0.26078	3	2	3	3	-0.00252
2	1	2	2	-0.00123	1	3	1	3	1.79069
3	1	2	2	-0.00503	2	3	1	3	-0.00499
1	1	3	2	-0.00514	3	3	1	3	0.02044
2	1	3	2	-0.00503	1	3	2	3	-0.00499
3	1	3	2	-0.00499	2	3	2	3	1.79130
1	2	1	2	1.79087	3	3	2	3	-0.00252
2	2	1	2	-0.00123	1	3	3	3	0.02044
3	2	1	2	-0.00455	2	3	3	3	-0.00252
1	2	2	2	-0.00123	3	3	3	3	2.41265
2	2	2	2	2.41183					

Table B.2: Interaction coefficients of $U_{\gamma_1\gamma_2\gamma_3\gamma_4}$ of atom 1 from a cRPA calculation. The other atoms are similar.

Appendix C

Example Parameters.in

These parameters.in files give reasonable results if the code is run on 480-800 (30-50 nodes on the Vienna Scientific Cluster 3) cores in parallel.

Example Parameters.in for a calculation without spin-orbit coupling in the standard basis:

```
[General]
DOS = ReadIn
NAt = 6                                  # Number of atoms
HkFile = HK_LiOsO3_.dat                  # Hamiltonian H(k) File
beta = 15                                # 15 20 30 50
totdens = 3.0                            # Electrons per atom
EPSN = 1e-3                              # Search mu-tolerance
readold = 0
fileold = asdf
DMFTsteps = 100
FileNamePrefix = LiOsO3_t2g_Full_Coulomb_beta15
EPSEQ = 1e-3                             # Limit for atomic equivalence
magnetism = para                         # Enforces paramagnetism
mixing = 0.5                             # Mixing of the self-energy
siw_moments = estimate                   # For continuation of the self-energy
#equiv = 0,1,0,1,0,1                     # To enforce equivalence of atoms

[Atoms]
[[1]]
Hamiltonian = ReadNormalUmatrix          # Or Kanamori
QuantumNumbers= Nt All Szt #Qzt          # Conserved quantum numbers
Nd = 3                                   # Number of d-bands
umatrix = U_ijkl_LiOsO3_at1.dat
#Udd = 2.412                             # For Kanamori
#Vdd = 1.791                             # For Kanamori
#Jdd = 0.261                             # For Kanamori

.
.                                        # Here go atoms 2-6
.

[QMC]
Eigenbasis = 1
Nwarmups = 1e5
Nmeas = 6e4                              # 6e4-6e6 Measurments
```

```
NCorr = 2e2                          # 1e2-1e3 (beta dependent)
                                     # Correlation length
Niw = 1000                           # Number of Matsubara frequencies
Ntau = 1000                          # Number of tau points
statesampling = 1
offdiag = 1                          # Only for ReadNormalUmatrix
```

Example Parameters.in for a calculation with spin-orbit coupling in a rotated basis:

```
[General]
DOS = ReadInSO
NAt = 6                              # Number of atoms
HkFile = HK_LiOsO3_SOC_rot.dat       # Hamiltonian H(k) File
beta = 15                            # 15 20 30 50
totdens = 3.0                        # Electrons per atom
EPSN = 1e-3                          # Search mu-tolerance
readold = 0
fileold = asdf
DMFTsteps = 100
FileNamePrefix = LiOsO3_t2g_Full_Coulomb_beta15_lambda0.15
EPSEQ = 1e-3                         # Limit for atomic equivalence
magnetism = ferro                    # Most general
mixing = 0.5                         # Mixing of the self-energy
siw_moments = estimate               # For continuation of the self-energy
#equiv = 0,1,0,1,0,1                 # To enforce equivalence of atoms

[Atoms]
[[1]]
Hamiltonian = ReadUmatrix            # Spin dependent
QuantumNumbers= Nt  All              # Conserved quantum numbers
Nd = 3                               # Number of d-bands
complex_umatrix = 1
umatrix_re = U_ijkl_LiOsO3_at1_rot_re.dat
umatrix_im = U_ijkl_LiOsO3_at1_rot_im.dat

.
.                                    # Here go atoms 2-6
.

[QMC]
Eigenbasis = 1
Nwarmups = 1e5
Nmeas = 6e4                          # 6e4-6e6 Measurments
NCorr = 2e2                          # 1e2-1e3 (beta dependent)
                                     # Correlation length
Niw = 1000                           # Number of Matsubara frequencies
Ntau = 1000                          # Number of tau points
statesampling = 0
offdiag = 1                          # Only for ReadNormalUmatrix
Percentage4OperatorMove = 0.005      # Necessary for correct sampling
complex = 1
TaudiffMax = 2                       # Max. tau diff. of 2 Operator insertion
use_phase = 1
MeasDensityMatrix = 1
```

Appendix D

Read and Write Module

This module contains six functions. "readaline" reads the next non commented line of an opened file, "checkline" returns the input line with possible comments stripped off, "read_hk_wannier" reads a Wannier Hamiltonian formatted as needed by w2dynamics and returns it in a numpy array of the form (kpoint, band, spin, band, spin), "write_hk_wannier" takes a numpy array of the form (kpoint, band, spin, band, spin) and writes it to a file formatted as input for w2dynammics, "read_umatrix" reads an umatrix file formatted as needed by w2dynamics and returns an numpy array of the form (band, spin, band, spin, band, spin, band, spin) where the spin dependency is optional and "write_umatrix" takes a numpy array of the form (band, spin, band, spin, band, spin, band, spin) where again the spin is optional and writes it to a file formatted as input to w2dynamics.

```
import numpy as np
import sys
import custom_errors as err

def readaline(readfile, comments='#'):
    '''This is a function to reading the next line which is not a comment \
       from a file ignoring everthing after the comment symbol'''
    while True:
        line = readfile.readline()
        if line[0] == comments:
            pass
        else:
            break
    commentpos = 0
    for letter in line:
        if letter == comments:
            return line[0:commentpos] + '\n'
        commentpos += 1
    return line

def checkline(line, comments='#'):
    '''This function checks whether there is a comment in line. It returns \
       everthing up to the comment including a \n.'''
    commentpos=0
    for letter in line:
```

```
            if letter == comments:
                return line[0:commentpos] + '\n'
            commentpos += 1
        return line

def read_hk_wannier(filename,spin=False):
    '''Function to read hk from a file with name 'filename'. spin \
       dependency is False by default. If spin is set to True it assumes \
       wannier convention (orbital index running fastest, spin index \
       slowest). It returns the hk of form of an numpy array of form \
       (number of kpoints, number of orbitals, number of spins, number of \
       orbitals, number of spins), the kpoints in form of a numpy array of \
       form (number of kpoints, x, y, z)\nreturn kpoints, hk'''
    f = open(filename, 'r')
    firstline = readaline(f)
    nk = int(firstline.split()[0]) #Number of k points of hk
    nd = int(firstline.split()[1]) #Number of orbitals (inkl. spin) of hk
    hk = np.zeros((nk,nd,nd),dtype=complex)
    kpoints = np.zeros((nk,3))
    for i in range(0,nk):
        splitline = readaline(f).split()
        kpoints[i,0] = float(splitline[0])
        kpoints[i,1] = float(splitline[1])
        kpoints[i,2] = float(splitline[2])
        for j in range(0,nd):
            splitline = readaline(f).split()
            for k in range(0,nd):
                hk[i,j,k] = complex(float(splitline[2*k]), \
                                    float(splitline[2*k+1]))
    if spin:
        hk = hk.reshape(nk, 2, nd/2, 2, nd/2)
        hk = hk.transpose(0,2,1,4,3)
    else:
        hk = hk.reshape(nk, 1, nd, 1, nd)
        hk = hk.transpose(0,2,1,4,3)

    f.close()
    return hk, kpoints

def write_hk_wannier(filename,hk,kpoints):
    '''Function to write hk to a file named 'filename' in wannier format \
       (spin indices running slower than orbital indices). Assumes hk to \
       be of the form (nk,nbands,spins,nbands,spins) and kpoint(nk,3). nd is\
       the number of orbitals (excluding spin), nk the number of kpoints.'''
    f = open(filename, 'w')
    nk = hk.shape[0]
    nbands = hk.shape[1]
    nspin = hk.shape[2]
    hk = hk.transpose(0,2,1,4,3)
    hk = hk.reshape(nk,nspin*nbands,nspin*nbands)

    #first line: number of k-points, number wannier orbitals, number of bands
    f.write(str(nk)+" "+str(nspin*nbands)+" "+str(nspin*nbands)+"\n")

    for k in range(0,nk):
        f.write(str(kpoints[k,0])+"  "+str(kpoints[k,1])+"  "+ \
```

```
                str(kpoints[k,2])+" \n")
        for i in range(0,nspin*nbands):
            for j in range(0,nspin*nbands):
                f.write('%+010.8f' % np.real(hk[k,i,j]))
                f.write("  ")
                f.write('%+10.8f' % np.imag(hk[k,i,j]))
                f.write("  ")
            f.write("\n")

def read_umatrix(filename, spin):
    '''Function to read a umatrix from a .dat file. 2 possible Formats
       1.: 1 1 1 1 value (spin==False)
       2.: 1u 1d 1u 1d value (spin==True)
    '''
    try:
        if type(filename) is not str: raise TypeError("1. argument \
            (filename) must be of type str")
        if type(spin) is not bool: raise TypeError("2. argument \
            (spin) must be of type bool:")
    except TypeError:
        raise
        sys.exit()
    f=open(filename, 'r')
    firstline = readaline(f).split()
    try:
        Nbands = int(firstline[0])
        if firstline[1].lower() != "bands": raise err.InputError( \
            "Expecting first non comment line to be of the form: \
             # BANDS")
    except err.InputError:
        raise
        sys.exit()
    Nspin = int(spin)+1
    if spin:
        umatrix=np.zeros((Nbands,2,Nbands,2,Nbands,2,Nbands,2))
    else:
        umatrix=np.zeros((Nbands,Nbands,Nbands,Nbands))

    spindict = {'u':0,'d':1}
    spininfile = False
    try:
        for line in f:
            splitline = line.split()
            newsplitline = []
            for element in splitline[0:-1]:
                newsplitline.append(list(element))
            splitline = [y for x in newsplitline for y in x] + \
                        [splitline[-1]]
            index = np.zeros((Nspin*4,), dtype=int)
            for i in range(0,(len(splitline)-1)):
                element = splitline[i]
                if element in spindict:
                    index[i] = int(spindict[element])
                    spininfile = True
                else:
                    index[i] = int(element)-1
```

```
            umatrix[tuple(index)] = float(splitline[-1])
        except IndexError:
            raise err.InputError("Specifiefied spin dependency does not \
                                  match ufile spin dependency")
            sys.exit()

        try:
            if spininfile!=spin: raise err.InputError("Specifiefied spin \
                dependency does not match ufile spin dependency")
        except err.InputError:
            raise
            sys.exit()

        return umatrix

    def write_umatrix(filename, umatrix, spin):
        '''Funtion to write the umatrix either with spin dependency or without'''
        try:
            if type(filename) is not str: raise TypeError( \
                "1. argument (filenname) must be of type str.")
            if type(umatrix) is not np.ndarray: raise TypeError( \
                "2. argument (umatrix) must be of type numpy.ndarray.")
            if type(spin) is not bool: raise TypeError( \
                "3. argument (spin) must be of type bool.")
            if len(umatrix.shape)!=4 and len(umatrix.shape)!=8: raise \
                err.ShapeError("Shape of umatrix is invalid")
            if len(umatrix.shape)==4 and spin: raise err.ShapeError("Spin \
                independent umatrix detected although spin was set to True.")
            if len(umatrix.shape)==8 and not spin: raise err.ShapeError("Spin \
                dependent umatrix detected although spin was set to False.")
            if spin and (umatrix.shape[1]!=2 or umatrix.shape[3]!=2 or \
            umatrix.shape[5]!=2 or umatrix.shape[7]!=2):
                raise err.ShapeError("Unexpected shape of spin dependent \
                umatrix. Expected shape: (Nbands,2,Nbands,2,Nbands,2,Nbands,2)")
        except TypeError:
            raise
            sys.exit()
        except err.ShapeError:
            raise
            sys.exit()
        f = open(filename, 'w')
        f.write("# non zero elements of interaction matrix U_ijkl\n")
        f.write("%i BANDS\n"%umatrix.shape[0])
        spindict={0:'u',1:'d'}
        if not spin:
            for index, value in np.ndenumerate(umatrix):
                if value != 0.:
                    f.write("%i %i %i %i  %010.10f\n"%(index[0]+1,index[1]+1, \
                            index[2]+1,index[3]+1, value))
        else:
            for index, value in np.ndenumerate(umatrix):
                if value != 0:
                    f.write("%s %s %s %s  %010.10f\n"%(str(index[0]+1)+ \
                        spindict[index[1]],str(index[2]+1)+spindict[index[3]], \
                        str(index[4]+1)+spindict[index[5]],str(index[6]+1)+ \
                        spindict[index[7]],value))
```

Appendix E

Rotating the One-Particle Coefficient Matrix

This script reads a provided Wannier Hamiltonian formatted as needed for w2dynamics and builds the local one-particle Hamiltonian. Then for every atom it cuts out the respective part of the local one-particle Hamiltonian and diagonalizes it in order to obtain the transformation matrix $\mathbf{V}^i$, where i denotes the atom. For a N atom Hamiltonian the full rotation matrix is then build via

$$\mathbf{V}^{\text{full}} = \begin{pmatrix} \mathbf{V}^1 & 0 & 0 \\ 0 & \ddots & 0 \\ 0 & 0 & \mathbf{V}^N \end{pmatrix} \quad . \tag{E.1}$$

The k dependent Hamiltonian is than rotated k-point by k-point and written to a new file.

```
##########################################################################
#This script Rotates Hk+SOC into the eigenbasis of Hk+SOC. It also prints
##########################################################################
##########################################################################
#out some checks if the rotation is valid. Make sure that thoose checks
##########################################################################
#########
#are ok!#
#########

import h5py as hdf5
import numpy as np
import sys
import argparse
# here we need to add the path to the personal myfunc directory
#(location of some read functions)
auxdir="/home/lv70961/sever2/programs/myfunc/"
sys.path.insert(0,auxdir)
# in order to import the functions available in input.py and
#interatction.py and readwrite and custom errors
import readwrite as rw
import custom_errors as err
```

```
parser = argparse.ArgumentParser(description="This script transforms a k \
                        dependent Hamiltonian to its local eigenbasis")
parser.add_argument('hkfile', help='PATH to the k dependent Hamiltonian', \
                    type=str)
parser.add_argument('Natoms', help='Number of atoms', type=int)
parser.add_argument('Nbands', help='Number of bands per atom', type=int)
parser.add_argument('-s', '--spin', action='store_true', default=False, \
                    help="If this option is set script expects a Hamiltonian \
                        with spin dependency, spin indices varying slowest \
                        (Wannier90 Convention).", dest='spin')
args = parser.parse_args()
filename = args.hkfile
spin = args.spin
Nspins = int(spin)+1
Natoms = args.Natoms
Nbands = args.Nbands

### load Hamiltonian
print "Loading Hamiltonian on hk and kpoints on kpoints."
hkfile = file(filename)
hk, kpoints = rw.read_hk_wannier(filename, spin=spin)

print "hk.shape", hk.shape
print "kpoints.shape", kpoints.shape

### get number of k-points
Nk=kpoints.shape[0]
print "Number of k points: ", Nk

try:
    if hk.shape[1] < Natoms*Nbands: raise err.InputError("Input hkfile \
        does not have spin entries! Please don't use -s.")
    if hk.shape[1] > Natoms*Nbands: raise err.InputError("Input hkfile \
        does have spin entries! Please use -s.")
except err.InputError:
    raise
    sys.exit()

#Building hkmean
print "Building hkmean i.e. averaging over all k points"
hkmean = 1./Nk * np.sum(hk, axis=0)
print "hkmean.shape", hkmean.shape

#reshape hkmean
hkmean = hkmean.reshape(Nspins*Nbands*Natoms,Nspins*Nbands*Natoms)
print "hkmean.shape", hkmean.shape

#Creating array with mean Hamiltonians per atom
print "Building hkmean_pa (hkmean per atom)"
hkmean_pa = np.zeros((Natoms,Nspins*Nbands,Nspins*Nbands),dtype=complex)
for i in range(0,Natoms):
    hkmean_pa[i] = hkmean[i*Nspins*Nbands:(i+1)*Nspins*Nbands, \
                        i*Nspins*Nbands:(i+1)*Nspins*Nbands]

print "hkmean_pa.shape", hkmean_pa.shape
```

```
for a in range(0,Natoms):
    print "hkmean_pa[" + str(a) + "]"
    if spin:
        for i in range(0,Nspins*Nbands):
            print '%+05.5f%+05.5fi' %(np.real(hkmean_pa[a,i,0]), \
                  np.imag(hkmean_pa[a,i,0])), '%+05.5f%+05.5fi' \
                  %(np.real(hkmean_pa[a,i,1]), np.imag(hkmean_pa[a,i,1])), \
                  '%+05.5f%+05.5fi' %(np.real(hkmean_pa[a,i,2]), \
                  np.imag(hkmean_pa[a,i,2])), '%+05.5f%+05.5fi' \
                  %(np.real(hkmean_pa[a,i,3]), np.imag(hkmean_pa[a,i,3])), \
                  '%+05.5f%+05.5fi' %(np.real(hkmean_pa[a,i,4]), \
                  np.imag(hkmean_pa[a,i,4])), '%+05.5f%+05.5fi' \
                  %(np.real(hkmean_pa[a,i,5]), np.imag(hkmean_pa[a,i,5]))
    else:
        for i in range(0,Nspins*Nbands):
            print '%+05.5f%+05.5fi' %(np.real(hkmean_pa[a,i,0]), \
                  np.imag(hkmean_pa[a,i,0])), '%+05.5f%+05.5fi' \
                  %(np.real(hkmean_pa[a,i,1]), np.imag(hkmean_pa[a,i,1])), \
                  '%+05.5f%+05.5fi' %(np.real(hkmean_pa[a,i,2]), \
                  np.imag(hkmean_pa[a,i,2]))

#Solving the Eigenvalue problem
print "Solving the Eigenvalue problem for hkmean_pa"
EigVal = np.zeros((Natoms,Nspins*Nbands),dtype=complex)
EigVec = np.zeros_like(hkmean_pa)
for i in range(0,Natoms):
    EigVal[i], EigVec[i] = np.linalg.eigh(hkmean_pa[i])
    print "Eigvalues of atom " + str(i), EigVal[i]

print "Checking if transformations of each atom are unitary."
eye = np.eye(Nspins*Nbands)
for i in range(0,len(EigVal)):
    print "Checking transformation of atom %i" %(i+1)
    try:
        if not np.allclose(np.dot(EigVec[i].conj().T,EigVec[i]),eye): \
            raise RuntimeError("Transformation of atom %i is not unitary! \
                You may try to change np.linalg.eigh to np.linalg.eig at \
                diagonalisation procedure"%(i+1))
    except RuntimeError:
        raise
        sys.exit()
    else:
        print "Transformation of atom %i all clear."%(i+1)

#Creating the Basis Transformation
print "Building full basis transformation matrix"
Trafo = np.zeros_like(hkmean)
for i in range(0,Natoms):
    Trafo[i*Nspins*Nbands:(i+1)*Nspins*Nbands, \
          i*Nspins*Nbands:(i+1)*Nspins*Nbands] = EigVec[i]
InvTrafo = Trafo.conj().T

print "Checking if full transformation is unitary."
try:
    if not np.allclose(np.dot(InvTrafo,Trafo),np.eye(Nspins*Nbands*Natoms)): \
        raise RuntimeError("Full transformation is not unitary! You may try \
```

```
                                to change np.linalg.eigh to np.linalg.eig at \
                                diagonalisation procedure")
except RuntimeError:
    raise
    sys.exit()
else:
    print "Full transformation all clear."

#Rotating Hamiltonian
print "Transforming the Hamiltonian"
hk = hk.reshape(Nk,Nspins*Nbands*Natoms,Nspins*Nbands*Natoms)
print "hk.shape", hk.shape
for i in range(0,Nk):
    hk[i] = np.dot(InvTrafo,np.dot(hk[i],Trafo))

print "Checking if transformed hk_mean per atom is diagonal with entries \
       equal to the calculated eigenvalues"
oldhkmean = hkmean
hkmean = 1./Nk * np.sum(hk, axis=0)
for i in range(0,Natoms):
    try:
        temphkmean = hkmean[i*Nspins*Nbands:(i+1)*Nspins*Nbands, \
                            i*Nspins*Nbands:(i+1)*Nspins*Nbands]
        if not np.allclose(temphkmean,np.diag(EigVal[i])): raise \
            RuntimeError("Transformed Hamiltonian is locally not diagonal \
                          for atom %i. Numeric errors to big!"%(i+1))
    except RuntimeError:
        raise
        sys.exit()
    else:
        print "Transformed local Hamiltonian of atom %i all clear." \
              %(i+1)

hk = hk.reshape(Nk,Nbands*Natoms,Nspins,Nbands*Natoms,Nspins)
print "hk.shape", hk.shape

#Writting output
newfilename = filename[:-4]+"_rot.dat"
print "Writting Hamiltonian to file "+newfilename
rw.write_hk_wannier(newfilename,hk,kpoints)
```

Appendix F

Rotating the Local Interaction Coefficient Matrix

This script reads a provided Wannier Hamiltonian formatted as needed for w2dynamics and builds the local one-particle Hamiltonian. Then for every atom it cuts out the respective part of the local one-particle Hamiltonian and diagonalizes it in order to obtain the transformation matrix $\mathbf{V}^i$, where i denotes the atom. It reads the provided file with the interaction coefficients formatted as needed by w2dynamics, uses the specified transformation matrix to rotate the interaction coefficients according to (3.8) and writes them to a new file, formatted as needed by w2dynamics.

```
##############################################################################
#This script Rotates U_ijkl into the eigenbasis of Hk+SOC. It also prints
##############################################################################
##############################################################################
#out some checks if the rotation is valid. Make sure that thoose checks
##############################################################################
########
#are ok!#
########

import h5py as hdf5
import numpy as np
import sys
import argparse
# here we need to add the path to the personal myfunc directory
# (location of some read functions)
auxdir="/home/lv70961/sever2/programs/myfunc/"
sys.path.insert(0,auxdir)
import readwrite as rw
import custom_errors as err

parser = argparse.ArgumentParser(description="This script transfomrs \
    U_ijkl of one atom to the local eigenbasis of the provided \
    Hamiltonian .The output ufile is spin dependent by default. A pure \
    band transformation can be activated with the --bandsonly option and \
    does only work with non spin dependent Hamiltonians.")
parser.add_argument('hkfile', help='PATH to the k dependent Hamiltonian', \
                    type=str)
```

```
parser.add_argument('Natoms', help='Number of atoms', type=int)
parser.add_argument('Nbands', help='Number of bands per atom', type=int)
parser.add_argument('ufile', help='PATH to the U_ijkl file', type=str)
parser.add_argument('atom', help='The transformation matrix of this atom \
                    will be used to transform U_ijkl', type=int)
parser.add_argument('-s', '--spin', action='store_true', default=False, \
                    help="If this option is set script expects a \
                    Hamiltonian with spin dependency, spin indices varying \
                    slowest (Wannier90 Convention).", dest='spin')
parser.add_argument('-bo','--bandsonly', action='store_true', default=False, \
                    help="If this option is set script expects a ufile \
                    without spin dependency. It will then only transform \
                    the bands. Only works if option -s is NOT set!.", \
                    dest='bandsonly')
parser.add_argument('--corrector', action='store_true', default=False, \
                    help="If this option is set the umatrix will be \
                    corrected before it is transformed. Entries \
                    corresponding to the same band and spin in the first \
                    4 or last 4 indices are set to zero. Has no influence \
                    if -bo (--bandsonly) is set.", dest='corrector')
args = parser.parse_args()
filename = args.hkfile
ufilename = args.ufile
spin = args.spin
Nspins = int(spin)+1
Natoms = args.Natoms
Nbands = args.Nbands
atom = args.atom
bandsonly = args.bandsonly #This bool is used throughout the script
                           #describing wether U_ijkl has spins or not!
                           #Usage may be counterintuitive. Name is
                           #choosen such that users only use it if they
                           #really want to!
Ntspins = 2-int(bandsonly)
corrector = args.corrector

try:
    if atom > Natoms: raise RuntimeError("Number supplied for atom must be \
                                          smaller than number supplied for \
                                          Natoms")
    if spin and bandsonly: raise RuntimeError("--bandsonly (-bo) only works \
                                               without --spin (-s)!")
except RuntimeError:
    raise
    sys.exit()

### load Hamiltonian
print "Loading Hamiltonian on hk and kpoints on kpoints."
hk, kpoints = rw.read_hk_wannier(filename,spin=spin)

print "hk.shape", hk.shape
print "kpoints.shape", kpoints.shape

### get number of k-points
Nk=kpoints.shape[0]
print "Number of k points: ", Nk
```

```
try:
    if hk.shape[1] < Natoms*Nbands: raise err.InputError("Input hkfile \
        does not have spin entries! Please use -s False.")
    if hk.shape[1] > Natoms*Nbands: raise err.InputError("Input hkfile \
        does have spin entries! Please use -s True.")
except err.InputError:
    raise
    sys.exit()

#load umatrix and checking if ufile is spin dependent
ufile=open(ufilename,'r')
rw.readaline(ufile)
line = rw.readaline(ufile)

try:
    if (('u' in line) or ('d' in line)) and bandsonly:
        raise err.InputError("Detected spin dependency in input ufile.\
                    Cannot perform bandsonly transformation!")
    elif ('u' in line) or ('d' in line):
        uspin = True
    else:
        uspin = False
except err.InputError:
    raise
    sys.exit()

ufile.close()

umatrix = rw.read_umatrix(ufilename,spin=uspin)
print "umatrix.shape", umatrix.shape

#blow up umatrix if it is not already spin dependent
if (not uspin) and (not bandsonly):
    print "Blowing up U matrix"
    newumatrix = np.zeros((umatrix.shape[0],) + (2,) + (umatrix.shape[1],)  \
                          + (2,) + (umatrix.shape[2],) + (2,)  \
                          + (umatrix.shape[3],) + (2,),dtype=complex)
    newumatrix[:,0,:,0,:,0,:,0] = umatrix[:,:,:,:]
    newumatrix[:,1,:,0,:,1,:,0] = umatrix[:,:,:,:]
    newumatrix[:,0,:,1,:,0,:,1] = umatrix[:,:,:,:]
    newumatrix[:,1,:,1,:,1,:,1] = umatrix[:,:,:,:]
    umatrix = newumatrix
    if corrector:
        for index, x in np.ndenumerate(umatrix):
            if (index[0:2] == index[2:4]) or (index[4:6] == index[6:8]):
                umatrix[index] = 0.
    print "umatrix.shape", umatrix.shape

#Building hkmean
print "Building hkmean i.e. averaging over all k points"
hkmean = 1./Nk * np.sum(hk, axis=0)
print "hkmean.shape", hkmean.shape

#reshape hkmean
hkmean = hkmean.reshape(Nspins*Nbands*Natoms,Nspins*Nbands*Natoms)
print "hkmean.shape", hkmean.shape
```

```
#Creating array with mean Hamiltonians per atom
print "Building hkmean_pa (hkmean per atom)"
hkmean_pa = np.zeros((Natoms,Nspins*Nbands,Nspins*Nbands),dtype=complex)
for i in range(0,Natoms):
    hkmean_pa[i] = hkmean[i*Nspins*Nbands:(i+1)*Nspins*Nbands, \
                          i*Nspins*Nbands:(i+1)*Nspins*Nbands]

print "hkmean_pa.shape", hkmean_pa.shape

#Solving the Eigenvalue problem
print "Solving the Eigenvalue problem of hkmean_pa for atom %i"%atom
EigVal, EigVec = np.linalg.eigh(hkmean_pa[atom-1])
print "Eigvalues of atom " + str(atom), EigVal

#Creating the Basis Transformation
print "Building basis transformation matrix of atom %i"%atom
Trafo = EigVec
if (not spin) and (not bandsonly):
    print "Expanding transformation to both spin channels."
    temptrafo = np.zeros((Nbands,2,Nbands,2),dtype=complex)
    temptrafo[:,0,:,0] = Trafo
    temptrafo[:,1,:,1] = Trafo
    Trafo = temptrafo.reshape(2*Nbands,2*Nbands)
InvTrafo = Trafo.conjugate().transpose()
print "Trafo.shape", Trafo.shape

print "Checking if transformation is unitary."
try:
    if not np.allclose(np.dot(InvTrafo,Trafo),np.eye(Ntspins*Nbands)):
        raise RuntimeError("Transformation is not unitary! You may try \
                            to change np.linalg.eigh to np.linalg.eig at \
                            diagonalisation procedure")
except RuntimeError:
    raise
    sys.exit()
else:
    print "Transformation all clear."
#transforming umatrix
print "Transforming umatrix with transformation matrix of atom %i"%atom
umatrix = umatrix.reshape(Ntspins*Nbands,Ntspins*Nbands, \
                          Ntspins*Nbands,Ntspins*Nbands)
umatrix = np.einsum('ai,bj,ijkl,kc,ld',InvTrafo,InvTrafo,umatrix,Trafo, \
                    Trafo,dtype=complex)
print "umatrix.shape", umatrix.shape

if not bandsonly:
    umatrix = umatrix.reshape(Nbands,2,Nbands,2,Nbands,2,Nbands,2)

#Writting output
newfilename1 = ufilename[:-4] + "_rot_re.dat"
newfilename2 = ufilename[:-4] + "_rot_im.dat"
print "Writting Re(U_ijkl) to file " + newfilename1
rw.write_umatrix(newfilename1, umatrix.real, spin=(not bandsonly))
print "Writting Im(U_ijkl) to file " + newfilename2
rw.write_umatrix(newfilename2, umatrix.imag, spin=(not bandsonly))
```

Appendix G

Rotating One-Particle Objects

This script reads a provided Wannier Hamiltonian formatted as needed for w2dynamics and builds the local one-particle Hamiltonian. Then for every atom it cuts out the respective part of the local one-particle Hamiltonian and diagonalizes it in order to obtain the transformation matrix $\mathbf{V}^i$, where i denotes the atom. It reads the provided hdf5 file with the one particle objects (ftau, gtau, giw, siw) generated by w2dynamics, uses the specified transformation matrix to rotate the specified objects to the choosen basis (by default only gtau is rotated and the new basis is the LS basis) and writes them to files named "object_(band,spin,band,spin).dat" in a subfolder (named LS_basis or Hloc_basis, according to the choosen basis). If the subfolder is not present it is created.

```
##########################################################################
# This script rotates an object into or from the basis in which Hloc
##########################################################################
################
# is diagonal #
################

import numpy as np
import matplotlib.pyplot as plt
import sys
import os
import argparse
import h5py as hdf5
# here we need to add the path to the personal myfunc directory
# (location of some read functions)
auxdir="/home/lv70961/sever2/programs/myfunc/"
sys.path.insert(0,auxdir)
import readwrite as rw
import custom_errors as err

class shift(argparse.Action):
    def __call__(self, parser, namespace, values, option_sting=None):
        newvalues = []
        for value in values:
            newvalues.append(value-1)
        setattr(namespace, self.dest, newvalues)
```

```
parser = argparse.ArgumentParser(description="This script rotates objects \
    depending on tau either in the basis where Hloc is diagonal or from the \
    basis where Hloc is diagonal into the LS Basis. On default it rotates \
    gtau.")
parser.add_argument('hkfile', help='PATH to the k dependent Hamiltonian. \
    Needs to be spin dependend', type=str)
parser.add_argument('Natoms', help='Number of atoms', type=int)
parser.add_argument('Nbands', help='Number of bands per atom', type=int)
parser.add_argument('hdf5file', help='PATH to the HDF5 file with the \
    w2dynamics results', type=str)
parser.add_argument('--toDIAG', default=False, action='store_true', \
    help="Rotate from the LS to the diagonal basis. On default it the \
    scripts rotates from the diagonal to the LS basis.")
parser.add_argument('-A', '--Atoms', default=[0], type=int, dest='Atoms', \
    nargs='*', action=shift, help="Objects of this atoms will be rotated.")
parser.add_argument('--notgtau', default=True, action='store_false', \
    help="Specify in order not to rotated gtau. In default the script \
    rotates gtau.")
parser.add_argument('--ftau', default=False, action='store_true', \
    help="Specify in order to rotated ftau.")
parser.add_argument('--giw', default=False, action='store_true', \
    help="Specify in order to rotated giw.")
parser.add_argument('--siw', default=False, action='store_true', \
    help="Specify in order to rotated siw.")
parser.add_argument('-s', '--spin', default=False, action='store_true', \
    help="Specify that Hamiltonian has spin dependency.")
parser.add_argument('-i', '--iteration', default=None, type=int, \
    help="Specify which iteration of hdf5 file to use.")
args = parser.parse_args()
hkfile = args.hkfile
Natoms = args.Natoms
Nbands = args.Nbands
hdf5file = args.hdf5file
atoms = args.Atoms
toDIAG = args.toDIAG
rotate_gtau = args.notgtau
rotate_ftau = args.ftau
rotate_giw = args.giw
rotate_siw = args.siw
iteration = args.iteration
Nspins = int(args.spin) + 1

for atom in atoms:
    if atom < 0 or atom > Natoms-1:
        raise err.InputError("Atom list out of range!")
        sys.exit()
if rotate_gtau == False:
    rot_objs = []
else:
    rot_objs = ["gtau"]
if rotate_ftau == True:
    rot_objs.append("ftau")
if rotate_giw == True:
    rot_objs.append("giw")
if rotate_siw == True:
    rot_objs.append("siw")
```

```
if Nspins == 2:
    print "Loading spin dependent Hamiltonian on hk and kpoints on kpoints."
    hk, kpoints = rw.read_hk_wannier(hkfile, spin=True)
else:
    print "Loading spin independent Hamiltonian on hk and kpoints on kpoints."
    hk, kpoints = rw.read_hk_wannier(hkfile, spin=False)
Nk=kpoints.shape[0]
print "hk.shape", hk.shape
print "kpoints.shape", kpoints.shape

print "Building hkmean i.e. averaging over all k points"
hkmean = 1./Nk * np.sum(hk, axis=0)
print "hkmean.shape", hkmean.shape
hkmean = hkmean.reshape(Nspins*Nbands*Natoms, Nspins*Nbands*Natoms)
print "hkmean.shape", hkmean.shape
print "Building hkmean_pa (hkmean per atom)"
hkmean_pa = np.zeros((Natoms, Nspins*Nbands, Nspins*Nbands), dtype=complex)
for i in range(0,Natoms):
    hkmean_pa[i] = hkmean[i*Nspins*Nbands:(i+1)*Nspins*Nbands, i*Nspins  \
    *Nbands:(i+1)*Nspins*Nbands]

print "hkmean_pa.shape", hkmean_pa.shape

if Nspins == 2:
    for atom in atoms:
        print "hkmean_pa[" + str(atom) + "]"
        for i in range(0,Nspins*Nbands):
            print '%+05.5f%+05.5fi' %(np.real(hkmean_pa[atom,i,0]),  \
                                      np.imag(hkmean_pa[atom,i,0])),  \
                  '%+05.5f%+05.5fi' %(np.real(hkmean_pa[atom,i,1]),  \
                                      np.imag(hkmean_pa[atom,i,1])),  \
                  '%+05.5f%+05.5fi' %(np.real(hkmean_pa[atom,i,2]),  \
                                      np.imag(hkmean_pa[atom,i,2])),  \
                  '%+05.5f%+05.5fi' %(np.real(hkmean_pa[atom,i,3]),  \
                                      np.imag(hkmean_pa[atom,i,3])),  \
                  '%+05.5f%+05.5fi' %(np.real(hkmean_pa[atom,i,4]),  \
                                      np.imag(hkmean_pa[atom,i,4])),  \
                  '%+05.5f%+05.5fi' %(np.real(hkmean_pa[atom,i,5]),  \
                                      np.imag(hkmean_pa[atom,i,5]))
else:
    for atom in atoms:
        print "hkmean_pa[" + str(atom) + "]"
        for i in range(0,Nspins*Nbands):
            print '%+05.5f%+05.5fi' %(np.real(hkmean_pa[atom,i,0]),  \
                                      np.imag(hkmean_pa[atom,i,0])),  \
                  '%+05.5f%+05.5fi' %(np.real(hkmean_pa[atom,i,1]),  \
                                      np.imag(hkmean_pa[atom,i,1])),  \
                  '%+05.5f%+05.5fi' %(np.real(hkmean_pa[atom,i,2]),  \
                                      np.imag(hkmean_pa[atom,i,2])),  \

print "Solving the Eigenvalue problem for hkmean_pa"
EigVal = np.zeros((Natoms, Nspins*Nbands),dtype=complex)
EigVec = np.zeros_like(hkmean_pa)
for i in range(0,Natoms):
    EigVal[i], EigVec[i] = np.linalg.eigh(hkmean_pa[i])
```

```
        print "Eigenvalues atom ", i+1
        print EigVal[i]

    #test for non spin rotation
    if Nspins == 1:
        print "Blowing up Transformation matrix to two spins"
        temp = EigVec.copy()
        EigVec = np.zeros((Natoms,Nbands,2,Nbands,2), dtype=complex)
        EigVec[:,:,0,:,0] = temp[:]
        EigVec[:,:,1,:,1] = temp[:]
        print "EigVec.shape ", EigVec.shape
        EigVec = EigVec.reshape(Natoms,2*Nbands,2*Nbands)
        print "EigVec.shape ", EigVec.shape

    print "Loading hdf5 file: " + hdf5file
    f=hdf5.File(hdf5file,"r")
    if iteration == None:
        print 'Using last iteration'
        iteration = "%03i" %int(f["/.config"].attrs.get("general.dmftsteps")) \
                    #using the last Iteration
    else:
        print 'Using %03i iteration' %iteration
        iteration = "%03i" %iteration

    #Checking for directory to put results
    if toDIAG:
        basis = 'hloc'
    else:
        basis = 'LS'
    basedir = "./" + basis + "_basis"
    if not os.path.exists(basedir):
        os.makedirs(basedir)

    for obj in rot_objs:
        for atom in atoms:
            atomstr = "%03i" %(atom+1)
            print ""
            print "Loading object " + obj + " of atom " + atomstr
            values = f["dmft-" + iteration + "/ineq-" + atomstr + "/" + obj \
                       + "-full/value"][:]
            values = np.array(values,dtype=complex)
            if obj in ['gtau']:
                axis = f[".axes/taubin"][:]
                ax = "tau"
            elif obj in ['ftau']:
                axis = f[".axes/tauf"][:]
                ax = "tau"
            else:
                axis = f[".axes/iw"][:]
                ax = "iw"
            n = values.shape[-1]
            print values.shape, n
            print axis.shape
            print "Building basis transformation matrices"
            if toDIAG:
                Trafo = np.array(EigVec[atom])
```

```
            InvTrafo = np.conjugate(np.transpose(Trafo))
        else:
            InvTrafo = np.array(EigVec[atom])
            Trafo = np.conjugate(np.transpose(InvTrafo))
        print "Checking if transformation is unitary."
        try:
            if not np.allclose(np.dot(InvTrafo,Trafo),np.eye(2*Nbands)): \
                raise RuntimeError("Full transformation is not unitary! \
                                    You may try to change np.linalg.eigh \
                                    to np.linalg.eig at diagonalisation \
                                    procedure")
        except RuntimeError:
            raise
            sys.exit()
        else:
            print "Transformation all clear."

        print "Rotating"
        values = values.reshape(2*Nbands,2*Nbands,n)
        print obj + ".shape", values.shape
        for i in range(0,n):
            values[:,:,i] = np.dot(InvTrafo,np.dot(values[:,:,i],Trafo))
        values = values.reshape(Nbands,2,Nbands,2,n)
        print obj + ".shape", values.shape

        print "Saving " + obj
        targetdir = basedir + "/atom-" + atomstr
        if not os.path.exists(targetdir):
            os.makedirs(targetdir)
        for b1 in range(0,Nbands):
            for s1 in range (0,2):
                for b2 in range(0,Nbands):
                    for s2 in range (0,2):
                        filename= targetdir + "/"  + obj + "_" + basis + \
                                  "_" + str(b1+1) + str(s1+1) + str(b2+1) \
                                  + str(s2+1) +".dat"
                        targetf = open(filename, 'w')
                        targetf.write('#%14s' % ax)
                        targetf.write('%15s' % ("Re("+obj+")"))
                        targetf.write('%15s' % ("Im("+obj+")"))
                        targetf.write('\n')
                        data=np.column_stack((axis,np.real( \
                                              values[b1,s1,b2,s2,:]) \
                                                   ,np.imag( \
                                              values[b1,s1,b2,s2,:])))
                        np.savetxt(targetf,data,fmt='%15.10f')
                        targetf.close()

f.close()
```

Appendix H

Adding Spin-Orbit Coupling to the One-Particle Coefficient Matrix

This script reads a provided Wannier Hamiltonian formatted as needed for w2dynamics. Then it quadruples its size by introducing a spin dependency, i.e. every entry gets reshaped according to

$$a \to \begin{pmatrix} a & 0 \\ 0 & a \end{pmatrix} \quad , \tag{H.1}$$

and adds the spin-orbit coupling to the k-dependent Hamiltonian at every k-point according to (1.3) where the specified parameter $\lambda = \frac{\xi}{2}$. For multiple atoms in the first brillouin zone the full local (atomic) spin-orbit Hamiltonian reads

$$\hat{H}_{\mathrm{SOC}}^{\mathrm{full}} = \begin{pmatrix} \hat{H}_{\mathrm{SOC}} & 0 & 0 \\ 0 & \ddots & 0 \\ 0 & 0 & \hat{H}_{\mathrm{SOC}} \end{pmatrix} \quad , \tag{H.2}$$

where $\hat{H}_{\mathrm{SOC}}$ is given by (1.3) and the diagonal contains as many copies of it as there are atoms in the first brillouin zone. Eventually the new k-dependent Hamiltonian is written to a new file formatted as needed by w2dynamics.

```
############################################################
#This script adds the local SOC to a provided HK file#
############################################################

import h5py as hdf5
import numpy as np
import sys
# here we need to add the path to the personal myfunc directory
# (location of some read functions)
auxdir="/home/lv70961/sever2/programs/myfunc/"
sys.path.insert(0,auxdir)
import readwrite as rw
import argparse
```

```
parser = argparse.ArgumentParser(description="This script adds SOC to an \
    existing t2g Hamiltonian. This will quadruple its size.")

parser.add_argument('hkfile', help='PATH to an existing file containing \
                    the Hamiltonian', type=str)
parser.add_argument('Natoms', help='Number of atoms of the \
                    Hamiltonian / brillouin zone', type=int)
parser.add_argument('epsilon', help='Epsilon Parameter of SOC', type=float)

args = parser.parse_args()
hkfile = args.hkfile
epsilon = args.epsilon
Na = args.Natoms

#setting the epsilon parameter for the SOC
print "epsilonSOC = ", epsilon

### load Hamiltonian
print "Loading Hamiltonian from file: ", hkfile
hk, kpoints = rw.read_hk_wannier(hkfile,spin=False)

print "hk.shape", hk.shape
print "kpoints.shape", kpoints.shape

### get number of k-points
Nk=kpoints.shape[0]
print "Nk", Nk

### number of d-orbitals
Nd=hk.shape[1]
print "Nd", Nd

#Setting atoms and orbitals per atom
Ndpa = Nd/Na        #Number of d-orbitals per atom
Ns = 2              #Number of spins
print "Na", Na
print "Ndpa", Ndpa
print "Ns", Ns

#Blowing the Hamiltonian to up for spin inclusion
hk = hk.transpose(0,1,3,2,4)
print "hk.shape", hk.shape
print "Blowing up Hamiltonian"
hk = np.append(np.append(hk,np.zeros_like(hk),axis=4), \
               np.append(hk,np.zeros_like(hk),axis=4)[:,:,:,:,::-1],axis=3)
print "hk.shape", hk.shape

#build hSOC from pauli matricies
print "Building hSOC"
hSOC = np.zeros_like(hk[1])
sigma1 = np.array([[0,1],[1,0]])
sigma2 = np.array([[0,-1j],[1j,0]])
sigma3 = np.array([[1,0],[0,-1]])
```

```
for i in range(0,Na):
        hSOC[0+3*i,1+3*i] = -1j*sigma3
        hSOC[0+3*i,2+3*i] = 1j*sigma1
        hSOC[1+3*i,0+3*i] = 1j*sigma3
        hSOC[1+3*i,2+3*i] = -1j*sigma2
        hSOC[2+3*i,0+3*i] = -1j*sigma1
        hSOC[2+3*i,1+3*i] = 1j*sigma2
hSOC = epsilon * hSOC
print "hSOC.shape", hSOC.shape

#build hkSOC
print "Building hkSOC"
hkSOC = np.zeros_like(hk)
for i in range(0,hkSOC.shape[0]):
    hkSOC[i] = hSOC
print "hkSOC.shape", hkSOC.shape

#Adding together hk and hkSOC
print "Adding hkSOC to hk"
hk += hkSOC

#Building hkmean as check
hkmean = 1./Nk*np.sum(hk, axis=0)
hkmean = hkmean.transpose(0,2,1,3)
hkmean = hkmean.reshape(Ns*Nd,Ns*Nd)

#writting hkmean of the first atom
print "hkmean including SOC for the first atom"
for i in range(0,6):
    print '%+3.3f%+3.3fi' % (np.real(hkmean[i,0]), np.imag(hkmean[i,0])), \
          '%+3.3f%+3.3fi' % (np.real(hkmean[i,1]), np.imag(hkmean[i,1])), \
          '%+3.3f%+3.3fi' % (np.real(hkmean[i,2]), np.imag(hkmean[i,2])), \
          '%+3.3f%+3.3fi' % (np.real(hkmean[i,3]), np.imag(hkmean[i,3])), \
          '%+3.3f%+3.3fi' % (np.real(hkmean[i,4]), np.imag(hkmean[i,4])), \
          '%+3.3f%+3.3fi' % (np.real(hkmean[i,5]), np.imag(hkmean[i,5]))

#Shaping it such that it can be written in wanner90 format
print "Shaping Hamiltonian for passing to write function"
print "hk.shape", hk.shape
hk = hk.transpose(0,1,3,2,4)
print "hk.shape", hk.shape

#Writting output
hkfilenew = hkfile[:-4] + "_SOC.dat"
print "Writting Hamiltonian to file: " + hkfilenew
rw.write_hk_wannier(hkfilenew,hk,kpoints)
```

Bibliography

[1] Calder, S. *et al.* Magnetically Driven Metal-Insulator Transition in NaOsO3. *Physical Review Letters* **108**, 257209 (2012).

[2] Lo Vecchio, I. *et al.* Infrared evidence of a Slater metal-insulator transition in NaOsO3. *Scientific Reports* **3**, 2990 (2013).

[3] Lo Vecchio, I. *et al.* Electronic correlations in the ferroelectric metallic state of LiOsO3. *Physical Review B* **93**, 161113(R) (2016).

[4] Kim, B. *et al.* Lifshitz transition driven by spin fluctuations and spin-orbit renormalization in NaOsO3. *Physical Review B* **94**, 241113(R) (2016).

[5] Giovannetti, G. & Capone, M. Dual nature of the ferroelectric and metallic state in LiOsO3. *Physical Review B* **90**, 195113 (2014).

[6] Held, K. Electronic structure calculations using dynamical mean field theory. *Advances in Physics* **56**, 829–926 (2007).

[7] Kotliar, G. *et al.* Electronic structure calculations with dynamical mean-field theory. *Reviews of Modern Physics* **78**, 865–951 (2006).

[8] Mostofi, A. A. *et al.* An updated version of wannier90: A tool for obtaining maximally-localised Wannier functions. *Computer Physics Communications* **185**, 2309–2310 (2014).

[9] Aryasetiawan, F. *et al.* Frequency-dependent local interactions and low-energy effective models from electronic structure calculations. *Physical Review B* **70**, 195104 (2004).

[10] Pavarini, E., Koch, E., Vollhardt, D. & Lichtenstein, A. I. *The LDA+DMFT approach to strongly correlated materials Modeling and Simulation Vol. 1* (Jülich, 2011).

[11] Kresse, G. & Furthmiiller, J. Efficiency of ab-initio total energy calculations for metals and semiconductors using a plane-wave basis set. *Computational Materials Science* **6**, 15–50 (1996).

[12] Kresse, G. & Furthmu, J. Efficient iterative schemes for ab initio total-energy calculations using a plane-wave basis set . *Physical Review B* **54**, 11169–11186 (1996).

[13] Kresse, G. & Hafner, J. Ab initio molecular dynamics for liquid metals. *Physical Review B* **47**, 558–561 (1993).

[14] Kresse, G. & Hafner, J. Ab initio molecular-dynamics simulation of the liquid-metal-amorphous-semiconductor transition in germanium. *Physical Review B* **49**, 14251–14269 (1994).

[15] Ascroft, N. W. & Mermin, N. D. *Solid State Physics* (Brooks/Cole, Cengage Learning, 1976).

[16] Kowalski, A., Hausoel, A., Gunacker, P. & Sangiovanni, G. State- and superstate-sampling in hybridization-expansion continuous-time quantum Monte Carlo (2018). `arXiv:1807.00361`.

[17] Wallerberger, M. *et al.* w2dynamics: Local one- and two-particle quantities from dynamical mean field theory. *Computer Physics Communications* **235**, 388–399 (2019).

[18] Levy, R., LeBlanc, J. P. F. & Gull, E. Implementation of the Maximum Entropy Method for Analytic Continuation. *Computer Physics Communications* **215**, 149–155 (2017).

[19] Baldassarre, L. *et al.* Quasiparticle evolution and pseudogap formation in V2O3: An infrared spectroscopy study. *Physical Review B* **77**, 113107 (2008).

[20] Mo, S. *et al.* Prominent Quasiparticle Peak in the Photoemission Spectrum of the Metallic Phase of V2O3. *Physical Review Letters* **90**, 186403 (2003).

[21] Martins, C., Aichhorn, M. & Biermann, S. Coulomb correlations in 4d and 5d oxides from first principles - Or how spin-orbit materials choose their effective orbital degeneracies. *Journal of Physics: Condensed Matter* **29**, 263001 (2017).

[22] Zhong, Z., Tóth, A. & Held, K. Theory of spin-orbit coupling at LaAlO3/SrTiO3 interfaces and SrTiO3 surfaces. *Physical Review B* **87**, 161102(R) (2013).

[23] Abrikisov, A., Gorkov, L. & Dzyaloshinski, I. *Methods of Quantum Field Theory in Statistical Physics* (Dover Publications, 1963).

[24] Bruus, H. & Flensber, K. *Many-Body Quantum Theory in Condensed Matter Physics* (Oxford University Press, 2004).

[25] Gerald D. Mahan. *Many particle physics* (Plenum Press, 1990).

[26] Nolting, W. *Grundkurs Theoretische Physik 7* (Springer Spektrum, 2016).

[27] Rammer, J. *Quantum field theory of non-equilibrium states* (Cambridge University Press, 2007).

[28] Rohringer, G. *New routes towards a theoretical treatment of nonlocal electronic correlations.* Dissertation, TU Wien (2013).

[29] Stefanucci, G. & van Leeuwen, R. *Nonequilibrium Many-Body Theory of Quantum Systems* (Cambridge University Press, 2013).

[30] Zagoskin, A. *Quantum Theory of Many-Body Systems* (Springer International, 2014), 2 edn.

[31] Georges, A. & Kotliar, G. Hubbard model in infinite dimensions. *Physical Review B* **45**, 6479–6483 (1992).

[32] Georges, A., Kotliar, G., Krauth, W. & Rozenberg, M. J. Dynamical mean-field theory of strongly correlated fermion systems and the limit of infinite dimensions. *Reviews of Modern Physics* **68**, 13–125 (1996).

[33] Kotliar, G. & Vollhardt, D. Strongly Correlated Materials: Insights From Dynamical Mean-Field Theory. *Physics Today* **57**, 53–59 (2004).

[34] Metzner, W. & Vollhardt, D. Ground-state energy of the d=1,2,3 dimensional Hubbard model in the weak-coupling limit. *Physical Review B* **39**, 4462–4466 (1989).

[35] Schollwöck, U. The density-matrix renormalization group. *Reviews of Modern Physics* **77**, 259–315 (2005).

[36] Schollwöck, U. The density-matrix renormalization group in the age of matrix product states. *Annals of Physics* **326**, 96–192 (2011).

[37] Gull, E. *et al.* Continuous-time Monte Carlo methods for quantum impurity models. *Reviews of Modern Physics* **83**, 349–404 (2011).

[38] Karolak, M. *et al.* Double Counting in LDA+DMFT The Example of NiO. *Journal of Electron Spectroscopy and Related Phenomena* **181**, 11–15 (2010).

[39] Shinaoka, H., Nomura, Y., Biermann, S., Troyer, M. & Werner, P. Negative sign problem in continuous-time quantum Monte Carlo : Optimal choice of single-particle basis for impurity problems. *Physical Review B* **92**, 195126 (2015).

[40] Fuchs, S., Pruschke, T. & Jarrell, M. Analytic continuation of quantum Monte Carlo data by stochastic analytical inference. *Physical Review E* **81**, 056701 (2010).

[41] Petocchi, F. *Competing Interactions in Correlated Heterostructures.* Doctoral thesis, International School for Advanced Studies.